# UNIVERSITY OF OSLO

**Master's thesis**

# Electrostatic control of two-electron quantum dot qubits in a Morse double-well potential

Engineering degeneracy and entanglement for high-fidelity quantum gate protocols

**Jonny Aarstad Igeh**

Computational Science: Physics
60 ECTS study points

Department of Physics
Faculty of Mathematics and Natural Sciences

Spring 2025

**Jonny Aarstad Igeh**

# Electrostatic control of two-electron quantum dot qubits in a Morse double-well potential

## Engineering degeneracy and entanglement for high-fidelity quantum gate protocols

Supervisors:
Morten Hjorth-Jensen
Oskar Leinonen

**Abstract**

Phase instability, control-signal complexity, and fabrication remain key obstacles to implementing high-fidelity, scalable quantum-dot qubits. In this work, we explore the Morse double-well potential as a model for two-electron quantum-dot qubit and develop a numerical framework to solve its time-dependent Schrödinger equation. The method is validated by $> 99.99\%$ agreement between the Sinc-Discrete Variable Representation (Sinc-DVR) basis used and the exact eigenstates of the Morse potential. We employ a product state approach to the two-electron system, allowing us to treat the two electrons as independent particles confined in a double-well potential, with vanishing exchange interaction at our chosen inter-well separation of $d = 15$ a.u. Using our framework, we identify optimal double-well parameters for two distinct operating configurations: a measurement mode with well-separated single-particle levels (zero entanglement) and a gate mode with nearly degenerate first excited single-particle states (maximal entanglement), ensuring that the coupling term in the system Hamiltonian is significant (or non-negligible). Time-domain simulations of the two-electron system, driving the system adiabatically between configurations, demonstrate high-fidelity two-particle entanglement via purely electrostatic control of the potential: detailed benchmarks show a SWAP operation attaining average fidelity of 98.79% and classical fidelity of 99.98% after single-qubit phase corrections are applied. These results establish the Morse double-well as a viable quantum-dot qubit platform, and lay the groundwork for future extensions incorporating spin degrees of freedom and realistic noise models.

## Acknowledgements

# Contents

# Chapter 1

# Introduction

## 1.1 Background and motivation

Quantum computers promise to revolutionize modern computations by leveraging quantum mechanical phenomena such as superposition and entanglement to solve problems that are intractable for classical computers. By harnessing these phenomena, it has been demonstrated that quantum computers can outperform their classical counterparts in specific tasks, such as factoring large numbers, simulating quantum systems and cryptography [1–4]. The rapid development of quantum algorithms and error-correction techniques has fueled optimism that we are nearing the threshold for practical 'quantum advantage'—where quantum computers outperform classical systems in real-world applications—but significant challenges remain in the construction of scalable, noise-resilient quantum hardware [5, 6].

Quantum-dot platforms have emerged as a leading candidate for scalable quantum computing due to their compatibility with semiconductor fabrication and the potential for on-chip qubit integration [7, 8]. These semiconductor materials offer electronic and optical properties that can be precisely engineered via their composition and crystal-lattice structure, to realize any desired quantum-dot architecture. This has allowed for the development of technologies from mobile phones to satellites, and they now seem poised to reshape modern quantum computing hardware [9, 10]. Due to the nanometer scale of semiconductor quantum dots, the electronic motion leads to atom-like electronic structures, where the discrete energy levels can be tuned by varying the quantum dot size, shape, and surrounding environment [11]. Quantum dot spin-qubits have previously demonstrated long coherence times, but their manipulation via electric fields is too slow for many future applications [12], and they are susceptible to noise from spin-orbit and hyperfine interactions [13, 14]. To overcome these limitations, researchers are looking into alternative approaches that utilize electrostatic control [15, 16], and some are looking at alternative quantum dot qubits based on electric charge states [17, 18]. Much progress has been made in the development of quantum-dot qubits, and the field is rapidly evolving, with new techniques showing high fidelity gate operations and long coherence times [9].

Yet, implementing high-fidelity gate operations in such systems often demands complex control hardware—microwave drives, rapid voltage pulses, and magnetic field gradients—making them susceptible to charge noise, phase instabilities, and crosstalk [13, 19, 20]. Purely electrostatic approaches, which manipulate qubit states by shaping static or slowly varying potential landscapes, promise simpler, lower-noise architectures [15, 21]. The Morse double-well potential, with its tunable anharmonic profile and direct analogy to molecular bonding, offers a natural testbed for these electrostatic quantum control strategies—due to the already atom-like electronic structures commonly found in quantum dot systems. Originally developed to model molecular interactions [22], and widely used in quantum chemistry to model diatomic molecules [23], we believe the Morse potential to be a promising candidate for quantum-dot

qubit architecture. Some studies have explored the Morse potential in the context of quantum computing of molecules [24], but it is generally underexplored for quantum-dot qubits and its potential role in quantum hardware. Here we present the Morse double-well potential as a candidate quantum-dot qubit architecture, and show that it can be engineered to create a tuneable two-qubit system, where the anharmonicity of the potential allows for efficient population transfer and entanglement generation between two qubits. Moreover, because the anharmonic energy spacings can be independently tuned (so no two transitions are degenerate), this design also supports stable single-qubit operations.

In this thesis, we develop and analyze a one-dimensional model of two interacting electrons in a Morse double-well potential—a form that can be realized either by static split-gate voltages in a semiconductor heterostructure or by equivalent electrostatic barrier shapes in an experimental electronics setup [21, 25]. By tuning those voltages to set the well's separation, depth, and width, we engineer a potential landscape that supports two well-localized states and switch between an idle mode (large single-particle gaps, suppressed entanglement) and a gate mode (near-degenerate first excited levels inducing two-particle entanglement). Using this platform, we demonstrate coherent SWAP and $\sqrt{\text{SWAP}}$ protocols driven purely by electrostatic tuning of the Morse well, achieving high-fidelity population transfer and entanglement generation once appropriate single-qubit phase corrections are applied.

## 1.2  Goals

Achieving robust, electrostatic gates in a Morse double-well potential requires both methodological rigour and quantitative benchmarks. First, we must validate a numerical solver that captures both static and dynamic behavior of two-electron systems to high precision. Next, we need to identify optimal parameter configurations that isolate logical states, yet allow for fast entangling interaction. Having defined those, we must implement concrete gate protocols in time-domain simulations and finally, we must measure gate performance through standardized fidelity metrics to assess our implementation.

The thesis is structured around four main objectives:

1. **Numerical framework development**: Combine a grid based Sinc-Discrete Variable Representation (Sinc-DVR) with a product-state Hartree approximation to accurately solve both the time-independent and time-dependent Schrödinger equations for two interacting particles confined in a Morse double-well potential.

2. **Parameter optimization**: Identify two operational configurations—an *idle* mode with large single-particle energy gaps and suppressed entanglement, and a *gate* mode that enforces near-degeneracy of the first excited states to induce two-particle entanglement and population transfer.

3. **Time-evolution simulations**: Implement and test coherent SWAP and $\sqrt{\text{SWAP}}$ gate protocols by dynamically tuning the one-body potential, monitoring population transfer, entanglement generation and stability.

4. **Performance assessment**: Quantify gate performance through classical and average (coherent) fidelity measures, and apply appropriate phase corrections, and assess state leakage outside the logical subspace.

## 1.3  Thesis structure

The remainder of the thesis is organized as follows. In Chapter 2, we review the theoretical foundations necessary for our work: such as Dirac notation, operator formalism,

and basis-set expansions; the Hartree and configuration-interaction methods; the Morse potential model; time-evolution operator theory; measures of entanglement; and fidelity metrics. Chapter 3 describes our computational methods and implementation details, including system initialization, Sinc-DVR basis validation, the Hartree product approximation with configuration-interaction corrections, numerical propagators (Crank-Nicolson, matrix exponentiation, and ramp protocols), and the post-processing steps for phase correction and fidelity extraction. In Chapter 4, we present our results, starting with intermediate benchmarks of exchange shifts, DVR accuracy, and propagator performance; followed by optimized Morse-double-well configurations for the idle and gate modes; and concluding with time-domain simulations of SWAP and $\sqrt{\text{SWAP}}$ protocols along with detailed fidelity and entanglement analyses. Finally, Chapter 5 offers concluding remarks and outlook, summarizing the key findings, discussing implications for quantum-dot qubit architectures, outlining study limitations, and proposing directions for future work. Supplementary derivations and discussions—such as effective-mass conversions and the midpoint Hamiltonian formulation for Crank-Nicolson propagation—are collected in Appendix A.1.

# Chapter 2

# Theory

In this chapter, we lay out the theoretical foundations upon which this thesis is built, introducing what we consider to be the most essential aspects of quantum mechanics necessary for a clear understanding of the subsequent work. Although we presume that the reader possesses familiarity with quantum physics, we adopt a pedagogical approach throughout, gradually progressing from simple illustrative examples to more complex concepts. Our goal is to ensure the reader can comfortably follow the development of the project and grasp the methods and results presented in later chapters.

> *"Anyone who is not shocked by quantum theory has not understood it."*
>
> — Niels Bohr

We begin with a concise yet thorough review of the linear-algebraic framework underpinning quantum mechanics, including Dirac notation; operators and their properties; the concept of Hilbert spaces; and common basis sets. Collectively, these tools provide the language and mathematical structure necessary to describe quantum systems and their dynamics. Having established the framework, we then introduce the fundamental wave equation of quantum mechanics, the Schrödinger equation, which describes how quantum states evolve over time, including remarks on various numerical methods to solve this equation, like Hartree and Configuration Interaction theory. We discuss various numerical methods to solve this equation, notably Hartree and Configuration Interaction methods. Using these methods, we introduce the Morse double-well potential as our model quantum system and outline the theoretical framework underlying its (numerical) time evolution for analyzing the dynamics of an interacting two-particle system. Preliminary test results are provided to validate our numerical approaches and highlight the respective strengths of different methods in simulating quantum dynamics.

Next, we introduce the concept of entanglement, a uniquely quantum feature responsible for correlations between particles that defy classical explanations. We discuss how entanglement can be quantified and leveraged for quantum computational tasks, and we highlight the quantum mechanical phenomenon known as the avoided crossing. Finally, we conclude the chapter by introducing quantum logic and control protocols essential for practical quantum computing implementations. We outline the basic principles of quantum gates and demonstrate how our quantum system can implement both single- and two-qubit gates. To evaluate these gates' effectiveness, we discuss the concept of gate fidelity, a measure of a quantum gate's accuracy in performing its intended operation. Additionally, we describe methods for implementing phase-corrected single-qubit rotations to achieve higher gate fidelities.

Throughout this thesis, we employ atomic units ($\hbar = m_e = e = 4\pi\epsilon_0 = 1.0$). For a detailed derivation relating atomic units to SI units, see Appendix A.1; readers seeking further details may consult Chapter 2.1.1 in Szabo and Ostlund [26].

## 2.1  Linear Algebra

Before we tackle quantum mechanics itself, we first review the key linear-algebra tools that underpin it. Quantum mechanics is founded on the physics of waves and the language of linear operators, and a solid grasp of these topics will greatly aid our exploration of its more intricate features. In this thesis, we will be dealing with $n$-dimensional complex vector spaces, expressed in Dirac notation, which is a compact and powerful notation for linear algebra in quantum mechanics.

### 2.1.1  Dirac notation

Introduced and named by the famous physicist Paul Dirac in his paper 'A new notation for quantum mechanics' [27], this notation allows for linear algebra in quantum mechanics to be performed in a neat and compact way. Any $n$-dimensional complex vector in the vector space $V$ is represented as a ket, $|\psi\rangle$, and its dual-vector as a bra, $\langle\psi|$. The inner product of two vectors is then defined as:

$$\langle\psi|\phi\rangle = \int \psi^*(x)\phi(x)dx,$$

and any generic vector $|c\rangle$ can be expressed in a basis set $\{|i\rangle\}$ as:

$$|c\rangle = \sum_i c_i \, |i\rangle = \sum_i |i\rangle \, \langle i|c\rangle, \tag{2.1}$$

where $c_i$ are the coefficients of the expansion. This naturally introduces the *completeness relation*, where the following holds:

$$I = \sum_i |i\rangle \, \langle i|, \tag{2.2}$$

where $I$ is the identity operator. This relation guarantees that the basis set $\{|i\rangle\}$ spans the entire vector space $V$.

### 2.1.2  Operators

An operator is a mathematical object that maps elements from one vector space $V$ to itself (or, more generally, to a new vector space $W$)[28]. In this work, we focus on *linear operators*, i.e mappings $\hat{O} : V \to V$ that satisfy the following linearity properties:

$$\hat{O}(\alpha\mathbf{x} + \beta\mathbf{y}) = \alpha\hat{O}\mathbf{x} + \beta\hat{O}\mathbf{y},$$

for any $\mathbf{x}, \mathbf{y}$ in $V$ and $\alpha, \beta \in \mathbb{C}$. In the dirac notation then, we can write the following to show how an operator $\hat{O}$ acts on kets $|i\rangle$ in our space

$$\hat{O} \, |i\rangle = \alpha \, |i\rangle.$$

We can also define the adjoint of this operator, $\hat{O}^\dagger$, which acts on the dual-vectors, the bras, in the same space

$$\langle i| \, \hat{O}^\dagger = \alpha^* \, \langle i|.$$

One of the most useful properties of linear operators, is that given a basis $\{|i\rangle\}$, we can express the operators as matrices, where the matrix elements are as follows

$$O_{ij} = \langle i| \, \hat{O} \, |j\rangle = \sum_k \langle i|k\rangle \, O_{kj},$$

and we can identify the action of the operator on the vector in this basis, as a matrix-vector product

$$\hat{O} |i\rangle = \sum_j |j\rangle O_{ji}.$$

In quantum mechanics, certain operators play a fundamental role due to their specific mathematical properties [28, 29]. These operators represent key physical observables and transformations, which we will explore in detail in the quantum mechanics section. However, some of their defining mathematical characteristics are crucial to emphasize:

- **Unitary:** A matrix $U$ is unitary if $U^*U = I$, meaning the inverse of the matrix $U$ is it's complex conjugate. This property of unitary matrices is such that they preserve the inner product of vectors, e.g $\langle\psi|\phi\rangle = \langle U\psi|U\phi\rangle$, and the unitary matrices also preserve the vector norm. Unitary matrices are used to represent time-evolution operators in quantum mechanics.

- **Hermitian:** A matrix $U$ is hermitian if $U = U^\dagger$, meaning the matrix is equal to its complex conjugate transpose[1]. This is a special case of self-adjoint operators, living in a *complex* Hilbert space, where the eigenvalues are real and the eigenvectors are orthogonal. These matrices are used to represent physical observables in quantum mechanics, like the Hamiltonian operator, which represents the total energy of a quantum mechanical system.

### 2.1.3  Hilbert spaces

The concept of a Hilbert space is fundamental to quantum mechanics, as it provides the mathematical framework for which quantum states and operators are defined. A Hilbert space is a generalization of Euclidiean space, which allows for linear algerba and calculus to be applied to infinite-dimensional spaces. More formally, a Hilbert space is a complex complete inner product space, which means that it adhers to the following properties [28, 29]:

- **Completeness:** Every Cauchy sequence $\{x_n\}$ in the space $V$ converges to a limit in the space. Specifically, $V$ is complete if:

$$\forall \epsilon > 0, \quad \exists N \in \mathbb{N} : |x_n - x_m| < \epsilon, \quad \forall n, m > N. \tag{2.3}$$

- **Positivity:** The inner product of a vector with itself is always positive, and zero if and only if the vector is the zero vector. That is:

$$\langle\phi|\psi\rangle \geq 0, \quad \text{and} \langle\phi|\phi\rangle = 0 \iff |\phi\rangle = |0\rangle. \tag{2.4}$$

- **Multiplicativity:** The inner product is linear in the second argument and conjugate linear in the first argument, meaning:

$$\langle\beta\phi|\alpha_1\psi_1 + \alpha_2\psi_2\rangle = \alpha_1\beta^* \langle\phi|\psi_1\rangle + \alpha_2\beta^* \langle\phi|\psi_2\rangle. \tag{2.5}$$

The choice for conjugate linearity in the first agrument is by convention in many physics textbooks. Vectors living in Hilbert space is in quantum mechanics often coined state-vectors. As we mentioned, a Hilbert space is an inner product space, and we define the inner product on the space $V$ as

$$\langle\phi|\psi\rangle = \int \phi^*\psi dx,$$

---

[1]represented by a $\dagger = *^T$

for the complex-valued, continuous, state vectors $|\phi\rangle, |\psi\rangle \in V$.

We can use this inner product to define *orthogonality* in the Hilbert space

$$\langle \psi_i | \psi_j \rangle = \delta_{ij},$$

where $\delta_{ij}$ is the Kronecker delta. This orthogonality relation is crucial in quantum mechanics, as it allows us to define a basis set of vectors that are orthogonal to each other. As elegant as this framework may be, the challenge of quantum many-body systems lies in the exponential scaling of the Hilbert space with the number of particles and degrees of freedom. For a system of $N$ particles, with $d$ degrees of freedom, the dimension of the Hilbert space is $d^N$, which quickly becomes intractable for classical computers. This rapid growth makes exact solutions for interacting many-body systems computationally infeasible, even in low-dimensional systems [26, 30].

### 2.1.4   State representation

The representation of state-vectors in a Hilbert space is not unique, and we are free to choose basis sets to express the vectors that span our Hilbert space (or any space for that matter), as long as the basis of choice spans the Hilbert space [28, 29]. This is a powerful tool, as it allows us to choose the basis that best suits the problem at hand, and clever choices can simplify problems significantly. The flexibility in choosing a basis set is central to both theoretical insights and computational efficiency when solving quantum mechanical problems [26, 30].

Many modern many-body methods are built upon this principle, where the choice of basis set can make the difference between a computationally infeasible problem and a tractable one. For example, by exploiting symmetry, localization, or energy scales, we can often reduce the dimensionality of the problem and focus on the most relevant degrees of freedom. The choice of basis is not just a mathematical convenience, it can also yield physical insights into system's behaviour. For instance, in quantum chemistry, the choice of basis set can reflect the underlying symmetries of the molecular structure, leading to a more efficient representation of the wavefunction and its properties. Similarly, in condensed matter physics, the choice of basis can be guided by the crystal structure or electronic correlations present in the material [31, 32].

Furthermore, by finding a basis that diagonalizes the Hamiltonian matrix, we can directly solve for the energy eigenvalues and eigenstates. This principle underlies many techniques, such as using harmonic oscillator eigenfunctions for bound systems or plane waves for periodic potentials [29, 32]. The search for an optimal basis is often guided by the specific features of the system under study, such as symmetry or localization, making it a central consideration in both theoretical and computational approaches to quantum mechanics.

Because no single basis is optimal for every task at hand, we are often required to re-express states and operators in different bases during calculations, depending on the problem and what we are currently studying.

The transformation between two basis sets $\{|i\rangle\}$ and $\{|\alpha\rangle\}$ is given by the unitary transformation matrix $U$:

$$|\alpha\rangle = \sum_i U_{\alpha i} |i\rangle,$$

where the matrix elements of $U$ are given by the inner product of the basis vectors:

$$U_{\alpha i} = \langle \alpha | i \rangle,$$

here assuming the basis sets are complete, meaning they obey the completeness relation 2.2:

$$\sum_i |i\rangle \langle i| = \sum_\alpha |\alpha\rangle \langle \alpha| = I.$$

This relation allows the insertion of the identity operator in calculations, to expand state-vectors and operators in the basis of our choice. This underpins many mathematical tools in quantum mechanics, from the spectral decomposition of operators [2] to perturbation-theory expansions [28, 29, 34].

We can also study how the matrix representation of an operator change under a basis transformation between complete orthonormal basis sets [26]. Assume that $\hat{O}$ is an operator in the basis $\{|i\rangle\}$, and $\hat{O}'$ is the same operator expressed in the basis $\{|\alpha\rangle\}$, then the transformation between the two operators is given by:

$$O'_{\alpha\beta} = \langle\alpha|\hat{O}|\beta\rangle = \sum_{ij} \langle\alpha|i\rangle \langle i| \hat{O} |j\rangle \langle j|\beta\rangle = \sum_{ij} U_{\alpha i} O_{ij} U^\dagger_{j\beta}.$$

We have the following transformation rule for operators under a basis transformation:

$$\hat{O}' = U\hat{O}U^\dagger,$$
$$\hat{O} = U^\dagger\hat{O}'U,$$

which allows us to freely move between coordinate, momentum, energy or grid-based representations as needed.

### 2.1.5  Basis sets

As we have mentioned, the choice of basis is essential for controlling error, even though there is no uniquely 'correct' basis and one must often settle on a convenient or computationally efficient option. Any complete set of orthonormal vectors can be used to express our state-vectors, and there are numerous choices available, each with its own advantages and disadvantages. The choice can greatly affect computational efficiency, numerical stability and the physical insights gained from the calculations. We will briefly outline some of the most common families of basis sets, and their usages before we present our choice in this thesis:

- **Discrete Variable Representation (DVR):** A grid-based approach that discretizes the continuous space into a finite set of points, with one basis function peaked at each grid point. This method makes coordinate operators diagonal in the basis, retaining analytical expressions for the kinetic energy operator making it both efficient and accurate for smooth potentials [35].

- **Harmonic oscillator basis:** A set of orthonormal functions that are solutions to the quantum harmonic oscillator (QHO) problem. As such, these are useful for bound systems exhibiting oscillatory behaviour, such as vibrational modes of molecules and quantum dot systems [30].

- **Plane wave basis:** The natural choice for representing periodic systems, such as crystals, and is often employed in condensed matter physics. Their diagonalization of the kinetic energy operators makes them particularly useful for systems with translational symmetry, such as electrons in a crystal lattice [32].

- **Gaussian-type orbitals (GTOs):** Common choice for initial approximations in quantum chemistry, particularly in the Hartree-Fock method. GTOs are computationally efficient, and reflect the atomic symmetries of atoms, making them suitable for molecular systems [26].

---

[2]See for example chapter 5.5 in [33]

- **Energy eigenfunctions:** The eigenfunctions of a chosen reference Hamiltonian (such as the QHO)form an orthonormal set that diagonalizes the Hamiltonian operator. For example, the static or unperturbed system Hamiltonian can be used to construct a basis set of energy eigenfunctions, and using these states makes unperturbed time-evolution trivial, as the time-evolution operator is diagonal in this basis. This is a common approach in quantum chemistry and condensed matter physics. The downside is that for many-body systems, the number of states required to accurately express the wavefunction grow exponentially, and computing the eigenstates of the Hamiltonian becomes intractable [26, 30].

We focus on the Sinc-DVR basis [36] for the analysis done in our thesis work, due to its simple structure and wide applicability to problems with smooth, localized potentials. The Sinc-DVR basis functions form an orthonormal set on a uniformly spaced spatial grid, and exhibit Kronecker delta-like behaviour at the grid points, making them especially suited for representing localized states and sparse Hamiltonians, such as our bounded Morse double well system. For some analyses we will also use the energy eigenfunctions of the unperturbed system Hamiltonian, mostly to validate and compare results obtained in the Sinc-DVR basis.
The Sinc-DVR basis funtions are mathematically defined as

$$\phi_n(x) = \frac{1}{\sqrt{N}} \text{sinc}\left(\frac{x - x_n}{\Delta x}\right), \tag{2.6}$$

where $N$ is the number of grid points, $x_n$ is the $n$th grid point, and $\Delta x$ is the grid spacing. The Sinc function is defined as

$$\text{sinc}(x) = \begin{cases} \frac{\sin(\pi x)}{\pi x} & \text{if } x \neq 0, \\ 1 & \text{if } x = 0. \end{cases}$$

These basis functions are orthonormal, meaning that they satisfy the following relation:

$$\int_{-\infty}^{\infty} \phi_n(x)\phi_m(x)dx = \delta_{nm},$$

where $\delta_{nm}$ is the Kronecker delta function. This orthonormality property is crucial for ensuring that the basis functions can be used to represent quantum states accurately, and results in the Hilbert space being spanned by the basis functions. We shall in later sections discuss further on how we chose to implement the Sinc-DVR basis in our code, by number of grid points, grid spacing etc.
In the Discrete Variable Representation, the kinetic energy operator is expressed in matrix form using a grid-basis. In atomic units, this operator is given by

$$T = -\frac{1}{2}\frac{d^2}{dx^2},$$

and the Sinc-DVR function defined on a uniform grid as in (2.6). The kinetic energy operator matrix elements are then given by

$$T_{nm} = \langle \phi_n| -\frac{1}{2}\frac{d^2}{dx^2}|\phi_m\rangle.$$

Using the known analytical solution of these integrals with the sinc function properties (see for example Appendix A in [36]), these matrix elements take the form

$$T_{nm} = \begin{cases} -\frac{\pi^2}{6\Delta x^2} & \text{if } n = m, \\ \frac{(-1)^{(n-m)}}{\Delta x^2(n-m)^2} & \text{if } n \neq m. \end{cases} \tag{2.7}$$

This provides us with a simple matrix expression for the Sinc-DVR Hamiltonian that is easily implemented numerically, as it removes the need for numerical differentiation.

To compute the Coulomb interaction matrix elements in the Sinc-DVR basis, we start from the general form of the Coulomb interaction between two particles with the shielded Coulomb potential:

$$V_{nmpq} = \int \int \phi_n(x_1)\phi_m(x_2) \frac{\alpha}{|x_1 - x_2| + a^2} \phi_p^*(x_1)\phi_q^*(x_2) dx_1 dx_2,$$

where $\alpha$ is the Coulomb constant, and $a$ is a small shielding parameter to avoid singularities when the particles are very close together. In the DVR basis, this integral becomes a double sum over the grid points with weight $\Delta x^2$. Since each basis function is peaked at a grid point, it satisfies the delta-like property

$$\phi_n(x_i) = \frac{1}{\sqrt{\Delta x}}\delta_{n,i}.$$

Inserting this property into the 4-index two-body integral all four indices collapse via the Kronecker delta. One can then show that the interaction matrix elements in the Sinc-DVR basis are given by

$$V_{nmpq} = \sum_{i,j} \frac{1}{\Delta x^2}\delta_{n,i}\delta_{m,j} \frac{\alpha}{|x_i - x_j| + a^2}\delta_{p,i}\delta_{q,j}\Delta x^2.$$

where we have assumed a uniform grid spacing $\Delta x_1 = \Delta x_2 = \Delta x$. This gives us the final $N \times N$ interaction matrix elements

$$V_{nm} = \frac{\alpha}{|x_n - x_m| + a^2} \tag{2.8}$$

and it is clear that the interaction matrix is sparse in the Sinc-DVR basis, since the basis functions are highly localized at the grid points. This sparsity significantly reduces the computational cost of evaluating the interaction elements as they are often zero, or negligible. As a result, the Sinc-DVR approach is particularly well-suited for systems with local interactions and enables efficient numerical simulations of quantum systems with large basis sets [37].

## 2.2  Quantum Mechanics

### 2.2.1  The Schrödinger equation

The physical description of any quantum system, i.e the *state space*, is given by the quantum mechanical *wavefunction* (also often called a *state vector*) [38], which in Dirac notation is written as $|\Psi(t)\rangle$. This function is a complex-valued function that gives a complete description of both static and dynamic properties of a given quantum system, and thus presents the analogue to the classical notion of a set of trajectories in phase space [39].

The dynamics of the wavefunction is governed by the *Time-dependent Schrödinger Equation* (TDSE)

$$i\frac{\partial}{\partial t}|\Psi(x,t)\rangle = H(x,t)|\Psi(x,t)\rangle, \tag{2.9}$$

where $H$ a linear hermitian operator often referred to as the *Hamiltonian* [28, 29]. Here $x$ is the position of the particle, and $t$ is the time. This operator describes the total energy of the system, and is given by (in atomic units)

$$H = \frac{-\nabla^2}{2} + V(x),$$

where $\nabla^2$ is the Laplacian operator, and $V(x)$ is the potential energy of the system, both external and internal. This equation gives the equation of motion for the wavefunction, and describes how the wavefunction evolves in time. Atomic units (a.u) transform fundamental constants like the speed of light $c$, Planck's constant $\hbar$, and the electron mass $m_e$ to unity, to simplify equations and calculations. This is a common practice in quantum mechanics, as it allows for easier manipulation of the equations without loss of generality. In this notation, lengths are measured in Bohr radii ($a_0 = 0.529$Å) and energies in Hartrees (Ha $= 27.211eV$) [26].

While the TDSE governs the time-evolution of the quantum system, many problems—particularly stationary or bound-state problems—are often more easily analysed through the *Time-independent Schrödinger Equation* (TISE), which is obtained by separating the temporal and spatial variables in the TDSE. This gives us

$$H \left| \psi_n(x) \right\rangle = E_n \left| \psi_n(x) \right\rangle, \tag{2.10}$$

where $\psi_n(x)$ are the *energy eigenstates* of the system, and $E_n$ are the corresponding *energy eigenvalues*. As is clear from equation (2.10), the energy eigenvalues are the diagonal elements of the diagonalized Hamiltonian operator. In practice, these eigenvalues are obtained by diagonalizing the Hamiltonian operator (regardless of time-dependency), and the associated eigenvectors form a basis of energy eigenfunctions.

The energy eigenstates are the stationary states of the system, and they form a complete orthonormal basis for the Hilbert space of the system. This means that any wavefunction can be expressed as a linear combination of the energy eigenstates, and in our work, it will serve as an important reference point to validate our choice of basis sets. To be precise, any state function $\Psi(x, t)$ can be expressed as a linear combination of the energy eigenstates $\psi_n(x)$ as

$$\Psi(x, t) = \sum_n c_n \psi_n(x),$$

where $c_n$ are the coefficients of the linear combination, which are determined by the initial conditions of the system. This is a direct consequence of the linearity of the Schrödinger equation, and it allows us to express any state function as a superposition of energy eigenstates [28, 29].

### 2.2.2 Hartree approximation

Accurately solving the Schrödinger equation for many-body systems is a formidable challenge—even a one-dimensional system with just a few interacting particles can become intractable very quickly. The core difficulty stems from the exponential growth of the Hilbert space as we add more degrees of freedom, coupled with particle interactions and, for identical particles, the need to enforce antisymmetry (the Pauli exclusion principle). In real-world applications—like molecular dynamics or solid-state physics, we often invoke the Born-Oppenheimer[3] approximation to freeze out the nuclear motion, which drastically reduces the size of the electronic Hilbert space [26, 30]. Even after that simplification, however, finding an exact solution on a classical computer remains out of reach for systems of more than a few particles.

Mean-field theory offers a practical way to approximate the many-body problem by replacing the full interacting Hamiltonian with an effective single-particle picture in which each particle feels an average field created by all the other particles. This means, solving $N$ coupled single-particle equations instead of the full many-body problem. The most widely used mean-field method is the Hartree-Fock (HF) method. Here the trial wavefunction is a single

---

[3]Formulated by Max Born and Robert J. Oppenheimer in their 1927 paper [40]

Slater determinant[4] of orthonormal orbitals, thereby incorporating both Coulomb (direct) and exchange interactions automatically [26, 30]. In the simpler Hartree approximation, we drop exchange entirely and assume the $N$-particle wavefunction can be approximated as a product of $N$ single-particle orbitals.

Both the HF and the Hartree methods build on the variational principle, which guarantees that the expectation value of the energy

$$E[\Psi] = \frac{\langle \Psi | H | \Psi \rangle}{\langle \Psi | \Psi \rangle}, \tag{2.11}$$

is always an upper bound to the true ground state energy $E[\Psi] \geq E_0$. By choosing a trial wavefunction $\Psi$ with adjustable parameters (here, the single-particle orbitals), and minimizing the energy functional $E[\Psi]$, we derive a set of self-consistent one-particle equations: each orbital satisfies its own Schrödinger-like equation that contains the kinetic and external potential as usual with an additional mean-field Coulomb potential from the density of the other orbitals (particles)[30][5].

In a discrete basis this becomes a matrix eigenproblem for the so-called *Hartree* matrix, whose elements combine the one- and two-body integrals of the Hamiltonian, weighted by the current orbital coefficients. Because every orbital is coupled to every other orbital's effective Hamiltonian, the equations must be solved iteratively (self-consistently) until convergence is reached (self-consistency). One starts from a guess for the orbitals, computes the Hartree matrix, diagonalizes it to obtain new orbitals, and repeats this process until the orbitals no longer change significantly. This self-consistent procedure is the essence of the Hartree-Fock and the Hartree methods. Although the Hartree product does not enforce anti-symmetry or exchange, it captures the leading direct Coulomb interaction between particles at modest computational cost, and is often sufficient for many practical applications, especially in systems where particles are well-separated or localized, such as in our double-well system.
The orbitals that build the Hartree product are the solution of the one-electron Schrödinger equation

$$\hat{h}\phi_i = \epsilon_i \phi_i,$$

where the full Hamiltonian (for a non-interacting) system would be

$$H = \sum_{i=1}^{N} \hat{h}_i,$$

which has the solution eigenvector

$$\Psi = \phi_1(\mathbf{r}_1)\phi_2(\mathbf{r}_2)...\phi_N(\mathbf{r}_N), \tag{2.12}$$

with corresponding eigenvalue $E = \epsilon_1 + \epsilon_2 + ... + \epsilon_N$, i.e. the sum of single-particle energies. Equation (2.12) is the Hartree product, and it is the simplest possible wavefunction for a many-body system. As is evident, this Hartree product is not anti-symmetric, nor indistinguishable, as the particles are designated a specific orbital to occupy and thus they are distinguishable, and the state is symmetric under particle exchange. In our double-well system, the two particles remain localized in separate wells and therefore behave like distinguishable subsystems rather than identical fermions, which is why we choose to solve our system using the Hartree method.

---

[4]We refer the reader to ch. 2.2.3 in [26] for details on the Slater Determinant
[5]We refer the reader particularly to chapter 4.2 in [30]

To derive this method, we select a finite basis set $\{\chi_\alpha\}$ for each subsystem $M$ (left or right well), and expand the single-particle Hartree orbitals in this basis.

$$|\phi_i^M\rangle = \sum_{\alpha=1}^{N^M} C_{\alpha i}^M |\chi_\alpha\rangle,$$

where $N^M$ is the number of single-particle basis functions in subsystem $M$. The Hartree product state for our two-particle system can then be expressed as a product of the single-particle Hartree orbitals for each subsystem, i.e. $|\phi_i^A\rangle$ and $|\phi_j^B\rangle$, where $i, j$ are the orbital indices for subsystems A and B respectively. We can then also define the two necessary integrals, the one-body integrals and the two-body interaction integrals, as

$$h_{\alpha\beta}^M = \langle \chi_\alpha^M | h^M |\chi_\beta^M\rangle = \int \chi_\alpha^{M*} h^M \chi_\beta^M d\mathbf{r},$$

$$u_{\alpha\beta,\gamma\delta} = \langle \chi_\alpha^M \chi_\beta^N | u^{MN} |\chi_\gamma^M \chi_\delta^N\rangle, = \int \chi_\alpha^{M*} \chi_\beta^{N*} u^{MN} \chi_\gamma^M \chi_\delta^N d\mathbf{r}_M d\mathbf{r}_N,$$

where $h^M$ is the single-body Hamiltonian for subsystem $M$, and $u^{MN}$ is the two-body interaction between subsystems $M$ and $N$. The two-body interaction is the Coulomb interaction between the two subsystems. Due to the nature of our system, where the particles occupy distinct wells, we can omit the otherwise present exchange term in the two-body interaction integral and only the direct coulomb interaction remains.

The groundstate wavefunction will then have the following form:

$$|\Psi\rangle = |\phi_0^A \phi_0^B\rangle,$$

where $\phi_0^M$ is the single-particle Hartree functions (orbitals) for subsystem $M \in [A, B]$, with the constraint that these single-particle orbitals are orthonormal. We can set up the Lagrangian

$$L = E_H - \lambda^A(\langle\phi_0^A|\phi_0^A\rangle - 1) - \lambda^B(\langle\phi_0^B|\phi_0^B\rangle - 1),$$

where $\lambda^M$ are the Lagrange multipliers, and $E_H$ is the Hartree energy, which is the expectation value of the Hamiltonian in the Hartree product state

$$E_H = \langle\Psi| H |\Psi\rangle = \langle\phi_0^A| h^A |\phi_0^A\rangle + \langle\phi_0^B| h^B |\phi_0^B\rangle + \langle\phi_0^A \phi_0^B|u^{AB}|\phi_0^A \phi_0^B\rangle,$$

here $h^M$ are the single-body Hamiltonian, for each subsystem and $u^{AB}$ the mean-field Coulomb interaction between subsystems. The Hartree orbitals can be expanded in our single-particle basis set, as linear combinations,

$$|\phi_i^M\rangle = \sum_{\alpha=1}^{N^M} C_{\alpha i}^M |\chi_\alpha\rangle,$$

where $N^M$ is the number of single-particle basis functions in subsystem $M$. Minimizing the Lagrangian by the basis transformation coefficients $C_{\alpha 0}^M$ gives us two coupled eigenvalue equations, i.e calculating $\partial L/\partial C_{\alpha 0}^{M*} = 0$ for $M \in [A, B]$ yields

$$\frac{\partial L}{\partial C_{\alpha 0}^{A*}} = \sum_{\beta=0}^{N_A} (h_{\alpha\beta}^A + \sum_{\gamma\delta=0}^{N_B} C_{\gamma 0}^{B*} u_{\alpha\gamma,\beta\delta} C_{\delta 0}^B) C_{\beta 0}^A = \lambda^A C_{\alpha 0}^A,$$

$$\frac{\partial L}{\partial C_{\alpha 0}^{B*}} = \sum_{\beta=0}^{N_B} (h_{\alpha\beta}^B + \sum_{\delta\gamma=0}^{N_A} C_{\delta 0}^{A*} u_{\delta\alpha,\gamma\beta} C_{\gamma 0}^A) C_{\beta 0}^B = \lambda^B C_{\alpha 0}^B, \tag{2.13}$$

where $_{\alpha\beta} = \langle \chi_\alpha^M | h^M | \chi_\beta^M \rangle$ are the one-body integrals, and $u_{\alpha\beta,\gamma\delta} = \langle \chi_\alpha^M \chi_\beta^N | u^{MN} | \chi_\gamma^M \chi_\delta^N \rangle$ are the two-body interaction integrals.

These eigenvalue equations are for subsystem A and B respectively, and we can identify the Hartree matrix as the left-hand side inside the big parenthesis. These two coupled equations are solved iteratively, by updating the coefficients $C_{\alpha 0}^M$ until convergence is reached (self-consistency). By diagonalization of these Hartree matrices we gain the $N_M$ lowest energy orbitals $C_{\alpha i}^M$ and energy levels $\lambda_i^M = \epsilon_i^M$ [21], which we will use as our single-particle basis for each subsystem. The equations to be solved are

$$\sum_{\beta=0}^{N_M} f_{\alpha\beta}^M C_{\beta i}^M = \epsilon_i^M C_{\alpha i}^M, \tag{2.14}$$

with the Hartree matrices from eqs. (2.13). From this we identify the *Hartree operator*

$$f_{\alpha\beta}^M = h_{\alpha\beta}^M + \sum_{\gamma,\delta=0}^{N_{\bar{M}}} C_{\gamma 0}^{\bar{M}*} u_{\alpha\gamma,\beta\delta} C_{\delta 0}^{\bar{M}}. \tag{2.15}$$

This method to solve the interacting many-body problem is called the Hartree method, and is a simplification of the Hartree-Fock method where Hartree product states are applied, instead of anti-symmetric Slater determinants. This method will naturally introduce a mean-field coulomb interaction between our two subsystems into their respective basis sets, and will be the basis for our study of the two-particle system [21].

### 2.2.3 Configuration Interaction

Configuration Interaction (CI) refines the mean-field Hartree solution by expanding on the Hartree product state to include all possible configurations of the particles. The exact two-body wavefunction is then expanded in a basis of *correlated* product states, which are constructed from the single-particle Hartree orbitals. This allows us to account for all possible correlations between the particles, and thus obtain a more accurate description of the system. If we include all possible configurations (i.e infinite number of basis states) we obtain Full Configuration Interaction (FCI), which is the exact solution to the many-body problem, but is intractable for all but the smallest systems [26, 30].

Starting from the Hartree orbitals for subsystems A and B (obtained by solving the eigenvalue equations 2.14), we can collect a truncated set of single-particle orbitals, $\{\phi_i^A\}$ and $\{\phi_j^B\}$, where $i, j < N$ are the orbital indices for subsystems A and B respectively, and $M = N^2$ is the number of single-particle orbitals we include in our basis set, and construct all possible two-particle product states

$$\phi_i^A(\mathbf{r}_1)\phi_j^B(\mathbf{r}_2).$$

As mentioned, retaining all such product states leads to the exact solution within the one-particle basis approximation, but due to the combinatorial explosion of the number of product states, we choose to truncate the basis set and include $N$ function in each subsystem.

To enforce the Pauli exclusion principle—and regaining exchange effects omitted by the distinguishable-particle Hartree product—we construct anti-symmetrized linear combinations of the Hartree product states. Each such unordered pair $(i, j)$ gives a Slater-type state

$$|\Psi_{ij}\rangle = \frac{1}{\sqrt{2}}(\phi_i^A(\mathbf{r}_1)\phi_j^B(\mathbf{r}_2) - \phi_j^A(\mathbf{r}_1)\phi_i^B(\mathbf{r}_2)),$$

which is equivalent to the Slater determinant for two particles in two different subsystems, that is, when accounting for the strict localization of the two particles the particle-swap terms are zero in the determinant. We desire these anti-symmetrized energies to compare with our product state solution.

Gathering all unique such pairs $i < j$ of Slater-type states, yields a basis set of $N^2$ two-particle states. We then build the many-body Hamiltonian matrix in this basis set, which is given by

$$H_{ij,kl} = \langle \Psi_{ij} | H | \Psi_{kl} \rangle = \langle \phi_i^A \phi_j^B | H | \phi_k^A \phi_l^B \rangle ,$$

by evaluating the one- and two-body integrals in the truncated CI basis, and diagonalizing it to obtain the CI eigenvalues and eigenvectors.

### 2.2.4   Morse potential

To build our qubit system, we need to define some form of potential trap that we can confine our particles within. In modern quantum computing many different potentials are used, tested and theorized. One of the most common potentials is the Quantum Harmonic Oscillator potential (QHO), a very well known potential in quantum mechanics. This potential has been studied in great detail and has been used in many different quantum systems, and is very often used as a benchmark for more advanced symmetric potentials [28, 29]. The QHO basis sets are widely employed to study quantum dot systems [41], and are often used in quantum chemistry to describe molecular vibrations [42].

One could think that using the QHO potential for our qubit would be a natural choice, but there are some nuances necessary to consider. The QHO double well potential is perfectly symmetric, meaning the energy levels are uniformly spaced, and equal across both wells. This is not ideal for qubit systems, as we need more control over energy levels in both wells and the uniform energy spacing makes one-qubit operations unstable as we lack control over what energy levels we excite [43].

#### Single-well Morse potential

To achieve this, we will instead use the Morse potential, first introduced by Philip M. Morse in 1929 as a solution to the Schrödinger equation representing the motion of the nuclei in a diatomic molecule [22]. This potential has non-uniform energy levels, and more parameters, and is widely used in quantum mechanics to describe anharmonic oscillators. An extension of the Morse potential, Morse/Long-range potential is one of the most popular potentials to model potential energy surfaces used for spectroscopy [44] in chemical physics. Given that this potential has already been extensively studied within quantum-dot systems, and molecular systems in general, it is natural to expect that—should our study succeed—it could prove to be a promising candidate for a prototype (near-)room-temperature qubit system [45–47].
The Morse potential is given as

$$V(r) = De^{-2a(r-r_0)} - 2De^{-a(r-r_0)}.$$

This function has a minima of $-D$ at $r = r_0$, and goes asymptotically towards zero at $r = \infty$, and tends towards large values for $r \to 0$. In our study, we will rewrite the potential somewhat, to make it more computationally efficient to make multiple evaluations. As the zero-point of a potential is arbitrary, we can subtract or add any scalar value without loss of generality. We will therefore rewrite the Morse potential, adding the zero-point energy $D$ to the potential, and

factor out a $D$ to simplify the expression. This gives us

$$V(r) = De^{-2a(r-r_0)} - 2De^{-a(r-r_0)} + D$$
$$= D(e^{-2a(r-r_0)} - 2e^{-a(r-r_0)} + 1),$$

which yields a simpler form, by factorization using the square binomial formula

$$V = D(e^{-a(r-r_0)} - 1)^2, \tag{2.16}$$

where now, computationally, we need only evaluate the exponential function once, and the rest of the potential is given by simple algebraic operations. Here the $D$ parameter is the dissociation energy, which is the depth of the potential well, and $a$ is a parameter that controls the width of the well, and thus the curvature of the potential. The parameter $r_0$ is the position of the well minima, and can be used to shift the potential to any desired position.

Expanding a Taylor series about the well minima, we can see that the potential is approximately harmonic. From this, we can identify Hookes law, and also identify the spring constant in this potential. Expanding around $r_0$

$$V(r) = V(r_0) + V'(r_0)(r - r_0) + \frac{1}{2}V''(r_0)(r - r_0)^2 + ...,$$

and, since we are operating around the minima, higher order terms can be neglected as they become very small ($\mathcal{O}(\Delta r^n)$). By shifting the zero point of the potential to $r_0$, we have $V(r_0) = 0$. Furthermore, as $r_0$ is a minima of the potential, $V'(r_0) = 0$, as the slope of the potential function is flat at this point. This simplifies our expression to

$$V(r) = \frac{1}{2}V''(r_0)(r - r_0)^2,$$

which we recognize as the harmonic oscillator potential with spring constant $k = V''(r_0)$, Differentiating this potential with respect to $r$, we obtain the force acting on the particle, thus recovering Hooke's law [23]. This gives us a new parameter to control the width of the well, and the curvature of the potential, which is expressed as

$$V' = 2D(1 - e^{-a(r-r_0)})a$$
$$V'' = 2Da^2 e^{-a(r-r_0)}$$
$$V''(r_0) = 2Da^2$$
$$k = 2Da^2 \rightarrow a = \sqrt{\frac{k}{2D}}.$$

Figure 2.1 shows the Morse potential, with the 5 lowest energy levels and corresponding energy eigenfunctions.

This potential admits closed form solutions to the Schrödinger equation [22, 23], and the energy eigenstates are given by

$$\psi_n(z) = N_n e^{-\frac{z}{2}} z^{\lambda-n-\frac{1}{2}} L_n^{(2\lambda-2n-1)}(z), \quad z = 2\lambda e^{-a(r-r_0)}, \quad \lambda = \frac{D}{a^2}, \tag{2.17}$$

where $L_n^{(\alpha)}$ are the generalized Leguerre polynomials, and the normalization constant $N_n$ is given by

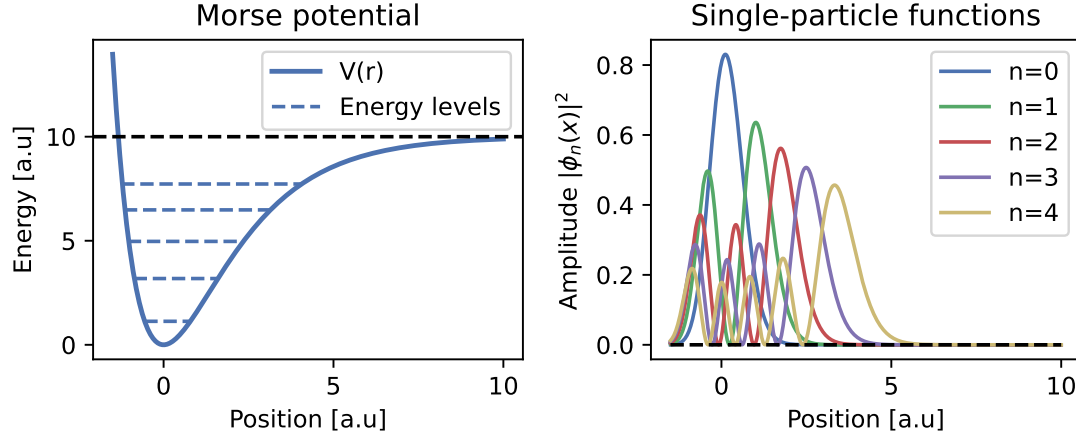$$N_n = \sqrt{\frac{n!(2\lambda - 2n - 1)a}{\Gamma(2\lambda - n)}}.$$

Figure 2.1: The Morse potential and the 5 lowest energy levels and energy eigenfunctions. The dissociation energy, $D$, is highlighted by the black dashed line, and the parameters for this visualization of a Morse potential are $D = 10, a = 0.5, r_0 = 0$. We can see how the lowest lying states are populated near the well minima, while the higher order states are spreading out further towards the dissociation curve (to the right), as opposed to the potential wall at the left side. The energy levels are anharmonic, and the spacing non-uniform, as is expected from the Morse potential.

These energy eigenstates are the solutions to the Schrödinger equation for the Morse potential, with the corresponding energy eigenvalues

$$E_n = -D + h\nu(n + \frac{1}{2}) - \frac{ah\nu}{\sqrt{8D}}(n + \frac{1}{2})^2, \quad n = 0, 1, 2, ..., \tag{2.18}$$

where $h$ is Planck's constant, $n$ the vibrational quantum number, and $\nu = \frac{a}{2\pi}\sqrt{2D/m}$ is the characteristic frequency of the potential, with $m$ being the mass of the particle. The first term is the zero-point energy, the second term is the harmonic oscillator energy, and the third term is the anharmonic correction to the energy levels. The anharmonicity of the Morse potential gives us a non-uniform energy spacing, which is crucial for our qubit system, as it allows for independent control of specific energy states [22, 23].

**Double-well Morse potential**

We make a potential trap for *two* separate particles, as our qubit system will be a two-particle system. To do so, we construct a double Morse potential well, simply by adding two Morse potentials together. We flip the right potential well, so that the minima are at the same position, and the potential is symmetric (given symmetric parameters, i.e same parameter for each well). This gives us the double Morse potential as

$$V(r) = D_L(e^{-a_L(r-r_{0,L})} - 1)^2 + D_R(e^{a_R(r-r_{0,R})} - 1)^2, \tag{2.19}$$

where the subscripts L and R correspond to left and right well, respectively. The parameter $D$ controls the depth of the potential well, whilst $a$ has some control over the width of the well, through the steepness of the exponential functions decay (and thus the curvature, and width, of the well). A smaller $a$ parameter constitutes a wider well as the function would then decay slowly. Recall also the $a$ parameter's relation with the spring-like constant $k = 2Da^2$, which is the parameter we shall use in our numerical implementations. The parameter $r_0$ is the position of the well minima. It is this potential that we shall study in great detail in this thesis, and we will use it to construct our qubit system. The parameters will be tuned throughout the time-evolution to achieve the desired energy level structure, and thus control the qubit system parametrically.
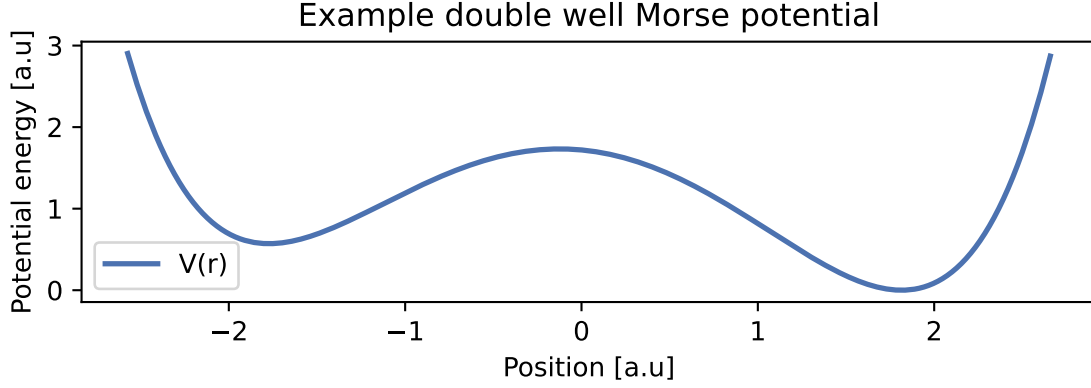
Figure 2.2: A visual representation of the double Morse potential, with the two wells, and the energy levels. Parameters for this visualization are $D_L = 10$, $D_R = 11$, $k_l = 7$, $k_r = 7$, $r_{0,L} = -2$, $r_{0,R} = 2$, with a grid length of 5.3, with $N = 400$ grid points. The deviation between well depths ($D_L \neq D_R$) is what gives the asymmetrical shape of the potential, and subsequently will give degenerate single-particle energy levels.

Figure 2.2 shows the double Morse potential with the two wells. This is an example visualization, and shows how the qubit system can be constructed by tuning the parameters of the potential and placing a single particle in each well minima. With a sufficiently high barrier between the two wells, we can ensure that the particles remain localized in their respective wells, and thus behave like distinguishable subsystems. The asymmetric shape of the potential is due to the difference in well depths, $D_L \neq D_R$, which will give us distinct single-particle energies in each well, and thus a non-degenerate energy level structure.

## 2.3 Time evolution

The time evolution of a quantum system is described by the Time-Dependent Schrödinger Equation (TDSE) (2.9). The TDSE shows the behaviour of a quantum system over time under the influence of the system Hamiltonian. While simple systems without time-dependence admit closed-form solutions, most physically realizable systems—especially those relevant for quantum control and information—exhibit time-dependent behaviour, and is generally not exactly solvable analytically. Treating such systems that cannot be solved analytically, requires numerical methods to approximate the evolution of the system. Understanding time evolution is crucial for modelling driven systems such as qubit under external control field, where energy transitions reveal non-trivial dynamics [48, 49], or simulating quantum gates in quantum computing [21, 50]. In this section, we outline the framework for quantum time evolution and introduce the time-evolution operator, which is at the heart of quantum dynamics, and the base for our numerical methods. We will also conceptualize the steps behind the numerical framework for solving the time-dependent Schrödinger equation, and also for discretizing the time evolution operator.

### 2.3.1 Time evolution operator

Simulating the dynamics of any quantum system is seen through the evolution of the quantum mechanical state representing the system at hand. The time evolution of a quantum state from time $t_0$ to $t$ is expressed by the linear unitary time-evolution operator $U(t, t_0)$, which is a solution to the time-dependent Schrödinger equation (2.9) [28, 34]. This operator should do

the following

$$|\Psi(t)\rangle = U(t, t_0) |\Psi(t_0)\rangle \tag{2.20}$$

and it must satisfy the following critera:

- **Unitarity:** $U(t, t_0)U^\dagger(t, t_0) = U^\dagger(t, t_0)U(t, t_0) = \mathbb{I}$, meaning it preserves the norm of the quantum mechanical state.

- **Composition property:** $U(t_2, t_0) = U(t_2, t_1)U(t_1, t_0)$, meaning the time-evolution operator is a composition of smaller time-evolution operators that are time-ordered $(t_2 > t_1 > t_0)$.

- **Continuity:** $\lim_{dt \to 0} U(t_0 + dt, t_0) = \mathbb{I}$, meaning the time-evolution operator is continuous, and reduces to identity when the time difference is zero.

All these critera can be satisfied by

$$U(t_0 + dt, t_0) = 1 - i\Omega(t_0)dt,$$

where $\Omega$ is a Hermitian operator, and $dt$ is the infinitesimal time difference. The third criteria is satisfied naturally as $dt$ goes to zero, while the first and second criteria are satisfied to first order

$$U^\dagger(t_0 + dt, t_0)U(t_0 + dt, t_0) = (1 + i\Omega(t_0)^\dagger)(1 - i\Omega(t_0)) = 1 + \mathcal{O}(dt^2) \cong 1$$

and

$$U(t_0 + 2dt, t_0) = 1 - i2\Omega(t_0)dt,$$
$$U(t_0 + 2dt, t_0 + dt)U(t_0 + dt, t_0) = 1 - 2i\Omega(t_0)dt + \mathcal{O}(dt^2),$$

if we have a small enough time-step $dt$, where we can safely ignore higher order terms. But how do we identify the operator $\Omega$? We identify from classical mechanics that the Hamiltonian operator is the propagator of the system [34]

$$\Omega = \frac{H}{\hbar}.$$

This means that the time-evolution operator can be expressed as

$$U = 1 - \frac{i}{\hbar}Hdt,$$

which we can see is the first order approximation of the exponential series

$$e^{\frac{-i}{\hbar}Ht} = 1 - \frac{i}{\hbar}Ht + \frac{1}{2!}\left(\frac{-i}{\hbar}Ht\right)^2 + ....$$

This is the full form of the time-evolution operator, normally called the time-propagator in the literature, and is given by

$$U(t, t_0) = \mathcal{T}\exp\left(\frac{-i}{\hbar}\int_{t_0}^{t} H(t')dt'\right), \tag{2.21}$$

where the integral must be time-ordered, and swapped with the Dyson series expansion should the Hamiltonian be time-dependent, and non-commutative at different times (see chapter 2.1.2 in [34] for more details on the time-ordering and Dyson series). For a time-independent Hamiltonian $H$, the time-evolution operator simplifies to

$$U(t, t_0) = e^{-\frac{i}{\hbar}H(t-t_0)},$$

allowing for analytical propagation of the system. In contrast, the time-dependent case (2.21) requires numerical treatment to solve the integral, as the exponential cannot be solved analytically.

### 2.3.2  Numerical time propagation

The time-propagator in (2.21) involves a time-ordered exponential, which generally cannot be solved analytically for a time-dependent Hamiltonian $H(t)$. Therefore, we must revert to numerical methods to approximate the integral. Choice of method is crucial, and it depends on desired accuracy, computational cost and stability. There are some other criteria to consider when developing, or choosing, a numerical method for time propagation. The method should preserve the norm of the wavefunction, and it should preserve the unitarity of the time-evolution operator.

To simulate time evolution of a quantum system numerically, we start by discretizing time $t$, into smaller intervals (time steps) $\Delta t$. Doing so allows us to approximate the time-evolution operator as a product of smaller step time-evolution operators, which can be solved iteratively (recall the composition property of the time-evolution operator). At each step then, the wavefunction is evolved by approximating the true time-evolution operator on the time interval $[t, t + \Delta t]$.

The simplest approximative method is the *Euler-Cromer* method, a first order method given by the Taylor expansion of the time-evolution operator

$$U(t + dt, t) = 1 - \frac{i}{\hbar} H(t) dt, \tag{2.22}$$

which leads to an explicit update of the wavefunction as

$$|\Psi(t + dt)\rangle = \left(1 - \frac{i}{\hbar} H(t) dt\right) |\Psi(t)\rangle.$$

This is a simple and fast, but inaccurate method. While this method is simple to implement and computationally inexpensive, it suffers from numerical instability and is not unitary nor norm-preserving. This means that the wavefunction will not be normalized after each time step, and the norm of the wavefunction may diverge over time, and we may obtain non-physical results should we want to evolve for longer timespans.

To improve the accuracy and stability of time propagation, higher-order and norm-preserving methods are generally preferred. One straightforward approach is to compute the matrix exponential of the Hamiltonian over each time step. Since this operator is unitary by construction, it ensures that the wavefunction remains normalized and the dynamics remain physically consistent. This method is particularly appealing for low-dimensional systems, where the Hamiltonian can efficiently be diagonalized, and the matrix exponential can be computed.

In practice, the matrix exponential is compututed on a discretized time interval by the expression

$$U(t + dt, t) = e^{-\frac{i}{\hbar} H(t) \Delta t}, \tag{2.23}$$

assuming that the Hamiltonian is approximatively constant over the time interval $\Delta t$.

This naturally is an exact update rule for time-independent Hamiltonians, but the accurateness of this method depends on the size of the time step $\Delta t$ and how the Hamiltonian varies over the time intervals. This does however introduce a new alley for approximations, where we may introduce various methods to approximate the Hamiltonian over the time interval, such as the average-time approximation, where we assume a better approximation is the average of the Hamiltonian at the start and end of the time interval, i.e

$$U(t + dt, t) = e^{-\frac{i}{\hbar} \frac{H(t) + H(t + dt)}{2} \Delta t}.$$

In this work, however, we shall mainly use (2.23) in its simplest form, as the Hamiltonian varies smoothly as we traverse through parameters space between our desired configurations.

Direct matrix exponentiation, however, quickly becomes intractable, as the system dimensionality increases, due to the computational burden of diagonalizing, or exponentiating, large matrices—commonly referred to as *the curse of dimensionality.* For this reason, it is often more efficient to apply numerical integration methods. A range of numerical integration methods can be applied to evolve the quantum wavefunction, each with its own advantages and disadvantages. These methods generally involve discretizing time and updating the wavefunction iteratively by approximating the time-evolution operator over small time intervals. While these methods are generally more computationally efficient than direct matrix exponentiation, they may not preserve unitarity exactly—however, many such methods can be made to do so approximatively. Most of these methods build upon Taylor expansions, as in the simple case of the Euler-Cromer method shown in (2.22), and more complex methods can be seen as higher-order approximations of the time-evolution operator.

Despite these limitations, numerical integration methods are widely used in quantum dynamics simulations, and they can provide accurate results for a wide range of systems. In this work, we will explore matrix exponentiation as a baseline method for time propagation, and we will compare it to other numerical integration methods. This will allow us to assess the accuracy and efficiency of other approaches for simulating quantum dynamics in our system.

Returning to our simple system (2.32), the time-evolution of a two-level system under a time-varying Hamiltonian is illustated in figure 2.5, where the population transfer between the two first energy eigenlevels $\phi_0 = |0\rangle$ and $\phi_1 = |1\rangle$, and avoided crossing reflect the dynamics driven by the time-evolution operator applied using direct matrix exponentiation. In figure 2.5, we highlight how some of the simplest methods diverge when evolving the simple system previously introduced in section 2.4.3.

## 2.4  Entanglement

The concept of entanglement is a fundamental feature of quantum mechanical systems, distinguishing interacting quantum systems from classical systems. Conceptually introduced by Einstein, Podolski, and Rosen in their 1935 EPR paper [51], the term *entanglement* was later formalized by Schrödinger in the same year [52]. Entanglement measures the correlations between two or more quantum mechanical subsystems. Any system with more than one degree of freedom exhibits such correlations between the "allowed states" in the system, and these correlations make the system non-separable. This means that, even if we have a complete description of the full system, we may not have a complete description of the correlated (entangled) subsystems. For a system of multiple particles, this implies that the state of each particle cannot be described independently of the states of the other particles, even if they are spatially separated by large distances. As Einstein famously expressed, there exists what he referred to as *"spooky action at a distance"*, a phenomenon that classical physics fails to explain or replicate.

### 2.4.1  Bell states

In our system, we will be working in a bipartite system. This means that we have two subsystems, $L$ and $R$ (left and right), which are connected by a coupling Hamiltonian. Our two subsystems are two electrically charged particles trapped in separate Morse potential wells, as seen in Figure (2.2), which then are coupled through the Coulomb interaction. To illustrate the
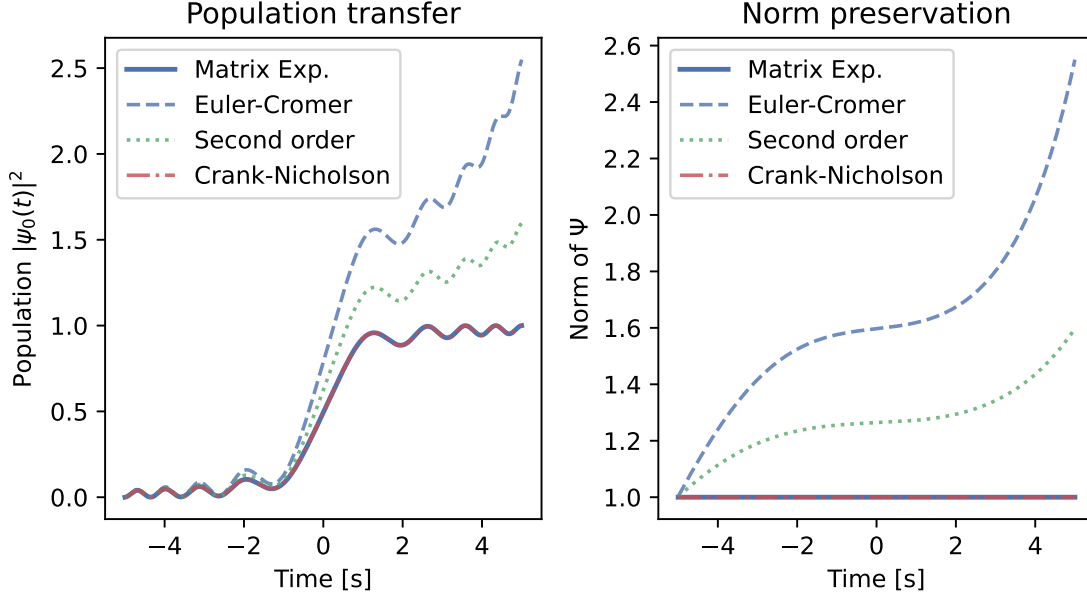
Figure 2.3: Time evolution of an initial state $\psi_0 = [1, 0]^T = |0\rangle$ in a two-level system under a time-varying Hamiltonian. Population transfer between $|0\rangle$ and $|1\rangle$ and wavefunction norm are shown, demonstrating how the simpler Euler-Cromer and second-order symmetric methods deviate from the exact solution, while Crank-Nicolson remains both norm-preserving and more accurate, and overlaps well with the exact direct matrix exponentiation.

concept of entanglement, we can consider a simple example of two distinguishable particles, $A$ and $B$, in a two-particle system, with two available states in each subsystem (ground state $|0\rangle$ and excited state $|1\rangle$). The state of the system can be expressed as a product state, where each particle is in a separate state:

$$|\Psi\rangle = |\psi_A\rangle \otimes |\psi_B\rangle,$$

where the available states are $|\psi_A\rangle = |0\rangle_A$ or $|1\rangle_A$ and $|\psi_B\rangle = |0\rangle_B$ or $|1\rangle_B$. The non-interacting system can be in any of the four possible product states:

$$|00\rangle = |0\rangle_A \otimes |0\rangle_B, \quad |01\rangle = |0\rangle_A \otimes |1\rangle_B,$$
$$|10\rangle = |1\rangle_A \otimes |0\rangle_B, \quad |11\rangle = |1\rangle_A \otimes |1\rangle_B$$

However, due to the influence of the coupling Hamiltonian, the system can evolve into an entangled state, in which the state of the particles are mutually dependent. An example of such entangled states are the Bell states [28, 34, 38], which are maximally entangled states of two qubits. These states are given by

$$|\Phi^+\rangle = \frac{1}{\sqrt{2}}(|00\rangle + |11\rangle), \tag{2.24}$$

$$|\Phi^-\rangle = \frac{1}{\sqrt{2}}(|00\rangle - |11\rangle), \tag{2.25}$$

$$|\Psi^+\rangle = \frac{1}{\sqrt{2}}(|01\rangle + |10\rangle), \tag{2.26}$$

$$|\Psi^-\rangle = \frac{1}{\sqrt{2}}(|01\rangle - |10\rangle). \tag{2.27}$$

In these states, measurements of the state of particle $A$ will immediately give information about

the state in which particle $B$ is in, and vice versa. For example, if we prepare our system in the Bell state $|\Phi^+\rangle$ and measure particle $A$ and find it in the state $|0\rangle$, we can immediately conclude that particle $B$ is also in the state $|0\rangle$. This is a fact, regardless of the physical separation of the two particles and was at the base for the EPR paradox [51]. This phenomenon, entanglement, is a direct consequence of the non-locality of quantum mechanics, and is a key resource for many quantum technologies, such as quantum computing, quantum cryptography, and quantum teleportation [3, 38, 53].

### 2.4.2  Quantifying, and measuring entanglement

While entanglement is conceptually well understood, quantifying it in physical systems—especially continuous and/or spatially extended systems like ours—requires precise mathematical tools. In our system of two charged particles confined in a double Morse well system (2.19), we aim to characterize the degree of entanglement between subsystems $L$ and $R$ that emerges due to the Coulomb coupling. To accomplish this, we shall turn to established entanglement measures such as the *von Neumann entropy*, which will allow us to quantify the extent to which subsystms $L$ and $R$ are entangled. To do so, we will also introduce the concept of the reduced density matrix and explore it's physical intepretation in the context of our bipartite system.

In classical physics, we always assume the system to exists in well-defined, definite states, with any uncertainty arising solely from a *lack of information or knowledge*. For example, a certain object will have a specific location in phase space, regardless of our knowledge of what this location is. This is what we call *pure states*. States that give a complete and unambigous description of the system. In quantum mechanics the situation is more nuanced. While there are systems that can be described by such pure states (and represented by a single state vector), many systems require a more general description, particularly large entangled systems of subsystems. In such cases, while the entire system as a whole is in a well-defined quantum state, the smaller subsystems may not have definite states of their own. Instead they can exists in a *mixed state*, which represents a statistical mixture—an ensamble—of different possible (pure) quantum states.

To summarize, a mixed state is a probabilistic combination of pure states, where the system is in one of the pure states with a certain probability. This is a direct consequence of the entanglement between the subsystems, as the correlations between them lead to uncertainty in the description of each subsystem. As opposed to the classical uncertainty, which arises from a lack of information, the uncertainty in quantum mechanics is a fundamental property of the system itself. This means that even if we have complete knowledge of the entire system, and it exists in a pure state, we may not be able to assign definite states to the subsystems meaning they are in mixed states [28, 29, 34].

Describing these mixtures thus require a more general formalism, and to do so we introduce the *density matrix formalism*. First introduced by John von Neumann in 1927 [54], the density matrix formalism allows for expressing quantum states by both pure and mixed states and it's an essential tool for understanding and quantifying entanglement, since it encapsulates information about how a subsystem becomes "uncertain" due to its correlations with the rest of the system. As a representation of the *density operator* (the two terms in practice are used interchangeably), the density matrix (operator) is given as

$$\rho = \sum_i w_i |\psi_i\rangle \langle\psi_i|, \tag{2.28}$$

where the probability weight $w_i$ is the probability of finding the system in the pure state $|\psi_i\rangle$. The density matrix is a positive semi-definite operator, and it has the following properties:

- $\text{Tr}(\rho) = 1$, meaning the trace of the density matrix is equal to 1, given that $\rho$ is a pure state. $\text{Tr}(\rho) < 1$ for mixed states.

- $\rho^\dagger = \rho$, meaning the density matrix is Hermitian.

- $\rho \geq 0$, meaning the density matrix is positive semi-definite.

Returning to our simple system of two distinguishable particles, we can express the density matrix of the system as

$$\rho_{AB} = \begin{pmatrix} \rho_{00,00} & \rho_{00,01} & \rho_{00,10} & \rho_{00,11} \\ \rho_{01,00} & \rho_{01,01} & \rho_{01,10} & \rho_{01,11} \\ \rho_{10,00} & \rho_{10,01} & \rho_{10,10} & \rho_{10,11} \\ \rho_{11,00} & \rho_{11,01} & \rho_{11,10} & \rho_{11,11} \end{pmatrix},$$

where the diagonal elements of the density matrix are the probability populations of the system being in the corresponding states $|00\rangle, |01\rangle, |10\rangle, |11\rangle$, while the off-diagonal elements are the coherences between said states—signatures of superposition states. Such superposition states differ from mixed states, as they are not statistical mixtures of pure states, but rather linear combinations of pure states. But how do we measure the entanglement in our system? To do so, we have mentioned the von Neumann entropy, which is a measure of the amount of information that is missing from the system. The von Neumann entropy is defined as [38]

$$S(\rho) = -\text{Tr}(\rho \ln \rho), \tag{2.29}$$

where $\rho$ is the density matrix of the system. But how do we relate this to entanglement when working with multiple entangled subsystems? We then need to find the *reduced density matrix*, which is a partial trace of the full density matrix over the other subsystem. Effectively, this means we are tracing out (or removing) the degrees of freedom in the other subsystems, which do not directly contribute to the entanglement. The reduced density matrix for subsystem $A$ is given as

$$\rho_A = \text{Tr}_B(\rho_{AB}) = \sum_i \langle i_B| \, \rho_{AB} \, |i_B\rangle, \tag{2.30}$$

where $|i_B\rangle$ are the basis states of subsystem $B$. The reduced density matrix for subsystem $B$ is given in a similar manner. The von Neumann entropy of the reduced density matrix is then given as

$$S(\rho_A) = -\text{Tr}(\rho_A \ln \rho_A), \tag{2.31}$$

and it can easily be shown that $S(\rho_A) = S(\rho_B)$, meaning the entanglement is symmetric between the two subsystems, which is to be expected.

Another useful aspect of the density matrix formalism is that it naturally ties together with measurements in quantum mechanics. Let us consider a quantum system expressed by a density matrix $\rho$ as in (2.28), and we want to measure an observable $O$ in the system. The expectation value of the observable is given as

$$\langle O \rangle = \sum_i w_i \langle \psi_i| \, O \, |\psi_i\rangle = \sum_i w_i \text{Tr}\big(|\psi_i\rangle \langle \psi_i| \, O\big) = \text{Tr}\big(\sum_i w_i |\psi_i\rangle \langle \psi_i| \, O\big) = \text{Tr}(\rho O),$$

and we see how powerful this notation is, we can quickly calculate expectation values of operators (observables) by a simple trace operation.

### 2.4.3  Avoided crossings

In our coupled, double well system (2.19), entanglement arises directly from the Coulomb inter-action between the two particles. This interaction (coupling) produces a phenomenon known as *avoided crossings* [50], regions in the parameters where energy levels approach one another but repel instead of crossing due to the coupling. In the uncoupled system, certain levels may be exactly degenerate, but the Coulomb coupling lifts these degeneracies and mixes the subsystem states. As a result, the full two-particle wavefunction can no longer be written as a simple product of single-particle states: the particles become entangled, and their energy levels shift in response to the interaction. We can then exploit these shifts to control and manipulate the joint quantum state [55].

To illustrate this, we can consider a simple example of a two level system, with two energy levels $E_1$ and $E_2$, which are degenerate in the uncoupled system, i.e $E_1 = E_2$. Introducing a coupling term $V$, the effective Hamiltonian of the system can be expressed as

$$H = \begin{pmatrix} E_1 & V \\ V & E_2 \end{pmatrix},$$

where $V$ is the coupling strength between the two levels. The eigenvalues of this Hamiltonian are given as

$$E_\pm = \frac{E_1 + E_2}{2} \pm \sqrt{\frac{(E_1 - E_2)^2}{4} + V^2},$$

and we can see that the energy levels are shifted due to the coupling, and they will never cross for $V \neq 0$.

Consider now a dynamical system, where there is some explicit time-dependence in the Hamiltonian, with a constant coupling strength $V$

$$H(t) = \begin{pmatrix} E(t) & V \\ V & -E(t) \end{pmatrix} = \begin{pmatrix} kt & V \\ V & -kt \end{pmatrix}, \tag{2.32}$$

where $E(t)$ is the time-dependent energy level of the system, with $k$ the sweeping parameter, that sweep the energy levels towards each other (they are equal at $t = 0$).

Simulating for a time starting from $t < 0$, where the energy levels are degenerate we will highlight the avoided crossing at $t = 0$, and we get what is called a *Landau-Zener transition* [48, 49]. As we can see, the Coulomb coupling between the two subsystems results in the energy levels repelling each other, while the non-interacting system would have crossed at $t = 0$ (as indicated by the dotted lines). But what happens with the wavefunctions prepared in the system? Initializing the system in the ground state $\psi_0 = |0\rangle$, we shall see that what happens at the avoided crossing depends heavily on both coupling strength $V$ and sweeping paramter $k$, through the Landau-Zener formula [48, 49]:

$$P_D = e^{-\frac{2\pi V^2}{\hbar k}}, \tag{2.33}$$

which governs the probability of the system to transitions diabatically (i.e remain in the same diabatic states). As visualized in the following plot (2.5), we can see how the sweeping parameter $k$ governs how the avoided crossing affect the prepared wavefunction, in one case we achive some minor level of mixing between the two basis states, while in the other case we achieve a full transition between the two states. In the case for a low $k = 1.0$, we near the adiabatic limit $P_D \approx 0$, where the system has time to continually adjust to the changing Hamiltonian, and
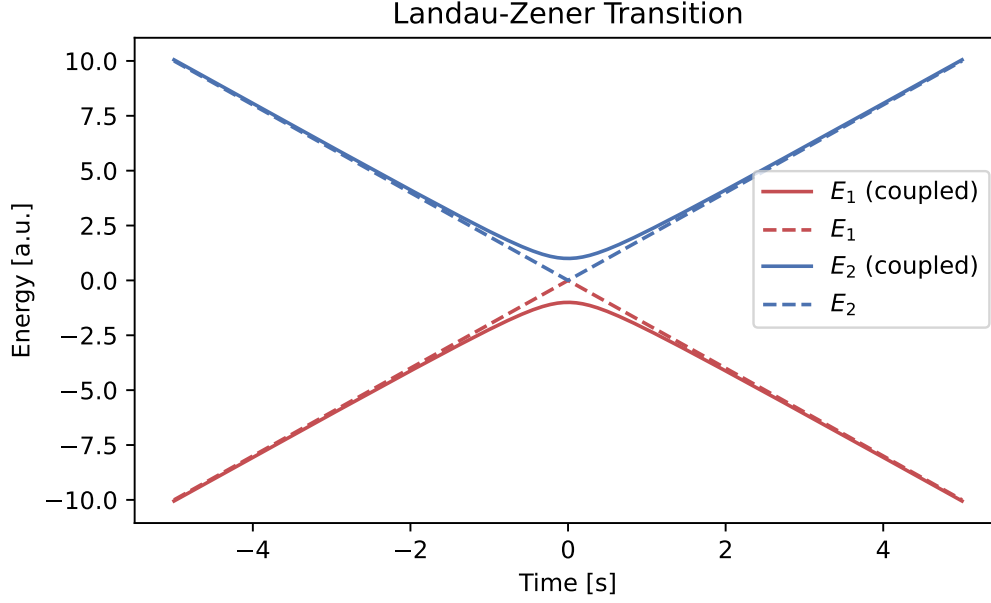
**Figure 2.4:** The avoided crossings in a two-level system as a function time $t$. The energy levels are shifted due to the coupling, and the energy levels do not cross, but rather "avoid" each other. The un-coupled system crosses at $t = 0$, as indicated by the dotted lines. The solid lines show the energy levels of the coupled system, which avoid crossing due to the coupling. Parameters for this novel visualization are $k = 1.0$ and $V = 2.0$.

the energy eigenstates 'swap' places as they evolve. In the case for a high $k = 10$, we are in the diabatic (non-adiabatic) limit $P_D \approx 1$, where the rapid change in the Hamiltonian does not allow the system to properly adjust, and the system eigenstates remain unchanged. As seen in the plot, we are not completely at the limits, but rather in a regime where the system ends up being partially mixed.

### 2.4.4  Rabi-oscillations in two-level systems

The evolution of coupled states in a two-level system follows coherent oscillations, known as *Rabi oscillations*[34, 38]. At resonance, the system oscillates between the two states $|0\rangle$ and $|1\rangle$ with a frequency determined by the coupling strength $J$. The transition probability between the two states are (in atomic units)

$$P_{0\to1}(t) = \frac{J^2}{\Delta^2 + J^2} \sin^2\left(\frac{1}{2}\sqrt{\Delta^2 + J^2}\,t\right),$$

where at resonance, $\Delta = 0$, the probability simplifies to

$$P_{0\to1}(t) = \sin^2\left(\frac{1}{2}Jt\right). \tag{2.34}$$

This gives us a simple way to compute the optimal gate duration for our qubit operations. For example, if we aim to implement the SWAP-gate, we want 100% population transfer between the two states, which means we want a transition probability of $P_{0\to1}(t) = 1$. This gives the optimal gate duration as

$$P_{0\to1}(t_{\mathrm{SWAP}}) = \sin^2\left(\frac{1}{2}Jt\right) = 1 \implies \frac{1}{2}Jt_{\mathrm{SWAP}} = \frac{\pi}{2}.$$
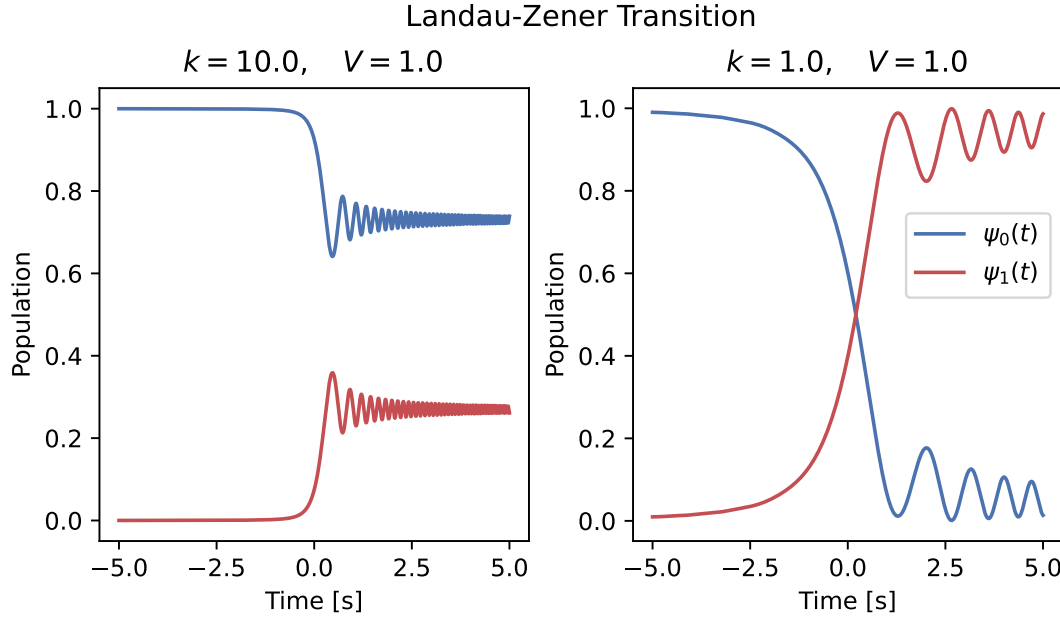
Figure 2.5: The Landau-Zener transition probability for different combinations of the coupling strength $V$ and the sweeping parameter $k$. The probability of the system to transition between the two energy levels is given by the Landau-Zener formula (2.33). We can see how the states are mixed for large $k = 10$ and transition fully for small $k = 1.0$.

This yields an optimal gate duration $t_{\text{SWAP}} = \pi/(2J)$, corresponding to the time required for a complete oscillation between the two states given a coupling strength $J$. To implement a $\sqrt{\text{SWAP}}$-gate, we instead require a 50% population transfer—a perfect mixture—which occurs when the transition probability is $P_{0 \to 1}(t) = 0.5$. Thus, the optimal gate duration becomes $t_{\sqrt{\text{SWAP}}} = t_{\text{SWAP}}/2$.

## 2.5 Quantum Logic and Control

Quantum computing is a rapidly developing field that promises to revolutionize information processing across disciplines such as cryptography, optimization, and materials science. While the subject has recently gained popular attention—even being mentioned in political discourse such as the 2024 U.S. presidential debates—the practical realization of quantum computers still faces several significant challenges [6]. At the top among these are the development of robust quantum hardware and the precise control of quantum systems, both of which fall under the umbrella of *quantum control* [56, 57].

In this work, we study a simple double-well Morse potential—a possible prototype for a quantum dot system—and investigate its time-evolution under the influence of Coulomb interaction. By tuning the parameters that define the potential, we perturb the system and observe how its dynamics evolve. This controlled perturbation forms the basis for implementing our quantum control protocols.

### 2.5.1 Quantum Control

Quantum control refers to the ability to manipulate the state of a quantum system in a precise and predictable way. It is a foundational requirement for quantum computing, where qubits (quantum bits) must be steered through specific trajectories in their Hilbert space to perform logic operations. Just as classical computation depends on switching transistors (bits) on

and off, quantum computation depends on the coherent manipulation of qubits via unitary transformations [38].

In this context, our double well Morse potential serves as a simple platform to demonstrate basic quantum control principles. By applying external fields or, as we shall see in this work, by tuning the parameters of the potential we can prepare our system for single-qubit operations, and induce transitions between different quantum states to perform two-qubit operations. This paves the way for considering Morse-type potentials candidates for robust and tunable qubit architectures—an avenue that, to our knowledge, has yet to be extensively explored in the literature.

Achieving reliable single-qubit operations in our system requires energy levels to be well-separated and non-degenerate. This is crucial so that one can apply external fields to induce transitions in a single qubit without inducing unwanted transitions in the other qubit. With the 4 tunable parameters in our double well Morse potential (2.19), we can achieve this by finding such a configuration that dinstinguishes the lowest lying single particle energy levels. The single particle energies are the Hartree energies of the two subsystems, found through the Hartree calculation 3.3. In our work, this will be referenced as the *measurement configuration*, or *configuration I*. It is in this configuration we want to make measurements of the system.

The second configuration, *configuration II*, aims to induce a transition between the two lowest lying single particle states. This configuration make the first excited states of both subsystems degenerate, while maintaining separation among higher levels. In this configuration, we expect the respective energy eigenstates to mix, and this will entangle our two qubits—which in turn, allows for two-qubit operations such as the SWAP gate, or the CNOT gate to mention a few [21, 58].

### 2.5.2 Quantum Logic

**Two-qubit operations**

In our model, we aim to emulate the SWAP- and $\sqrt{\text{SWAP}}$-gate by dynamically tuning the system into configuration II as previously described. The SWAP-gate is a two-qubit gate that swaps the states of two qubits [38]. It is defined as:

$$\text{SWAP} = \begin{pmatrix} 1 & 0 & 0 & 0 \\ 0 & 0 & 1 & 0 \\ 0 & 1 & 0 & 0 \\ 0 & 0 & 0 & 1 \end{pmatrix}, \tag{2.35}$$

and we have the square root of the SWAP gate, $\sqrt{\text{SWAP}}$, which maximally entangles the affected qubits, defined as:

$$\sqrt{\text{SWAP}} = \begin{pmatrix} 1 & 0 & 0 & 0 \\ 0 & \frac{1+i}{2} & \frac{1-i}{2} & 0 \\ 0 & \frac{1-i}{2} & \frac{1+i}{2} & 0 \\ 0 & 0 & 0 & 1 \end{pmatrix}. \tag{2.36}$$

The ordinary SWAP gate simply exchanges the states of two qubits without introducing any correlations, whereas its square-root variant $\sqrt{\text{SWAP}}$, split amplitude coherently between the two qubits, therefore turning a separable state input, $|01\rangle$ or $|10\rangle$, into a maximally entangled Bell state (2.27). These states are indispensable resources for many quantum algorithms and protocols, such as quantum teleportation, entanglement-based cryptography and many error-correcting codes [38, 53, 59].

In our work, configuration $C_{II}$ is designed to bring the first excited states of the two subsystmems into resonance, which allows for a coherent exchange of population between the qubit

states. This is due to the Coulomb interaction between the particles at this near-degenerate condition, akin to the avoided crossing shown in Section 2.4.3. Although we will not explicitly model the phase evolution needed to realize the exact SWAP or $\sqrt{\text{SWAP}}$ matrix, the behavior of our system mimics the essential ingredients of a SWAP-like gate: resonant exchange and entanglement generation.

By controlling the duration for which the system remains in the various configurations, and the time spent ramping between them, we can identify time windows where the system approximates the desired state-swapping behavior. This is analogous to how SWAP-gates are implemented in superconducting or trapped-ion systems through Hamiltonian engineering and pulse timing [60].

Thus, our model represents a novel first step towards demonstrating quantum logic operations using Morse-type double well potentials. The anharmonicity of the Morse potential enables isolation of low-lying states and avoids (unwanted) higher-level leakage, which is essential for the construction of robust, tunable qubit architectures [38].

**Single-qubit operations**

In addition to our two-qubit operations, high-fidelity quantum logic also requires precise single-qubit operations. In experimental practice, single-qubit gates are implemented by applying tailored external fields or voltage pulses that transiently shift one dot's energy levels [61]. In our Morse double-well model, configuration $C_I$ is engineered to have well-separated single-particle energies in the two subsystems. By driving at the resonance of one qubit, we can induce rotations in the state of that qubit without affecting the other.

In our study we focus mainly on *Z-rotations*, which are rotations around the *Z*-axis of the Bloch sphere[6], which crucially can correct unwanted dynamical phases that may accumulate during a two-qubit operation. A Z-rotation is defined as:

$$R_Z(\theta) = \begin{pmatrix} e^{-i\theta/2} & 0 \\ 0 & e^{i\theta/2} \end{pmatrix}, \tag{2.37}$$

where $\theta$ is the rotation angle. Written more compactly using the Pauli $Z$ operator, this can be expressed as $R_z(\theta) = \exp(-i\theta Z/2)$ [38]. The ultimate goal of these single-qubit operations is to increase the fidelity of our two-qubit operations, such as the SWAP gate, by correcting for any unwanted relative phases that misaligns the evolved statse with the target states. We note that $X$ and $Y$ rotations similarly can be performed, but our present work is limited to Z-rotations for phase correction.

### 2.5.3 Fidelity measures

To quantify, and assess the performance of our quantum control protocols we will measure the *fidelity* of the numerically generated two-qubit operation $U = \Psi_0^\dagger \Psi(t_f)$ against the ideal target operation $U_{target}$, where the target operation are the two-qubit gate matrices e.g (2.35). We introduce the following fidelity measures:

- **Average fidelity:** This is the standard measure of fidelity in quantum gate operations, sensitive to both population errors and incorrect phases. Following the derivations in Pedersen et al. [62], in a $d-$dimensional Hilbert space the average fidelity is defined as:

$$F_{avg}(U, U_{target}) = \frac{1}{d(d+1)}\left[\text{Tr}(MM^\dagger) + |\text{Tr}(M)|^2\right],$$

---

[6]If the reader is unfamiliar with the Bloch sphere representation, we recommend ch. 1.2 in [38]

where $M = U^\dagger_{target} U$. Assuming that $U$ is unitary, $M$ is therefore unitary, and $\text{Tr}(MM^\dagger) = d$, meaning the average fidelity is given by:

$$F_{avg}(U, U_{target}) = \frac{1}{d(d+1)} \left[ d + |\text{Tr}(U^\dagger_{target} U)|^2 \right].$$ (2.38)

- **Classical fidelity:** If we are only interested in the population transfer, and not the relative phases, then we may compare the two classical transition matrices $P$ and $P_{target}$, whose entries are $P_{ij} = |U_{ij}|^2$, through the Bhattacharyya overlap [63]:

$$F_j(P, P_{target}) = \sum_{i,j} \sqrt{P_{ij} P_{target,ij}},$$

and then average over all inputs $j$,

$$F_{classical}(U, U_{target}) = \frac{1}{d} \sum_j F_j(P, P_{target}).$$ (2.39)

Classical fidelity measures how well the gate operation reproduces the target population transfer, disregarding any phase information [38]. For deterministic gates—where each input state $|j\rangle$ is mapped to a unique output $|g(j)\rangle$—the target transition matrix probabilities satisfy $P_{target,ij} = \delta_{g(j),i}$, where $\delta_{ij}$ is the Kronecker delta. The Bhattacharyya overlap then simplifies to

$$F_j(P, P_{target}) = \sum_i \sqrt{P_{ij} \delta_{g(j),i}} = |U_{g(j),j}|.$$

and the classical fidelity reduces to the average of the absolute values of the transition amplitudes:

$$F_{classical}(U, U_{target}) = \frac{1}{d} \sum_j |U_{g(j),j}|^2 = \frac{1}{d} \sum_j P_{g(j),j}.$$ (2.40)

This is the average probability of correctly transferring the population from input state $|j\rangle$ to the target state $|g(j)\rangle$.

To summarize, the two fidelity measures introduced above play complementary roles in assessing the performance of our quantum control protocols. The average fidelity (2.38) captures the full coherent performance of the gate, including both population transfer and phase alignment, while the classical fidelity (2.39) isolates purely population transfer, disregarding any phase information. Initially, we will primarily focus on the classical fidelity to asseess if our two-qubit operations achieve the desired population transfer. Once the population transfer is satisfactory, we will calculate the average fidelity to assess the overall performance of our two-qubit operations, including any phase errors. This will then be usde to find suitable single-qubit operations that can correct for any unwanted phases that may have accumulated during the two-qubit operation, resulting in a better average fidelity measure, and a more successful two-qubit operation. In the method section, we will outline how we compute these fidelity measures numerically from the time-evolved system, and how this guides the construction of our single-qubit $R_Z$ corrections to yield a high-fidelity two-qubit gate.

# Chapter 3

# Methods & Implementation

This chapter details the methodologies and implementation strategies that underpin both intermediate analyses and the final results of our thesis. Structured chronologically, our approach aims to guide the reader to an understanding of the progression and refinement of methods throughout the project.

> *"Science is what we understand well enough to explain to a computer. Art is everything else we do."*
>
> — Donald E. Knuth

Initially, we describe the foundational setup and system initialization, outlining the Morse double-well potential implementation and its essential components and conditions required for simulation. Next, we present the methods used for the preliminary background analysis of the Morse double-well system, which provide critical insights and understandings necessary for the subsequent time-dependent simulations. Following this, the Hartree approximation method is introduced, detailing the numerical implementation and its significance in substantially reducing the computational complexity of the system.

Central to our project's objective, we then delve into the sophisticated numerical techniques used for simulating time-evolution dynamics. Particular attention is given to ensuring the accuracy, stability and robustness of thse numerical schemes. Subsequently, our attention shifts toward post-processing techniques, which include the calculation of physical observables, such as state populations and entanglement measures, and phase-correction techniques to enhance the fidelity of our quantum gates.

Finally, we conclude with a comprehensive overview of the workflow, clearly illustrating how individual methodological components interconnect. This summary serves as a roadmap, ensuring the reader appreciates how each element integrates seamlessly to achieve our research goals.

All numerical implementations were done in Python, with complex computational algorithms presented clearly with code snippets and pseudo-code. The complete codebase is available on GitHub at: `https://github.com/Jonnyigeh/Thesis`.

## 3.1  System initialization and setup

In this section, we outline the steps taken to initialize the system Hamiltonian on the Sinc-DVR basis grid.

To numerically implement the Morse potential as presented in Section 2.2.4, and obtain separate single-particle hamiltonians for each subsystem, we need to 'split' the potential into two parts, one for each subsystem. This is easily done by dividing the spatial grid, $x \in [-L, L]$, on which the double-well potential is defined on, into two halves, left $x_L \in [-L, 0]$ and right $x_R \in [0, L]$. and computing the kinetic and potential integrals for each subsystem separately, using the analytical expressions in (2.7) and (2.19) respectively. This gives the single-particle Hamiltonians

$$H_L = T + V_L$$
$$H_R = T + V_R,$$

with $T$ being the kinetic energy operator, and $V_L$ and $V_R$ being the potential energy operators for the left and right subsystems respectively.

Similarly, to compute the interaction integrals, we want to compute the Coulomb interaction between the two subsystems. This is done by computing the shielded Coulomb interaction for each grid point in subsystem $L$ with each grid point in subsystem $R$. The following snippet illustrates how this is done in practice:

```python
N_L = ...
N_R = ...
alpha = 1.0
a = 0.1
coulomb = np.zeros((N_L, N_R), dtype=np.complex128)
for i in range(N_L):
    for j in range(N_R):
        x_L = x[i]
        x_R = x[j]
        r = np.sqrt((x_L - x_R)**2 + a**2)
        coulomb[i, j] = alpha / r
```

This code computes the shielded Coulomb interaction between each grid point in the left subsystem and each grid point in the right subsystem, resulting in an $N_L \times N_R$ interaction matrix. The parameter $a$ is the shielding length that ensures the interaction is well-defined even when particles are very close together, avoiding singularities.

This interaction matrix is then added to the single-particle Hamiltonians, constructing the full two-particle Hamiltonian matrix as

$$H = H_L \otimes \mathbb{I}_R + \mathbb{I}_L \otimes H_R + V_{LR}, \tag{3.1}$$

where $H_L$ and $H_R$ are the single-particle Hamiltonians for the left and right subsystems, respectively, and $V_{LR}$ is the interaction matrix between the two subsystems. This Hamiltonian is built upon our assumption that the two subsystems are separable, meaning that the particles are strictly localized in their respective wells.

With this in hand, we can construct the reduced Hartree basis through the Hartree method (Section 3.3).

## 3.2  General study of the system

In this secton we will outline the methods used to study our system in general. These studies will be used to set up our system in such a way that our desired configurations are achieved,

whilst also ensuring that the system is stable, well-defined and physically meaningful. To this end there are a few things we need to consider:

- At what well separation is our approximation of the two particles being distinguishable valid (to a certain degree)?

- What parameters do we need to set in order to achieve our desired configurations I and II?

- Will our choice of basis functions be sufficient to descibe our system?

- How do we ensure that our system is stable, and well-defined—while also physically meaningful?

### 3.2.1  Assessing validity of product state approximation

One of the core features of our qubit design is that each electron is tightly confined in its own well of the Morse double-well potential, so that their spatial wavefunctions have minimal overlap. Strictly speaking, electrons are indistinguishable fermions and their total two-particle wavefunction must be anti-symmetric under particle exchange to adhere to the Pauli exclusion principle [28, 29]. However, when the spatial overlap between localized orbitals $\langle \phi_L | \phi_R \rangle$ becomes vanishingly small (for large separations $d$ and/or very deep, narrow wells), the exchange integral tends to zero. In that limit, the anti-symmetric wavefunction

$$\Psi_A(x_1, x_2) = \frac{1}{\sqrt{2}} \left[ \phi_L(x_1)\phi_R(x_2) - \phi_L(x_2)\phi_R(x_1) \right],$$

reduces to a simple product state $\phi_L(x_1)\phi_R(x_2)$, and the electrons behave as effectively *distinguishable* particles.

In this analysis we aim to quantify the degree of distinguishability between the two particles in our system, and determine the conditions under which we can treat them as distinguishable and identify the inter-well separation limit where our product state approach is valid. Concretely, for each inter-well separation $d$, we compute

- **The product state energy:** We form the separable product state wavefunction

$$\Psi(x_1, x_2) = \phi_L(x_1)\phi_R(x_2),$$

and assemble the Hamiltonian matrix for this product state system $H = H_L \otimes I + I \otimes H_R + V_{LR}$, where $H_L$ and $H_R$ are the single-particle Hamiltonians for the left and right wells, respectively, and $V_{LR}$ is the inter-well coupling potential. We diagonalize this Hamiltonian to obtain the product state energy $E_{prod}(d)$.

- **The anti-symmetric (CI) energy:** We construct the anti-symmetric wavefunction $\Psi_A$ as a sum of product state and solve the full two-body Configuration Interaction (Section 3.4) to find $E_{anti}(d)$.

We then examine the energy difference between the two states to quantify the exchange interaction

$$\Delta E(d) = E_{anti}(d) - E_{prod}(d).$$

which should tend to zero as the inter-well separation $d$ increases, indicating that the exchange interaction becomes negligible and the particles can be treated as distinguishable. The distance $d^*$ at which $\Delta E(d^*) \approx 0$ defines the regime where the product-state treatment becomes fully justified.

### 3.2.2   Parameter optimization

As our goal is to realize single-qubit gates and the two-qubit SWAP-gate, we need to find suitable configurations of our potential where we achieve the desired degeneracy in energy levels and also our desired level of entanglement between the two particles. As we have discussed in earlier sections the two configurations we are looking for are:

- **Config I**: The measurement configuration, where all energy levels are distinct and there are minimal correlations between the two subsystems (particles). This corresponds to keeping all Von Neumann entropies in our system as close to zero as possible. With this, we know that our two-body energy eigenstates will have a product state structure, and maximal overlap with the Hartree product states $|00\rangle , |01\rangle , |10\rangle , |11\rangle$.

- **Config II**: The entangled configuration, where we have a degeneracy in the energy levels of our system. This degeneracy will give rise to an avoided crossings in the energy spectrum for the first and second energy eigenstates. In this configuration, the 1st and 2nd energy eigenstates are maximally entangled, while the other energy eigenstates are kept as pure as possible (product states). This corresponds to an entropy equal to 1 for $|\phi_1\rangle$ and $|\phi_2\rangle$, and 0 for $|\phi_0\rangle$ and $|\phi_4\rangle$.

As an initial search, we make a grid search over the potential parameters, mostly to map out the landscape of the parameterspace and find regions where we expect to find the desired configurations. Our grid search will be over the parameters presented in table 3.1, with the

| Parameter | Range | Description |
|---|---|---|
| $D_l, D_r$ | $[D_{\min}, D_{\max}]$ | The depth of the potential well |
| $k_l, k_r$ | $[k_{\min}, k_{\max}]$ | The width of the potential well |
| $d$ | $[d_{\min}, d_{\max}]$ | The distance between the two potential wells |

Table 3.1: The parameters we will search over in our grid search

constraint that $2D/\sqrt{k} < l$ where $l$ are the number of basis functions allocated to each well, as we have discussed earlier. This is to ensure that the basis functions are within the potential well, and that we do not have any basis functions that are cut off by the potential. This then becomes a *constrained optimization problem*. To perform our optimization we will use the `scipy.optimize` package, and the `minimize` function. We will use the `COBYQA` method, which is a derivative-free optimization method that is well suited for constrained optimization problems. This method is built on the concept of *sequential quadratic programming*, that solves constrained, non-linear problems. For more details on the method, see [64]. The optimization procedure is outlined in 1:

#### Objective function

An objective function is constructed for the optimizer, which is the object to be minimized by our optimization algorithm. We will have two separate objective functions, one for each configuration we are looking for. Across both configurations, we want to minimize the $\zeta$-parameter, which directly controls the stability of time-evolution through the Hamiltonian matrix. The parameters is defined as

$$\zeta = E_4 - E_1 - E_2 + E_0, \tag{3.2}$$

and we can identify this as the *accumulated phase* of the rotated time-evolution operator $U = e^{-iHt}$, expressed in terms of the energy eigenstates, $U = \sum_i^4 e^{-iE_i t} |\phi_i\rangle \langle\phi_i|$. We see

---

**Algorithm 1** Parameter optimization procedure: High-level overview

---

**Input:** Parameter ranges $\mathcal{R}$, $\epsilon_{\text{coarse}}$, $\epsilon_{\text{fine}}$     **Output:** Final refined parameter sets

**1. Initialization**

Generate a collection of random parameter configurations within $\mathcal{R}$.

**2. Coarse Optimization**

For each configuration in the collection:

- Run the optimizer with convergence tolerance $\epsilon_{\text{coarse}}$.

- If the optimized result meets the desired criteria, retain it as a candidate.

**3. Fine Optimization**

For each candidate parameter set:

- Re-run the optimizer with tighter tolerance $\epsilon_{\text{fine}}$.

- Add the refined output to the final results.

**4. Return** the final set of optimized parameters.

---

that written in matrix form in the logical state basis $\{|ij\rangle\}$, this propagator is (where $|11\rangle$ is the 4th energy eigenstate)

$$
U = \begin{pmatrix}
e^{-iE_{00}t} & 0 & 0 & 0 \\
0 & e^{-iE_{01}t} & 0 & 0 \\
0 & 0 & e^{-iE_{10}t} & 0 \\
0 & 0 & 0 & e^{-iE_{11}t}
\end{pmatrix}.
$$

The energy eigenstates themselves are not unique, because we are free to apply arbitrary single-qubit phase rotations to shift their individual phases without affecting populations (as they are cancelled in any innerproduct). By performing local $Z$-rotations (2.37) on qubit A and B, we can absorb the phases on the first three states ($|00\rangle$, $|10\rangle$, $|01\rangle$) into $|11\rangle$ [38]. In other words, invoking a single global phase, we use single-qubit rotations on each qubit to collect the relative phases onto $|11\rangle$. After the rotations, the condition

$$
E_{11} = E_{10} + E_{01} - E_{00}
$$

means that the excitation energy from the 0th state $|00\rangle \rightarrow |11\rangle$ equals the sum of excitations $|00\rangle \rightarrow |10\rangle$ and $|00\rangle \rightarrow |01\rangle$, which aids in ensuring phase stability in our SWAP-like two-qubit gate operation [65].

Configuration I, as we have mentioned, should have all energy levels distinct. This introduces penalties in our objective function corresponding to the overlap between energy eigenvalues and we want the Von Neumann entropies to be as close to zero as possible. We realise this in the following way

```
target_entropy = np.zeros(4)
detuning_penalty = -min(0.5, np.abs(e_L - e_R))
entropy_penalty = np.linalg.norm(entropy - target_entropy)
ZZ_penalty = np.abs(E_4 - E_1 - E_2 + E_0)
```

where `e_L` and `e_R` are the energy levels of the left and right well, and `entropy` is the Von Neumann entropy of the subsystems. The `detuning_penalty` is a penalty that is introduced to ensure that the energy levels are distinct, and the `entropy_penalty` is a penalty that ensures that the entropy is as close to zero as possible. The objective function is then the sum of these

two penalties. Furthermore, we would like the two configurations parameters to be close in parameter space, so that our evolution between the two configurations is smoooth. We introduce a penalty for this as well, similar to the `entropy_penalty`. We also want to penalize off-diagonal coupling terms in the Hamiltonian matrix, as these will introduce unwanted couplings between the subsystems in our measurement configuration. This is done by introducing a `off_diagonal_penalty` that is the scaled sum of the absolute values of the off-diagonal elements in the Hamiltonian matrix.

In configuration II we have a similar detuning penalty, but in this configuration we do want degeneracy in the 1st Hartree energy level in each well, as well as having an entropy penalty, but with a different target vector. We also here want to penalize certain off-diagonal coupling terms in the Hamiltonian matrix that induces unwanted transitions during evolution, and reward the correct coupling between the subsystems that induce entanglement between the first two excited energy eigenstates. This coupling is closely related to the energy difference between said energy states, so we want to minimize $\Delta E_{12}/J_{12}$, where $J_{12}$ is the coupling strength between the first two energy eigenstates through the `J_deltaE_penalty`. The objective function is then again the sum of these penalties.

```python
target_entropy = np.array([0, 1, 1, 0])
detuning_penalty = np.abs(e_L - e_R)
entropy_penalty = np.linalg.norm(entropy - target_entropy)
ZZ_penalty = np.abs(E_4 - E_1 - E_2 + E_0)
J_12 = np.abs(H[1, 2])
deltaE_12 = np.abs(E_2 - E_1)
J_deltaE_penalty = - np.abs(J_12 / deltaE_12 + 1e-12)
```

### 3.2.3  Sinc-Discrete Variable Representation

We implement the Sinc Discrete Variable Representation (Sinc-DVR) basis in Python to discretize our one-dimensional quantum problem on a uniform grid. The delta-like basis functions of the Sinc-DVR allow an analytic representation of the kinetic operator and simplify multi-dimensional integrals (Section 2.1.5), making this method efficient and accurate for smooth, localized potentials. However, its effectiveness relies on the accurate representation of the physically relevant states of the specific system under study.

As a test case, we consider a single particle trapped in a Morse potential (2.16), which models an anharmonic bounded oscillator potential with well-known analytical and numerical solutions. As a brief reminder, the Morse potential is given by

$$V(x) = D\left(1 - e^{-a(x-x_0)}\right)^2,$$

where $D$ is the depth of the potential well, $a$ is the width of the potential, and $x_0$ is the equilibrium position of the potential. This potential is well-suited for benchmarking, as it is smooth and localised, and also well represents the more complex double-well potential we are later interested in. The exact eigenstates and eigenvalues are computed analytically, using the expressions in (2.17) and (2.18), which are derived from the Schrödinger equation for the Morse potential.

The procedure to compute and compare the energy spectrum and eigenstates of the Morse potential using the Sinc-DVR basis and the exact energy eigenstates is as follows:

- Set up the potential using a set of parameters $D$, $a$, and $x_0$.

- Construct the Sinc-DVR basis functions $\phi_n(x)$ over a uniform grid of points $x_i$.

- Construct the Hamiltonian matrix $H$ using analytical expressions for Sinc-DVR.

- Diagonalize the Hamiltonian matrix to obtain the energy eigenvalues and eigenstates.

- Compute overlaps $S_{nm}$ and energy deviations $\Delta E_n$ between the Sinc-DVR and exact eigenstates.

This procedure allows us to validate the Sinc-DVR basis by comparing the computed energy eigenvalues and eigenstates with the exact solutions of the Morse potential. We aim for high accuracy in the lowest lying energy eigenstates and energy levels, as these are the most relevant for our quantum control protocols. In the following sections, we will outline the numerical implementation of these steps.

**Energy spectrum**

In the following code snippet, we highlight some of the key steps in the construction of the quantum mechanical system and the diagonalization of the Hamiltonian matrix, which is used to obtain the energy eigenstates and eigenvalues of the system.

```
N = 200
x = np.linspace(-1, 2, N)
dx = x[1] - x[0]
def morse_function(x, n, lmbda, x_e, c):
    def normalization(n, lmbda, c):
        return (
            (scipy.special.factorial(n) * (2 * lmbda - 2 * n - 1) * c /
             scipy.special.gamma(2 * lmbda - n))**0.5 # Gamma(n+1) = factorial(n)
        )
    z = 2 * lmbda * np.exp(-c * (x - x_e))
    return (
            normalization(n, lmbda, c) *
             z**(lmbda - n - 0.5) * np.exp(-z / 2) *
                scipy.special.genlaguerre(n, 2 * lmbda - 2 * n - 1)(z)
    )
def compute_eigenenergies(c, D, l):
    hnu = 2 * c * np.sqrt(D / 2)
    E_n = np.zeros(l)
    for n in range(l):
        E_n[n] = hnu * (n + 0.5) - (c * hnu * (n + 0.5)**2) / np.sqrt(8 * D)

    return E_n

def morse_potential(x, D, a, x0):
    return D * (1 - np.exp(-a * (x - x0)))**2 - D

V_matrix = np.diag(morse_potential(x, D, a, x0))
T_dvr = np.zeros((N, N))
for i in range(N):
    for j in range(N):
        if i == j:
            T_dvr[i, j] = np.pi**2 / (6 * dx**2)
        else:
            T_dvr[i, j] = ((-1)**(i - j)) / (dx**2 * (i - j)**2)

H_dvr = T_dvr + V_matrix
# Diagonalize the Hamiltonian
E_dvr, psi_dvr = np.linalg.eigh(H_dvr)
E_exact = compute_eigenenergies(c, D, N)
psi_exact = morse_function(x, np.arange(N), lmbda, 0, c)
```

To assess the performance of the Sinc-DVRs ability to reproduce the energy eigenvalues, we compute the absolute deviance

$$\Delta E_n = |E_n^{\text{DVR}} - E_n^{\text{exact}}|,$$

where $E_n^{\text{DVR}}$ is the $n$th energy eigenvalue computed using the Sinc-DVR basis, and $E_n^{\text{exact}}$ is the exact energy eigenvalue of the system. The goal is to show that the Sinc-DVR basis can reproduce the relevant energy levels of the system with high accuracy.

**Energy eigenstates**

To compare the energy eigenstates of the two basis sets, we compute the overlap between the Sinc-DVR basis functions and the exact energy eigenstates of the system. The overlap is defined as

$$S_{nm} = \langle \phi_n | \psi_m \rangle = \int_{-\infty}^{\infty} \phi_n(x)\psi_m(x)dx,$$

where $\phi_n(x)$ is the Sinc-DVR basis function and $\psi_m(x)$ is the exact energy eigenstate of the system. The overlap can be computed numerically using a direct Riemann sum,

$$\int_a^b f(x)dx \approx \sum_{i=0}^{N-1} f(x_i)\Delta x,$$

as shown in the following code snippet, building on the previous code snippet 3.2.3:

```python
E_dvr, psi_dvr = np.linalg.eigh(H_dvr)
E_exact, psi_exact = np.linalg.eigh(H_exact)
S = np.zeros((n_levels, n_levels))
for i in range(n_levels):
    for j in range(n_levels):
        # Calculate the overlap integral
        overlap = np.sum(psi_dvr[:, i].conj() * psi_exact[:, j])
        S[i, j] = np.abs(overlap)
```

where `n_levels` is the number of energy levels we are interested in. The reader might notice the lack of $\Delta x$ in the overlap integral, this is due to how `numpy` produces normalized basis sets from diagonalization in the `eigh` function, so their (discrete) normalization is already accounted for. The overlap matrix $S$ is then a $n_{\text{levels}} \times n_{\text{levels}}$ matrix, where each element $S_{nm}$ represents the overlap between the $n$th Sinc-DVR basis function and the $m$th exact energy eigenstate of the system.

## 3.3 Hartree method

As presented in section 2.2.2, the Hartree method is a self-consistent field method (SCF), where we solve the coupled eigenvalue equations for the two subsystems (particles) iteratively. The method is very similar to the Hartree-Fock method, and the main difference is that we do not include an exchange term and the wavefunction itself a single hartree product state. The general method is presented in 2:

We make an initial ansatz for the single-particle orbitals by constructing the Hartree matrix as in (2.15), and diagonalize the matrix to obtain the new set of orbitals, one set for each subsystem. The initial Hartree matrix is thus constructed as

$$f_{\alpha\beta}^{M(0)} = h_{\alpha\beta}^M,$$

---

**Algorithm 2** Self-Consistent Hartree Procedure

---

**1. Initial guess:**
Construct a starting set of single-particle orbitals $\{\chi_i\}$.

**2. Iterate to self-consistency:**
a. Build the Hartree matrix $f$ from the one- and two-body integrals weighted by the current $\{\chi_i\}$.
b. Diagonalize $f$ to obtain updated orbitals $\{\phi_i\}$ and orbital energies $\{\epsilon_i\}$.
c. Compute the total Hartree energy $E$.
d. If $|E - E_{\text{previous}}| < \delta E$, stop; otherwise set $\chi_i \leftarrow \phi_i$ and repeat.

**3. Final evaluation:**
Using the converged orbitals, calculate the final total energy, and any other desired observables.

---

where $M$ is the subsystem index, and $\alpha, \beta$ are the basis functions. This yields our initial set of orbitals, but does not include any interaction between the two subsystems. In the next iterations, we construct new Hartree matrices, and diagonalize them to obtain new orbitals. The new Hartree matrix for the ith iteration is constructed as

$$f_{\alpha\beta}^{M(i)} = h_{\alpha\beta}^M + \sum_i^N u_{\alpha\gamma\beta\delta}^M \rho_{\gamma\delta}^M,$$

where the density matrix $\rho_{\gamma\delta}^M$ is constructed from the previous set of orbitals, and used to calculate the interaction term *for subsystem $M$ specifically*. This differs from Hartree-Fock where the interaction term is calculated from the total density matrix ($\rho^A \otimes \rho^B$). In the following code snippet the density matrix is not used directly, but an equivalent Einstein summation is performed, following the equations (2.13).

```python
def construct_hartree_matrices(self, h_l, h_r, u_lr, c_l, c_r):
    return (
        h_l + np.einsum('j, ijkl, l -> ik', c_r[:,0].conj(), u_lr, c_r[:,0]),
        h_r + np.einsum('i, ijkl, k -> jl', c_l[:,0].conj(), u_lr, c_l[:,0]),
    )
def diagonalize_hartree_matrices(self, f_l, f_r):
    eps_l, c_l = scipy.linalg.eigh(f_l, subset_by_index=[0, self.num_basis_l - 1])
    eps_r, c_r = scipy.linalg.eigh(f_r, subset_by_index=[0, self.num_basis_r - 1])
    return eps_l, c_l, eps_r, c_r
```

With these two functions we set up the SCF as outlined in Algorithm 2. We use the `scipy.linalg`[66] package and its hermitian eigensolver `eigh` to diagonalize the Hartree matrices, selecting the subset of functions we wish to extract, corresponding to the number of available basis functions in each subsystem. In our implementation we terminate the SCF procedure when the single-particle Hartree energies converges within a threshold of $\Delta E < 10^{-10}$ a.u., or we reach a maximum number of iterations, which we set to 1000. For most Morse double-well configurations, the SCF procedure converges within a few 10-20 iterations starting from the non-interacting eigenstates. We rarely experience divergence, but if it should occur, we would recommend starting from a different initial guess to accelerate convergence.

## 3.4  Configuration Interaction

Building on the Hartree method, our CI implementation projects the full two-particle product state Hamiltonian into a smaller subspace of anti-symmetrized basis states. Recall from Section 2.2.3, that in practice we do the following:

- Truncate to the lowest $N$ ($N < M$) orbitals in each well.

- Form all unordered pairs of these orbitals, i.e. $\{\phi_i, \phi_j\}$ where $i \neq j$.

- Build the CI Hamiltonian by calculating the matrix elements of the two-particle Hamiltonian in this reduced basis.

- Diagonalize the CI Hamiltonian to obtain the energy eigenstates and eigenvalues.

In practice, to perform the CI procedure, we build a linear map $P$ that projects any vector in the $M$-dimensional product-state Hilbert space down onto our anti-symmetric subspace of dimension $\binom{N}{2}$. Concretely, this means that we enumerate all possible unordered pairs of orbitals with $0 \leq i < j < N$, and for each pair construct the anti-symmetric basis state

$$|\phi_i, \phi_j\rangle = \frac{1}{\sqrt{2}}(|\phi_i\rangle \otimes |\phi_j\rangle - |\phi_j\rangle \otimes |\phi_i\rangle).$$

This flattened representation of the anti-symmetric basis state will build the columns of the projection matrix $P$, which ensures $P^\dagger P = \mathbb{I}$, where $\mathbb{I}$ is the identity matrix.

Once $P$ is constructed, we can project the full two-particle Hamiltonian $H$ onto the anti-symmetric subspace by

$$H_{\mathrm{CI}} = P^\dagger H_{\mathrm{prod}} P.$$

Because $H_{\mathrm{prod}}$ contains all the one- and two-body terms of the product basis, the projected Hamiltonian $H_{\mathrm{CI}}$ will contain all the relevant interactions between the two particles in the anti-symmetric subspace. This gives us a reduced Hamiltonian that can be diagonalized to obtain the energy eigenstates and eigenvalues of the system. The CI method thus allows us to efficiently explore the low-energy spectrum of the two-particle system while maintaining the anti-symmetry required by quantum mechanics.

The following code snippet illustrates how we construct the projection matrix $P$ and the CI Hamiltonian $H_{\mathrm{CI}}$ in practice:

```python
h_l = ... # One-body Hamiltonian left well
h_r = ... # One-body Hamiltonian right well
u_lr = ... # Two-body coulomb matrix elements
H = np.kron(h_l, np.eye(M)) + np.kron(np.eye(M), h_r) + u_lr
M = h_l.shape[0]                # number of one-particle functions
pairs = [(i, j) for i in range(M) for j in range(i)]

P = np.zeros((M*M, len(pairs)), dtype=complex)
for idx, (i, j) in enumerate(pairs):
    e_i = np.zeros(M); e_i[i] = 1
    e_j = np.zeros(M); e_j[j] = 1
    psi_ij = np.kron(e_i, e_j)
    psi_ji = np.kron(e_j, e_i)
    P[:, idx] = (psi_ij - psi_ji) / np.sqrt(2)
H_CI = P.conj().T @ H @ P   # Projected CI Hamiltonian
eps_CI, C_CI = np.linalg.eigh(H_CI)   # Diagonalize CI Hamiltonian
```

This code constructs the projection matrix $P$ by iterating over all pairs of orbitals, creating the anti-symmetric basis states, and then projecting the full two-particle Hamiltonian onto this subspace. The resulting CI Hamiltonian $H_{\mathrm{CI}}$ can then be diagonalized to obtain the energy eigenstates and eigenvalues of the system in the anti-symmetric subspace.

## 3.5  Time-evolution

In this section, we describe the numerical implementation of the time-dependent Schrödinger equation (TDSE) for evolving quantum states under a (possibly time-dependent) Hamiltonian. Our primary goal is to simulate the time evolution of a quantum wavefunction from a known initial state, using various numerical methods to approximate both the time-evolution operator and the propagation of the wavefunction itself.

We begin by discussing how to discretize time for numerical propagation, and our choice made regarding time-discretization in the work. We then introduce different strategies for approximating the time-evolution operator and solving the TDSE. Several integration schemes are examined, and we compare their accuracy, stability, and efficiency. We validate our implementation using the well-known Landau-Zener model before applying the methods to the more complex double-well Morse potential system, before motivating our choice methods backed by these simple tests.

### 3.5.1  Time discretization

The foundation of any numerical time-evolution scheme lies in the discretization of the time variable. Typically, this is done by introducing a time step $\Delta t$, and defining a grid of time points $t_n = n\Delta t$ where $n$ is an integer. In general, there are two ways to do this:

- **Fixed time step:** This is the most common approach, where we define a fixed time step $\Delta t$ and evolve the system in small steps.

- **Adaptive time step:** This approach allows for a variable time step, where the time step is adjusted based on the dynamics of the system. This can be useful for systems with rapidly changing dynamics, where a fixed time step may not be sufficient to capture the dynamics accurately.

In this work we will be primarily employing fixed time steps, as the system we are studying is not expected to exhibit rapidly changing dynamics, due to us being in control of how we vary the potential parameters and thus perturb the system. The choice of time step is crucial for the accuracy and stability of most numerical schemes, and a poorly chosen time step can lead to divergence—as most methods error scales with $\Delta t$. In practice, we choose a time step that is small enough to ensure convergence of the results, but large enough to keep the computational cost manageable.

All of our time-evolution simulations on the Morse double-well potential use a fixed time-step of $\Delta t = 0.1$ a.u. This choice represents a compromise between accuracy (error scales as $\mathcal{O}(\Delta t^3)$ for our mid-point Crank-Nicolson scheme) and computational cost, and is sufficient to capture the dynamics of the system without introducing significant numerical errors. In physical terms, 0.1 a.u. corresponds to only about 2.4 attoseconds, so even this coarse time-step is extremely fine relative to experimental timescales. Thus, the choice for the time-step is purely to ensure convergence with the numerical integrator. For the simple Landau-Zener model benchmark simulations, a smaller time-step of $\Delta t = 0.01$ a.u. is used, ensuring that all integration schemes are well within their convergence regimes, and that time-step related errors remain negligible. This approach allows us to compare the performance of different numerical methods on a common footing, minimizing any bias introduced by the choice of time step.

### 3.5.2 Approximating the Time-evolution operator

In principle, the exact propagator for a quantum system is given by the time-ordered exponential of the Hamiltonian (2.21)

$$U(t, t_0) = \mathcal{T} \exp\left( \frac{-i}{\hbar} \int_{t_0}^{t} H(t') dt' \right),$$

or by the simpler matrix exponential $U(t) = e^{-iHt}$ for a time-independent system Hamiltonian. In either case, computing this operator exactly is impossible to evaluate analytically once our basis grows beyond a few states. Instead we must resort to numerical approximations, as discussed in section 2.3 that either approximate the operator $U$ itself, or step the wavefunction forward in time. Depending on the system size and whether or not the Hamiltonian is time-dependent, different numerical techniques are more appropriate.

For our simulations in the double-well Morse potential, we rely exclusively on two unitary-preserving, stable schemes:

- **Matrix exponentiation via Padé:** This is the most straightforward approach, where we compute a direct evaluation of the matrix exponential $U = \exp\left( -\frac{i}{\hbar} H \Delta t \right)$, typically using a Padé approximation combined with scaling and squaring, as implemented in `scipy.linalg.expm`. This method is efficient and works well for small to medium-sized matrices. Cost scales as $\mathcal{O}(N^3)$, where $N$ is the number of basis states [67].

- **Crank-Nicolson method:** An implicit midpoint method that approximates the evolution operator as a weighted average of states at the current and next time step,

$$\psi(t + \Delta t) = \left( \mathbb{I} + i \frac{\Delta t H}{2} \right)^{-1} \left( \mathbb{I} - i \frac{\Delta t H}{2} \right) \psi(t).$$

  This scheme also preserves unitarity and is numerically stable, making it useful for stiff or rapidly varying systems. It is much cheaper than matrix exponentiation, with the cost equivalent to solving a single linear system at each time step.

To make an informed choice, we also test two simpler integrators purely for benchmarking purposes, and to solidify our choice of methods. These will not be applied to the full system, but rather in a controlled testbed environment on the Landau-Zener model (2.32):

- **Taylor series expansion:** This method approximates the time-evolution operator as a Taylor series expansion in powers of the Hamiltonian. This is a very simple and straightforward method, but as we saw earlier, can be unstable or inaccurate unless the timestep is very small or the wavefunction norm is bounded.

- **Runge-Kutta methods:** These methods recast the TDSE as a first-order differential equation and integrate it stepwise. The 4th-order Runge-Kutta method (RK45) is common, though it does not preserve unitarity exactly.

By making this comparison, we shall see that the matrix exponentiation and Crank-Nicolson methods are the most reliable and efficient for our system, while the simpler methods are less accurate and more prone to numerical instabilities—even in the simple system.

#### Matrix exponentiation

Following the material presented in section 2.3, we know that our time-evolution operator (2.21) is given numerically, as an approximation, by the following expression (2.23)

$$U(t) \approx e^{-iH(t)\Delta t},$$

which is easily implemented direcly in python using the `scipy.linalg.expm` function. The approximation is only valid given a sufficiently fine[1] $\Delta t$, and/or slowly varying Hamiltonian. This function uses the `scipy.linalg` package to compute the matrix exponential using the algorithm introduced in [67], which in essence in a Padé approxmation to the exponential function, using a scaling and squaring method. The `scipy.linalg.expm` function is efficient and reliable, making it well-suited for systems of moderate size.

The function is implemented as follows:

```python
def time_evolution_operator(H, t, dt):
    return scipy.linalg.expm(-1j * H(t) * dt)
time = [...]
psi = [...]
psi_t = np.zeros([...])
dt = time[1] - time[0]
for t in time:
    U = time_evolution_operator(H, t, dt)
    psi_new = np.dot(U, psi)
    psi_t.append(psi_new)
    psi = psi_new
```

where `H` is the Hamiltonian matrix, `t` is time, and `dt` is the time step. This code snippet outlines how the `expm` function is used to compute the time-evolution operator, and how this operator is used in a time loop to evolve the wavefunction `psi`. The time-evolution operator is computed at each time step, and the wavefunction is updated accordingly. The `psi_t` variable is used to store the wavefunction at each time step, and can be used to visualize the dynamics of the wavefunction throughout the time-evolution procedure.

While matrix exponentiation provides a robust method for computing the time-evolution operator, its accuracy for time-dependent Hamiltonians depends on how the Hamiltonian is evaluated at each time step. In particular, since $U(t, t_0) \approx \exp(-iH(t)\Delta t)$, the choice of how to evaluate $H(t)$ on the interval $[t, t+\Delta t]$ can significantly affect the accuracy of the time-evolution operator. Some examples are

- **Euler (explicit first order):** $U(t+\Delta t, t) = \exp(-iH(t)\Delta t)$. This method is simple and fast, but inaccurate for rapidly varying Hamiltonians and/or large time steps.

- **Midpoint evaluation (second order):** $U(t + \Delta t, t) = \exp(-iH(t + \Delta t/2)\Delta t)$. This method is more accurate than the left-endpoint method, but still suffers from stability issues for large time steps.

- **Trapezoidal evaluation (second order, symmetric):** $U(t + \Delta t, t) = \exp(-i(H(t) + H(t+\Delta t))/2\Delta t)$. This method is more accurate than the midpoint method, and naturally leads into implicits methods like Crank-Nicolson.

The choice of evaluation method depends on the specific system, and in this work, we primarily use the Euler method for simplicity and speed. In the next section we will discuss the different approach of using numerical integration methods to solve the time-evolution operator, namely the Crank-Nicolson method and the Runge-Kutta method. These methods are more general and can be used for time-dependent Hamiltonians, but are also more complex and computationally expensive.

### 3.5.3 Numerical integrators

As we have seen, direct matrix exponentiation provides a robust and unitary method for approximating the time-evolution operator. However, it becomes increasingly inefficient and impractical for high-dimensional systems, due to the computational complexity of evaluating the

---

[1]Sufficiently is in general system specific, but it must atleast be $< 1$.

matrix exponential of the Hamiltonian in each time step. To address this, we resort to *numerical integration methods*, which offer more scalable alternatives for evolving the quantum system, and propagating the wavefunction through time.

These numerical methods treat the Schrödinger equation (2.9) as a first-order differential equation in time and aim to approximate the solution iteratively over successive time steps. This foregoes the need to explicitly compute the time-evolution operator (2.21), and instead focus on the evolution of the wavefunction itself.

Unlike direct matrix exponentiation—which preserves unitarity by construction—numerical integrators must be carefully designed to ensure that important physical properties, like norm conservation, are maintainted over time. Some integrators, like the Crank-Nicolson method, are specifically designed to preserve unitarity and are well-suited for long-time simulations. Others, like the Runge-Kutta method, may not preserve unitarity exactly, but is more flexible and can provide highly accurate results for a wide range of systems, and for shorter time simulations.

In this section, we present and suggest procedures to implement two widely used numerical integration schemes:

- **Crank-Nicolson method:** A semi-implicit, second-order finite-difference method that, while not computing the matrix exponential explicitly, it yields an approximative time-evolution operator as a weighted average of states at the current and next time step. It preserves unitarity by construction and is numerically stable, making it useful for rapidly varying systems. The unitary nature of the method ensures that the wavefunction remains normalized over time.

- **Runge-Kutta method (RK4):** A fourth-order explicit integration method that offers high accuracy and ease of implementation. It is particularly useful for systems with smooth dynamics, but does not preserve unitarity exactly. The RK4 method is computationally efficient, and instead focuses on evolving the wavefunction iteratively over time.

These methods are implemented in Python, and we will provide code snippets to illustrate their usage. They offer a powerful and flexible alternative framework for simulating the time evolution of quantum systems, especially when direct matrix exponentiation becomes impractical. The choice of method depends on the trade-off between computational cost, accuracy, and the specific requirements of the system being studied. In the following sections, we will present the implementation details and performance of these methods in the context of the simple Landau-Zener system (2.32) and, later on, employ these methods to study the full double-well Morse potential system.

### Crank-Nicolson method

Building on the limitations of the simple method of Euler-Cromer, and to improve upon the computational cost of direct matrix exponentiation, the *Crank-Nicolson method* offers a compelling, and physically grounded alternative. As mentioned, this is a semi-implicit, second-order finite-difference method that aims to solve the TDSE (2.9) iteratively over time. The weighted average of states used makes an approximative time-evolution operator—which in turn makes the method unitary by construction—and thus is key to preserve essential physical properties like **norm conservation** and **unitarity**.

At its core, the Crank-Nicolson method applies the trapezoidal rule to the Schrödinger equation, treating the Hamiltonian propagator as an average of its behaviour at the beginning and end of each time interval. This in turn leads to a scheme that does not explicitly compute the

time-evolution operator, but still approximates its action through a symmetric update rule. As stated, we apply the trapezoidal rule to the time-derivative in the TDSE (2.9):

$$\frac{|\Psi(t+\Delta t)\rangle - |\Psi(t)\rangle}{\Delta t} \approx \frac{-i}{2\hbar}\left[ H(t+\Delta t)\,|\Psi(t+\Delta t)\rangle - H(t)\,|\Psi(t)\rangle \right] |\Psi(t+\Delta t)\rangle$$

$$\approx |\Psi(t)\rangle - \frac{i\Delta t}{2\hbar}\left[ H(t+\Delta t)\,|\Psi(t+\Delta t)\rangle + H(t)\,|\Psi(t)\rangle \right].$$

Rearranging the terms of this equation, yields the Crank-Nicolson update rule:

$$\left[ \mathbb{I} + \frac{i\Delta t}{2\hbar}H(t+\Delta t) \right] |\Psi(t+\Delta t)\rangle = \left[ \mathbb{I} - \frac{i\Delta t}{2\hbar}H(t) \right] |\Psi(t)\rangle .$$

This equation represents a **linear system** of equations for the wavefunction, that must be solved at each time step. The implicit nature contributes to the stability of the method, and the symmetric structure of the update rule ensures that the resulting time-evolution operator is unitary to second order in time $\Delta t$. Expressed in matrix form, by left-multiplying the inverse of the left-hand matrix, the update rule, or rather, the approximative time-evolution operator $U_{CN}$, can be written as:

$$U_{CN}(\Delta t) = \left[ \mathbb{I} + \frac{i\Delta t}{2\hbar}H(t+\Delta t) \right]^{-1}\left[ \mathbb{I} - \frac{i\Delta t}{2\hbar}H(t) \right].$$

This expression is a **Padé approximation** to the exponential function, and it provides a second-order accurate approximation to the time-evolution operator that is norm-preserving. It is the (1,1) Padé rational to the exponential time-evolution operator [68, 69], and takes the following form in the time-independent case:

$$U = e^{-iH\Delta t/\hbar} \approx \frac{\mathbb{I} - \frac{i\Delta t}{2\hbar}H}{\mathbb{I} + \frac{i\Delta t}{2\hbar}H}.$$

For a time-dependant Hamiltonian, we use the average of the Hamiltonian at the current and next time step:

$$H = \frac{1}{2}(H(t+\Delta t) + H(t))$$

in place of $H$ to ensure unitarity, which is especially important for rapidly varying Hamiltonians, and is the procedure we shall use in our study. For a proof of unitarity, see appendix A.2.

Viewed as such, the Crank-Nicolson method situates itself somewhere in between numerical integration methods and approximate exponentiation schemes, providing a physical, flexible and efficient framework for quantum state time-evolution. Some of the key advantages of the Crank-Nicolson method include:

- **Unitarity:** The method preserves the norm of the wavefunction, ensuring that the total probability remains constant over time. This is crucial for maintaining physical consistency in quantum simulations.

- **Stability:** The implicit nature of the method provides numerical stability, making it particularly suitable for stiff or rapidly varying systems or long-time simulations.

- **Accuracy:** The second-order accuracy of the method supports the use of larger time steps compared to first-order methods, while still maintaining a high level of precision, as the local error scales as $\mathcal{O}(\Delta t^3)$, and global error as $\mathcal{O}(\Delta t^2)$.

- **Sparsity:** The method can be efficiently implemented for sparse Hamiltonians, as solving the linear system is generally more efficient than computing the full matrix exponential.

In the following, we shall outline a suggested implementation of the Crank-Nicolson method in Python, with a code snippet to illustrate its usage.

```python
N = ... # Number of time steps
hbar = 1.0  # Reduced Planck's constant (a.u)
psi = np.zeros([...])  # Initial wavefunction
time = np.linspace(0, 10, N)  # Time grid
dt = time[1] - time[0]  # Time step
def H_t(t):
    # Set the Hamiltonian matrix at time t
    # Placeholder function, replace with actual Hamiltonian
    return np.array([[1, 0], [0, 1]])  # Example: Identity matrix

def crank_nicolson(H_t, psi, t, dt):
    # Get the Hamiltonian matrix at the current time step
    H_current = H_t(t)
    H_next = H_t(t + dt)
    H_mid = (H_current + H_next) / 2  # Midpoint evaluation
    # Construct the Crank-Nicolson update operator
    U_CN = np.linalg.inv(np.eye(len(psi)) + 1j * dt / (2 * hbar) * H_mid) @ \
           (np.eye(len(psi)) - 1j * dt / (2 * hbar) * H_mid)
    # Solve the linear system to obtain the wavefunction at the next time step
    psi_new = np.dot(U_CN, psi)
    return psi_new
# Time evolution loop
psi_t = np.zeros((N, len(psi)), dtype=complex)
for t in time:
    psi_new = crank_nicolson(H_t, psi, t, dt)
    psi_t.append(psi_new)
    psi = psi_new  # Update the wavefunction
```

**Runge-Kutta method**

In contrast to the Crank-Nicolson method, the Runge-Kutta method trades unitarity and exact norm preservation for simplicity, flexibility and short-term accuracy. As such, it provides a versatile and widely used tool for initial value problems, and is particularly useful for systems with smooth dynamics. The RK4 method, in particular, is a fourth-order explicit integration scheme that offers high accuracy and ease of implementation.

Returning to the TDSE(2.9), we can recast it as a first-order differential equation (ODE) in time:

$$\frac{\partial}{\partial t} \left| \Psi(t) \right\rangle = -\frac{i}{\hbar} H(t) \left| \Psi(t) \right\rangle .$$

The Runge-Kutta methods are designed to solve ODEs of the form $dy/dt = f(t, y)$, where $y$ is the dependent variable (in our case, the wavefunction $\left| \Psi(t) \right\rangle$) and $f(t, y)$ is a function that describes the dynamics of the system (i.e the Hamiltonian). It does so by approximating the solution at successive time steps using a weighted average of the derivatives (slopes) evaluated at different intermediate points within the time step. The RK4 method, in particular, uses four evaluations of the derivative to achieve fourth-order accuracy, and provides a balanced trade-off between accuracy and computational efficiency and is a common choice in quantum dynamics

when unitarity is not strictly required. The RK4 update rule is given by:

$$k_1 = f(t, \Psi(t)) = -\frac{i}{\hbar} H(t) \, |\Psi(t)\rangle$$

$$k_2 = f(t + \frac{\Delta t}{2}, \Psi(t) + \frac{\Delta t}{2} k_1)$$

$$k_3 = f(t + \frac{\Delta t}{2}, \Psi(t) + \frac{\Delta t}{2} k_2)$$

$$k_4 = f(t + \Delta t, \Psi(t) + \Delta t k_3),$$

which yields the update to the wavefunction as

$$\Psi(t + \Delta t) = \Psi(t) + \frac{\Delta t}{6}(k_1 + 2k_2 + 2k_3 + k_4).$$

This method achieves a local error of $\mathcal{O}(\Delta t^5)$ and a global error of $\mathcal{O}(\Delta t^4)$, making it highly accurate for sufficiently small time steps $\Delta t$. However, as we have mentioned, the RK4 method does not in fact preserve unitarity and thus the wavefunction norm may drift, especially over longer time scales, unless norm corrections are applied repeatedly. Despite these limitations, for short time simulations, the RK4 remains a robust choice for time-evolution. Summarizing the key advantages of the RK4 method:

- **Simplicity:** The RK4 method is easy to implement and understand, making it a popular choice for many applications.

- **Flexibility:** The method can be applied to a wide range of systems, including those with time-dependent Hamiltonians.

- **Explicitness:** The RK4 method is explicit, meaning that it does not require the solution of a linear system at each time step, making it computationally efficient for a wide range of systems.

- **Accuracy:** The fourth-order accuracy enables the use of relatively large time steps while maintaining a high level of accuracy.

The following code snippet illustrates a suggested implementation of the RK4 method for time-evolution in Python, with illustration its usage in a time-loop:

```python
psi = np.zeros([...])  # Initial wavefunction
N = ... # Number of time steps
time = np.linspace(0, 10, N)  # Time grid
dt = time[1] - time[0]  # Time step
hbar = 1.0  # Reduced Planck's constant (in atomic units)
def H_t(t):
    # Define the Hamiltonian matrix at time t
    # This is a placeholder function
    return np.array([[1, 0], [0, 1]])  # Example: Identity matrix

def runge_kutta_4(H_t, psi, t, dt):
    # Define the Hamiltonian matrix at the current time step
    H_current = H_t(t)
    H_dt2 = H_t(t + dt / 2)
    H_dt = H_t(t + dt)

    # Compute the four slopes
    k1 = -1j / hbar * np.dot(H_current, psi)
    k2 = -1j / hbar * np.dot(H_dt2, psi + dt / 2 * k1)
    k3 = -1j / hbar * np.dot(H_dt2, psi + dt / 2 * k2)
```

```python
    k4 = -1j / hbar * np.dot(H_dt, psi + dt * k3)

    # Update the wavefunction using the RK4 update rule
    psi_new = psi + dt / 6 * (k1 + 2 * k2 + 2 * k3 + k4)
    return psi_new

# Time evolution loop
psi_t = np.zeros((N, len(psi)), dtype=complex)
for t in time:
    psi_new = runge_kutta_4(H_t, psi, t, dt)
    # Optionally, apply norm corrections to maintain unitarity
    correction = np.linalg.norm(psi_new)
    psi_new /= correction  # Normalize the wavefunction
    psi_t.append(psi_new)
    psi = psi_new  # Update the wavefunction
```

This code snippet outlines a suggested procedure, however—in our work, we shall instead use the `scipy.integrate` packages `RK45`[2] method, which is a built-in implementation of the RK4 method. This package provides a convenient and efficient way to perform numerical integration of ODEs, and is well-suited for our purposes.

In later sections, we compare the performance and qualitative behaviour of the Crank-Nicolson and RK4 methods when applied to the Landau-Zener system (2.32), providing insight into their respective advantages and limitations in a controlled testbed scenario.

### 3.5.4 Ramping protocols

In the context of time-evolution methods, ramping protocols refer to the controlled variation of system parameters over time, allowing for smooth transitions between different potential configurations. In our double-well Morse potential system, we will employ ramping protocols to gradually change the potential parameters during the simulation, to incur mixing of the states between the two wells.

In order to steer our system from the separable configuration $C_I$ into the degenerate, entangling configuration $C_{II}$ (and back again), we implement a time-dependent ramping protocol for the Morse potential parameters. This protocol is crucial to avoid diabatic transitions—undesired excitations caused by rapid parameter changes that drive the system away from its instantaneous eigenstates (which here define our $|0\rangle$ and $|1\rangle$ computational states) [38]—and to maintain precise quantum control over the induced entanglement.

We begin by choosing a total evolution time $T_{\text{total}}$ and a fixed time step $\Delta t$. We also define an interpolation function that linearly varies the potential parameters from their initial values in configuration $C_I$ to their final values in configuration $C_{II}$. The function of choice is a linear interpolation, which is simple and effective for our purposes. The parameters are defined as functions of time:

$$C(t) = (1 - \lambda(t))C_I + \lambda(t)C_{II}, \tag{3.3}$$

where $\lambda(t)$ is a time-dependent parameter that varies from 0 to 1 over the total evolution time $T_{\text{total}}$, by some ramping protocol we shall now outline.

To set the ramping protocol we partition the evolution into five segments:

- An **initial hold** of duration $T_{\text{start}}$, where the system is prepared in the separable configuration $C_I$ and can equilibrate.

---

[2]See `https://docs.scipy.org/doc/scipy/reference/generated/scipy.integrate.RK45.html`

- A **ramp-up** duration $T_{\text{up}}$, where the parameters interpolate from the initial configuration $C_I$ to the degenerate configuration $C_{II}$.

- A **hold** duration $T_{\text{hold}}$, where the system is held in the degenerate configuration $C_{II}$ to allow the system to explore the entangled regime.

- A **ramp-down** duration $T_{\text{down}}$, where the parameters interpolate back from the degenerate configuration $C_{II}$ to the separable configuration $C_I$.

- A final **hold** of duration $T_{\text{end}}$, where the system is held in the separable configuration $C_I$ to allow for equilibration and measurement.

To implement this ramping protocol, we define the time-dependent parameter $\lambda(t)$ as follows, using a cosine ramping function:

$$\lambda(t) = \begin{cases} 0, & t \leq t_{\text{start}}, \\[2mm] \dfrac{1 - \cos\left(\pi \frac{t - t_{\text{start}}}{t_{\text{up}}}\right)}{2}, & t_{\text{start}} < t \leq t_{\text{start}} + t_{\text{up}}, \\[2mm] 1, & t_{\text{start}} + t_{\text{up}} < t \leq t_{\text{start}} + t_{\text{up}} + t_{\text{hold}}, \\[2mm] \dfrac{1 + \cos\left(\pi \frac{t - (t_{\text{start}} + t_{\text{up}} + t_{\text{hold}})}{t_{\text{down}}}\right)}{2}, & t_{\text{start}} + t_{\text{up}} + t_{\text{hold}} < t \leq t_{\text{start}} + t_{\text{up}} + t_{\text{hold}} + t_{\text{down}}, \\[2mm] 0, & t > t_{\text{start}} + t_{\text{up}} + t_{\text{hold}} + t_{\text{down}}. \end{cases}$$

At each time step, we evaluate the potential parameters $C(t)$ using the interpolation function (3.3) and the ramping parameter $\lambda(t)$ and update the Hamiltonian accordingly in the main evolution loop. By varying the various ramping parameters, we can test and control how efficiently the system transitions, how well entanglement is induced, and how robust the protocol remains under various numerical methods. The ramping routine fits directly into our existing time-evolution framework, and provides a controlleed way to explore the dynamics of the double-well Morse potential system.

## 3.6 Post-processing

### 3.6.1 Measurement of gate fidelity

Our numerical two-qubit gate is represented by the $4 \times 4$ unitary matrix $U$ that we extract from the time-evolved system. Each column of $U$ is found by initializing the system in the four logical computational basis states $\{|00\rangle, |01\rangle, |10\rangle, |11\rangle\}$, and propagating through our time-evolutoin scheme that realises the SWAP-like operation by linearly ramping the system from configuration $C_I$ to $C_{II}$ and back, and projecting back onto the logical subspace to properly track evolution. $U$ is then constructed as

```
U = np.zeros((4, 4), dtype=complex)
psi_00 = ...
psi_01 = ...
psi_10 = ...
psi_11 = ...
psi_00t = evolve(psi_00, ramp_protocol)
psi_01t = evolve(psi_01, ramp_protocol)
psi_10t = evolve(psi_10, ramp_protocol)
psi_11t = evolve(psi_11, ramp_protocol)
psi0 = np.column_stack([psi_00, psi_01, psi_10, psi_11])
psit = np.column_stack([psi_00t, psi_01t, psi_10t, psi_11t])
U = psi0.conj().T @ psit
```
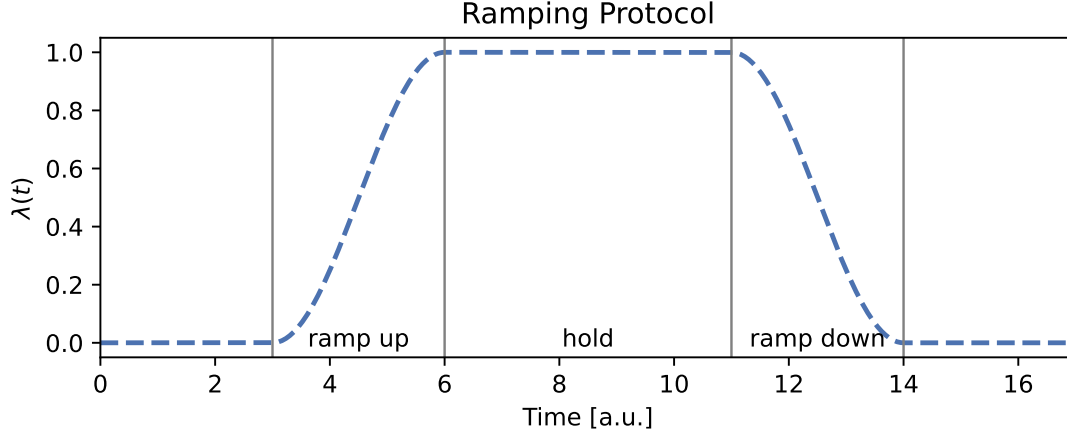
Figure 3.1: Example of a cosine ramping protocol as described in (3.5.4). The protocol smoothly transitions the system parameters from the initial configuration $C_I$ to the degenerate configuration $C_{II}$ and back again, allowing for controlled entanglement dynamics. The x-axis is time in atomic units (a.u), and the y-axis is the ramping parameter $\lambda(t)$, a dimensionless scalar value. In this illustration we have set $T_{\text{start}} = 3$ a.u, $T_{\text{up}} = 3$ a.u, $T_{\text{hold}} = 5$ a.u, $T_{\text{down}} = 3$ a.u, and $T_{\text{end}} = 3$ a.u. This ramping protocol is symmetric, and is not necessarily optimal for our system, but shows the general structure of such a protocol.

where $\psi_0$ is the initial state vector, and $\psi_t$ is the time-evolved state vector. $U_{target}$ is then the ideal unitary operation that we want to achive, i.e the ideal two-qubit gates. With these two unitary matrics in hand, we can compute the fidelity measures as shown in the following code snippet

```python
def classical_fidelity(U, U_target):
    d = U.shape[0]
    P = np.abs(U)**2
    P_targt = np.abs(U_target)**2
    F_j = np.sum(np.sqrt(P * P_targt), axis=0)
    F_classical = np.mean(F_j)

    return F_classical

def average_fidelity(U, U_target):
    d = U.shape[0]
    trace = np.trace(U_target.conj().T @ U)
    F = (np.abs(trace)**2 + d) / (d * (d + 1))

    return F
```

Before extracting the fidelity measures, we make certain that the time-evolution matrix $U$ is indeed unitary within numerical tolerance, i.e. $\|UU^\dagger - \mathbb{I} < 10^{-10}\|$, and we monitor leakage outside the logical subspace. Once these tests are passed we can compute the gate fidelity measures.

### 3.6.2 One-qubit phase correction

To recover the highest possible coherent gate fidelity, we can apply phase correction rotations to the unitary matrix $U$ after time evolution. To do so, we apply local $Z$-rotations (2.37) on each qubit to cancel any misaligned phases that may have accumulated during the time evolution. This phase-correction step sits at the very end of our pipeline, immediately after

we have extracted the unitary matrix $U$ from the time-evolved state. Its purpose is to remove all trivial single-qubit $Z$-phase rotations—leftover dynamical phases that have no impact on population transfer but degrade coherent fidelity, so that our final gate is as close to the ideal unitary operation as possible. The phases are moved onto the $|11\rangle$ state, and if we have suceeded in minimizing the $\zeta$-parameter (3.2), the result is an ideal unitary operation. Due to us moving unwanted phases, we may achieve high-fidelity gates even for non-zero $\zeta$.

In practice, we form the overlap matrix

$$M = U_0^\dagger U,$$

where $U_0$ is the ideal unitary operation that we want to achieve, and $U$ is the time-evolved unitary matrix. The overlap matrix $M$ should ideally be the identity matrix, but in practice it will have some non-trivial phases, both a harmless global phase and two relative phases—one phase for each qubits logical subspace. We extract these phases, and build the phase-correction matrix $P(\theta_2, \theta_3)$ (ignoring the global phase) as follows:

$$P(\theta_2, \theta_3) = \text{diag}\left( e^{-i(\theta_2+\theta_3)/2}, e^{-i(\theta_2-\theta_3)}, \dots \right)$$

which we can now apply to the time-evolved unitary matrix $U$ to correct for the misaligned phases, and recalculate the gate fidelity. This is the optimization, to find the optimal phase-correction angles $\{\theta_2, \theta_3\}$ that maximizes the average fidelity between the time-evolved unitary matrix $U$ and the target unitary matrix $U_0$. The structure of the phase-correction procedure is as follows:

---

**Algorithm 3** Phase Correction Procedure

---

1: **Input:** Time-evolved gate $U$, target gate $U_0$
2: Compute initial fidelity
$$F = \texttt{average\_fidelity}(U, U_0)$$

3: Compute overlap matrix
$$M = U_0^\dagger U$$

4: Extract phase-correction angles
$$(a_1, a_2, a_3) = \texttt{phase\_corr\_angles}(U)$$

5: Initialize $(\theta_1, \theta_2) \leftarrow (a_2, a_3)$
6: Define objective
$$f(\theta_1, \theta_2) = -\,\texttt{average\_fidelity}\big(P(\theta_1, \theta_2)\,U,\ U_0\big)$$

7: Optimize
$$(\theta_1^*, \theta_2^*) = \arg\min_{\theta_1, \theta_2} f(\theta_1, \theta_2)$$

   using SciPy's `minimize`
8: Construct phase-corrected gate
$$U' = P(\theta_1^*, \theta_2^*)\,U$$

9: Compute optimized fidelity

$$F_{\text{opt}} = \texttt{average\_fidelity}(U', U_0)$$

10: **return** $U'$, $F_{\text{opt}}$, and $(\theta_1^*, \theta_2^*)$

---

The follow code snippet implement exactly this procedure, again using the optimization algorithm `scipy.optimize.minimize` with the default 'BFGS' method. This optimization

finds the optimal phase correction angles $\{\theta_1, \theta_2\}$ that maximizes the average fidelity (2.38) between the time-evolved unitary matrix $U$ and the target unitary matrix $U_0$ (the ideal gate):

```python
def average_fidelity(U_0, U_target):
    d = U_0.shape[0]
    tr = np.trace(U_target.conj().T @ U_0)
    F = (np.abs(tr)**2 + d) / (d * (d + 1))

    return F.real

def phase_rotation(alphas, U):
    a2, a3 = alphas
    P = np.diag(
        [
            np.exp(-0.5j * (a2 + a3)),
            np.exp(-0.5j * (a2 - a3)),
            np.exp(0.5j * (a2 - a3)),
            np.exp(0.5j * (a2 + a3)),
        ]
    )

    return P @ U

def phase_corr_angles(overlaps):
    P = np.angle(overlaps)
    a1 = 0.5 * (P[1, 1] + P[2, 2])
    a2 = P[2, 2] - P[0, 0]
    a3 = P[1, 1] - P[0, 0]

    return -a1, -a2, -a3

def fidelity_opt_correction(alphas, U, fidelity):
    """Objective function"""
    return fidelity(phase_rotation(alphas, U))

def opt_fidelity(U_0, U):
    a1, a2, a3 = phase_corr_angles(U)
    opt_res = minimize(
        lambda x: -fidelity_opt_correction(x, U, partial(average_fidelity, U_0)),
        [(a2) % (2 * np.pi), (a3) % (2 * np.pi)],
    )

    G = phase_rotation(opt_res.x, U)
    G = np.exp(-1j * np.angle(G[0, 0])) * G

    return -opt_res.fun, opt_res.x, G
```

## 3.7 Implementation summary and workflow

Having now introduced the theoretical background and numerical strategies used to solve the time-dependent Schrödinger equation (TDSE) for our Morse double well quantum dot system, we conclude this chapter with a brief summary of how the various numerical components fit together in practice. This overview outlines the structure of our simulation codebase and the logic behind the implementation. The goal is to clarify how the different parts interact to evolve the quantum state over time and realise the quantum time evolution.

## Structure of the simulation framework

The simulation pipeline in this thesis follows a logical sequence, designed around the Morse double-well potential system for two interacting particles. The key stages of the implementation are as follows:

1. **Construct the Morse double-well potential**
   The first step is to implement a flexible and numerically stable representation of the Morse potential (2.19) with a double-well structure. This involves defining the functional form of the potential, setting physical parameters (well separation, depth, width), and discretizing the spatial domain to represent the wavefunctions and operators.

2. **Setup of the Hamiltonian matrix**
   In our Sinc-DVR basis, we compute all one-body (kinetic + potential) and two-body (Coulomb) integrals to set up our full two-particle Hamiltonian matrix (Section 3.2.3). We then construct the Hartree matrices for the two subsystems, which are used to diagonalize the system and project the full Hamiltonian onto a smaller subspace that accurately captures the essential dynamics of our system.

3. **System preparation**
   A separate optimization routine searches for two target configurations: $C_I$, in which the wells have well-separated, non-degenerate transition energies, and $C_{II}$, where the first excited states of the two subsystems are nearly degenerate. Once the optimal parameters are found, we rebuild the Hartree basis at $C_I$ and use this basis throughout the evolution for consistent overlap calculations.

4. **Time discretization and ramp protocol**
   We lay down a uniform time grid with step size $\Delta t$ over a total time $T$. On that grid we specify a ramping protocol that linearly interpolates the potential parameters from $C_I$ to $C_{II}$ and back at a chosen speed, staying entirely within the initial Hartree basis.

5. **Time-propagation**
   We then evolve the quantum state using one of two interchangable propagators: either direct matrix exponentition of the Hamiltonian, or the implicit Crank-Nicolson time integrator. Choice of method depends on the specific requirements of the simulation.

6. **Post-processing and analysis**
   After time evolution, we overlaps and state populations, von Neumann entropies, and other physical observables of interest. We also compute the unitary matrix $U$ that represents the time-evolved gate operation, and apply phase correction single-qubit rotations before computing gate fidelity measures to assess the performance of our quantum gate.

## Summary

The overall workflow — from system definition to result analysis — closely mirrors the physical logic of quantum simulation:

1. Build the system (basis + Hamiltonian),

2. Prepare the system (potential parameters),

3. Define the time domain and control fields,

4. Evolve the state using a suitable propagator,

5. Correct for any phase misalignments,

6. Extract and analyze physical quantities of interest.

This structure provides a coherent and extendable framework for studying both fundamental quantum dynamics and more complex qubit-like behavior in the coupled double-well Morse potential system.
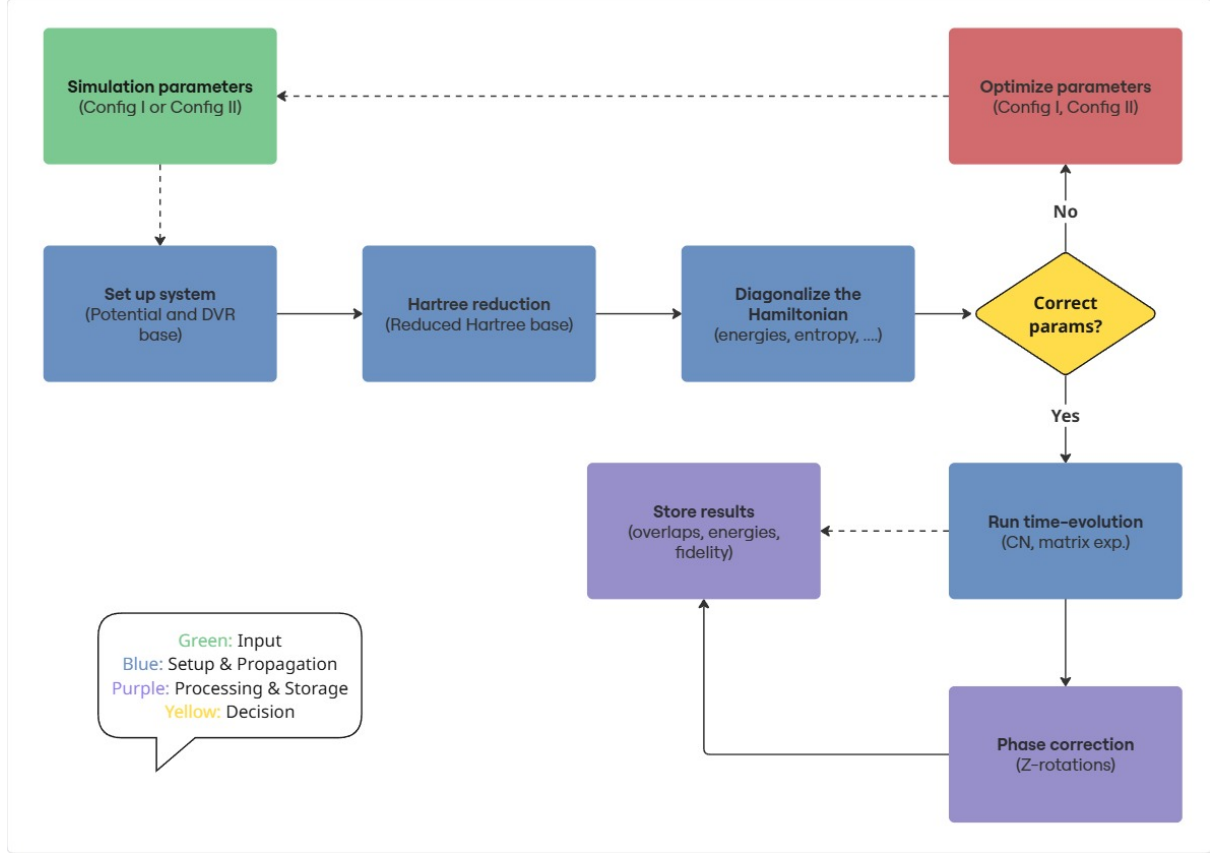


Figure 3.2: Graphical overview of the numerical workflow for simulating the two-particle Morse double-well potential system. The flowchart illustrates the main components of the simulation, from system setup and optimization, through time evolution and post-processing and gate fidelity calculations.

# Chapter 4

# Results

In this chapter, we present the results of our parameter optimization and dynamical simulations aimed at validating and operationalizing the Morse double-well system. Our primary objectives are twofold: first, to determine optimal parameters for two distinct configurations ($C_I$ and $C_{II}$) of the Morse double-well that exhibit the desired energy and entanglement properties; second, to explore the feasibility of adiabatically driving the system between these configurations to implement a SWAP-like two-qubit gate operation.

> *"If you want to make a simulation of Nature, you'd better make it quantum mechanical."*
>
> — Richard P. Feynman

We structure our findings into three main sections. First, we undertake a general preliminary study of the system to verify key foundational properties. We confirm the negligible impact of the exchange interaction between wells at moderate inter-well separations, justifying our treatment of the system as two separable subsystems. Furthermore, we validate our numerical framework—specifically the Sinc discrete variable representation (Sinc-DVR)—by direct comparison with the known analytical solutions of the Morse potential, and we benchmark our proposed numerical methods for time-evolution using a simplified Landau-Zener model (2.32).

Subsequently, we report on the results of our parameter optimization routines, presenting optimal paramters for the two configurations $C_I$ and $C_{II}$, that achieve desired entanglement properties and targeted eigenstate population, illustrated visually by population plots.

Finally, we detail our time-dependent simulations. Here, we first demonstrate dynamics within a simplified two-level model, showcasing the feasibility of adiabatically driving the system between configurations $C_I$ and $C_{II}$ to implement desired population transfer. Following this, we present a more comprehensive time-evolution simulation of the full (four-level) two-particle Morse double-well system. This includes rigorous assessment of gate fidelity, and results incorporating phase correction techniques to enhance gate performance.

## 4.1 Intermediate results of system and basis study

We here present the results of our study of the Morse double-well potential, and the validity of the Sinc-DVR basis for the system. First the analysis showcasing how the exchange term is negligible in th double-well system is presented, followed by a validation of the Sinc-DVR basis against the exact analytical eigenstates in a single-well system. Finally, we present a benchmark of the numerical methods used for time-evolution, using the Landau-Zener model as a testbed. This section serves as an intermediate step towards the final results presented in later sections.

### 4.1.1 Exchange interaction in the Morse double-well

In our Hartree product-state approach (Section 3.3), we include only the direct Coulomb interaction between the particles. This explicitly neglects exchange effects, justified by our intent to construct a system with strictly localized—and thus distinguishable—particles. Although exchange cannot create entanglement, it can influence energy spectra by shifting single-particle levels and modifying the composition of the reduced Hartree basis. To rigorously test our approximation, we benchmark our Hartree results against a fully antisymmetrized calculation performed using the configuration-interaction (CI) method described in detail in Section 3.4, following the procedure outlined in Section 3.2.1.

Recall that in the Hartree product-state approach, the two-particle Hamiltonian is given by

$$H_{dist} = H_L \otimes \mathbb{I} + \mathbb{I} \otimes H_R + V_{LR},$$

where $H_L$ and $H_R$ are the single-particle Hamiltonians of the left and right wells, respectively, and $V_{LR}$ is the direct Coulomb interaction between the particles—and the Hartree energies are found by direct diagonalization of this Hamiltonian. In the CI approach, we start from the same two-particle Hamiltonian but build a projection onto the anti-symmetric subspace spanned by all unordered pairs of single-particle states.

We carry out both calculations, Hartree and CI diagonalization as a function of inter-well separation $d$. In both solvers, we use a Sinc-DVR basis with $N = 800$ gridpoints and grid length of $L = 400$ a.u. This yields a grid spacing of $\Delta x = 0.5$ a.u. and a grid wide enough to encapsulate the system equally for all inter-well separations considered in the analysis. The grid spacing is chosen to be small enough to ensure convergence of the results. For CI we build the $N$ lowest single-particle orbitals and retain $\binom{N}{2}$ anti-symmetric states. We define the exchange-induced shift

$$\Delta E = E_{CI} - E_{Hartree},$$

where $E_{CI}$ is the ground-state energy obtained from the CI diagonalization and $E_{Hartree}$ is the ground-state energy obtained from the Hartree product state approach. The exchange shift $\Delta E$, as discussed in Section 3.2.1, quantifies the exchange interaction energy contribution, and is visualized alongside the two ground-state energies in figure 4.1. As the wells move farther apart, the exchange interaction energy falls off sharply, dropping below the numerical noise floor for separations $d > 10$ a.u, which is 10 $a_0$. Following the discussions in Appendix A.1, this corresponds to an effective inter-well separation of approximately 100 nm in a GaAs quantum dot system, well within the working ranges for quantum dots [9, 70].

We observe in figure 4.1 that the exchange interaction has a near-zero contribution beyond moderate separations, confirming that exchange contributions are truly negligible for our system—and that the Hartree product state captures the correct low-energy physics. This vindicates our assumption that the particles are distinguishable: once the two wells are sufficiently separated, the Pauli exclusion principle has vanishing impact of both energies and wavefunctions. The parameters used for this simulation are the optimal parameters for the
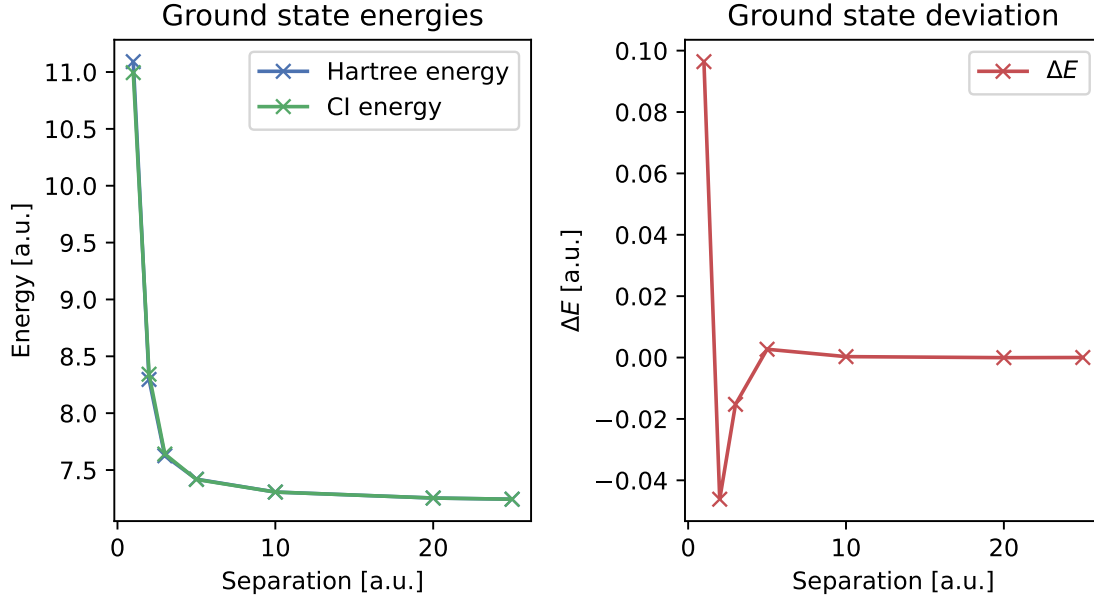
**Figure 4.1:** Ground-state energy as a function of the inter-well separation $d$ for the Morse double-well potential for Hartree (blue) and CI (green). The rapid decay of the exchange term of the coulomb interaction matrix with increasing well separation indicates that this term has a negligible effect on the ground state energy, confirming our assumption of locality and the usage of product states to express the wavefunction, as the particles become distinguishable for appropriate separation. We can see that the exchange term is close to zero for well separations larger than $d = 10$a.u., since $\Delta E = 0$. We also see the non-variational nature of the Hartree product state, as for some separations, the Hartree energy estimate falls below that of truncated CI, seen as a negative $\Delta E$.

Morse double-well configuration $C_I$ 4.2, as described in section 3.2.2 and presented in Section 4.2.

A final caveat: because the Hartree product state is not anti-symmetric, the Hartree energy is not variational with respect to exchange (it can lie slightly below the true anti-symmetric energy in a truncated basis, as seen in figure 4.1). One must therefore thread carefully when interpreting the energies obtained from the Hartree product state. In our tests, however, we find no (strictly) un-physical energies—the Hartree energy is within sub meV of the CI energy for all separations considered. We therefore conclude that for all practical purposes, the product state Hartree approximation suffices and this justifies neglecting exchange in our time-evolution simulations.

### 4.1.2 Sinc-DVR basis validation

**Energy eigenstates**

A natural validation of the Sinc-DVR basis is to check that the Sinc-DVR basis functions closely match the exact energy eigenstates of the system. We require that the eigenfunctions built from the Sinc-DVR basis to have a high degree of overlap with the exact energy eigenstates of the system. Otherwise, we risk losing important information about dynamics of the system, dynamics that may have a significant impact on the quantum control protocols we wish to implement.

We begin by computing the overlap matrix $S$ between the Sinc-DVR basis functions and the exact energy eigenstates of the Morse potential, from the analytical expressions in Section

2.1.5. Recall that the overlap matrix is defined as:

$$S_{ij} = \int \psi_i(x)\psi_j(x)dx,$$

where $\psi_i(x)$ and $\psi_j(x)$ are the Sinc-DVR basis and exact energy eigenstates, respectively using the procedures outline in Section 3.2.3.

The overlap matrix $S$ is then a measure of how well the Sinc-DVR basis functions represent the exact energy eigenstates of the system. The results are shown in figure 4.2, where we see that the overlap between the Sinc-DVR basis functions and the exact energy eigenstates is quite high, especially for the lowest lying states. We see that the overlap matrix is close to the identity matrix, indicating a near perfect overlap between the two basis sets.
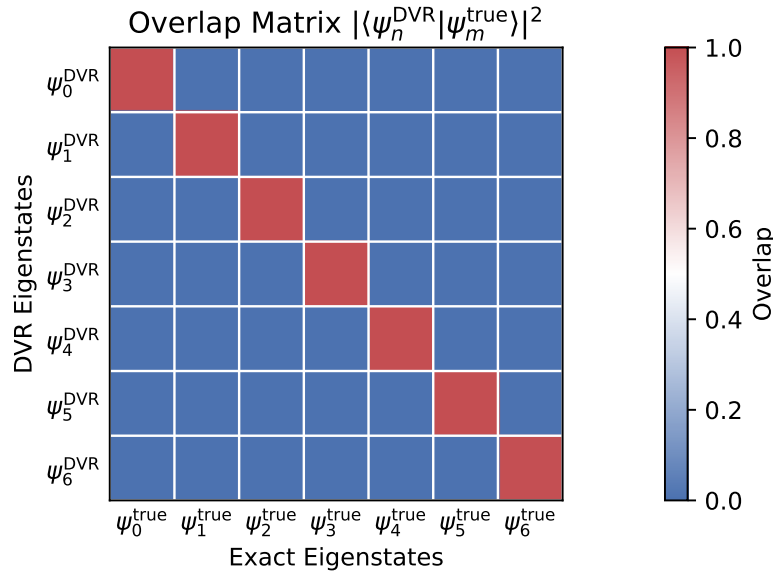


Figure 4.2: Overlap between the Sinc-DVR basis functions and the exact energy eigenstates of the Morse potential. The parameters used for the Morse potential are $D = 120.0$, $a = 1.0$, and $x_0 = 0.0$. The grid spacing is $\Delta x = 0.05$, and the number of grid points is $N = 600$ on a grid $x = [-1, 2]$.

Qualitatively, we see near perfect overlap between the Sinc-DVR basis functions and the exact energy eigenstates of the system. The diagonal elements of the overlap matrix exceed 0.9999 for the 6 lowest lying states, indicating a fidelity of 99.99% or higher, which is more than sufficient for our study. Due to the bound nature of the eigenstates in the Morse potential, we expect that the overlap should fall off rapidly when we are near the upper bounded state, and that is prevalent in the overlap matrix. Past eigenstate 7 (at 95.56% overlap), the 8th and 9th eigenstate have an overlap of 73.86% and 15.76% respectively, the remaining states have an overlap below 10%.

**Energy spectrum**

Next, we compute the energy spectrum of the Morse potential using the Sinc-DVR basis and compare it to the exact energy eigenvalues. We follow the procedure outlined in section 3.2.3, and the resulting energies are shown in figure 4.3. The energy spectrum is shown in atomic units, and we see that the energy levels of the Sinc-DVR basis closely align with the exact energies of the system, especially for the lowest lying states—of which we are mostly interested in.
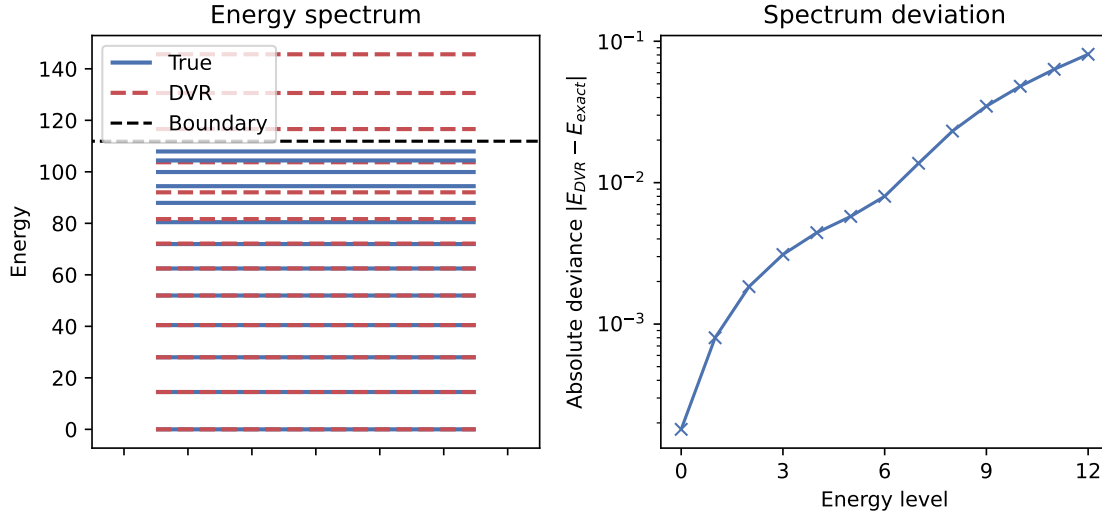
**Figure 4.3:** Comparison of the energy spectrum of the Morse potential using the Sinc-DVR basis and the exact energy eigenstates. The parameters used for the Morse potential are $D = 120.0$, $a = 1.0$, and $x_0 = 0.0$. The grid spacing is $\Delta x = 0.05$, and the number of grid points is $N = 600$ on a grid $x = [-1, 2]$. The energy spectrum of the lowest 13 eigenstates is shown in atomic units, blue line for the Sinc-DVR states and a red dashed line for the analytical eigenenergies. The absolute deviantion is plotted logarithmically. The energy level of the upper bounded state is shown as a black dashed line.

The DVR reproduces the ground-state energy exactly (within numerical tolerance), and the first four excited states to within $10^{-4}$ a.u. As seen in Figure 4.3, the absolute deviances of the energy eigenvalues are plotted logarithmically, and the first 8 eigenlevels have a relative error below $10^{-2}$. We see the clear limitation of the Sinc-DVR basis' ability to represent the higher order states, as their energies move above the bounded spectrum of the Morse potential trap. Furthermore, we see also how the energy deviation increases rapidly when moving towards the bounded states where the analytical solution 'squeezes' the energy levels together. The Sinc-DVR basis is not able to capture this 'squeezing' effect, and thus, the energy deviation increases as we move towards the boundary. As we are mostly interested in the lowest lying states, we do not mind the increasing error for the higher order states, or the lack of 'squeezing', as these levels are not directly relevant for our quantum control protocols, outside of the possibility to alter the dynamics of lower lying states should there occur population leakage to these higher-order states near the boundary.

**Implications and convergence**

Taken together, the near-perfect overlaps and sub-Hartree energy errors demonstrate that the Sinc-DVR basis introduce negligible residual errors in the representation of the energy eigenstates and the energy spectrum of interest in the Morse potential. If we desire, we may further reduce the error by increasing the number of grid points $N$ (or decreasing the grid spacing $\Delta x$). We therefore proceed with confidence that the Sinc-DVR basis is a suitable choice for our quantum control protocols, as it accurately captures the essential relevant features of the system. The grid spacing used here is much finer than what we aim for in the study of the double-well Morse potential. Most important for us is that the low-lying states in the system are well-represented as they are the targets for our quantum control protocols.

Setting up a test scenario with the following parameters $D = 60.0, a = 0.4$, we find that the Sinc-DVR basis with $N = 30$ grid-points on a grid $x = [-5, 10]$ with a grid spacing of $\Delta x = 0.5$ a.u. yields an overlap of $> 99.00\%$ for the first 4 eigenstates. This indicates that it is not only the grid spacing that matters, but also the distance from the boundary of the

grid. The Sinc-DVR basis accurately captures the low-lying states but fail to properly 'squeeze' the higher-order states when we approach the upper bound of the potential trap. For this reason, we will use a larger grid spacing of $\Delta x = 0.5$ a.u. in the study of the double-well Morse potential, while making certain that the states we are interested in are well below the uppe bound $l \leq \sqrt{2D}/a$, which is approximately $l \leq 27$ for the potential used in this test scenario. With this information at hand, it is imperative that we then construct our potential to be deep enough that the relevant states we wish to investigate lie far away from the boundary of the potential trap.

### 4.1.3 Numerical propagator benchmarks

To systematically validate our implementation of the aforementioned numerical methods (Section 3.5), we require a simple yet representative quantum system that exhibits non-trivial dynamics but still has closed form solutions for comparison. For this purpose, we will once again turn to the simple Landau-Zener model (2.32), introduced in Section 2.4.3. This simple two-level system is governed by a time-dependent Hamiltonian. It captures the essential features of quantum dynamics, making it an ideal testbed for our numerical methods in preparation for the more complex double-well Morse potential system we shall study. Recall, the Hamiltonian for the Landau-Zener model is given by:

$$H(t) = \begin{pmatrix} vt & V \\ V & -vt \end{pmatrix},$$

where $v$ is the sweeping velocity, $V$ is the coupling strength, and $t$ is the time. At $t = 0$, the uncoupled system would have a degeneracy, but the coupling $V$ opens a gap (lifts the degeneracy), resulting in an avoided crossing as we saw in section 2.4.3. Thus, this minimal system captures one of the simplest non-trivial dynamics of a quantum system, which also allows for closed form solution for the transition probability (2.33).

This makes an excellent textbed for our numerical integrators due to the following reasons:

- **Low dimensionality:** The Landau-Zener model is a two-level system, making it computationally efficient to simulate and analyze. This allows us to focus on the numerical methods without being overwhelmed by the computational complexity of the system.

- **Non-trivial dynamics:** The system exhibits interesting dynamics, such as transitions between states, which require the numerical implementations to accurately capture the time evolution of the wavefunction. This provides a meaningful test for the accuracy and stability of the numerical methods.

- **Analytical reference:** The Landau-Zener model has well-known analytical solutions for the transition probabilities and wavefunction dynamics, allowing us to directly compare the results of our numerical methods against these exact solutions. This serves as a benchmark for assessing the performance of the numerical methods.

#### Benchmark procedure

We initialize the system in the lowest lying state $|\Psi(0)\rangle = (1,0)^T$, which corresponds to the ground state of the uncoupled system, from an initial time $t_0 < 0$ to a final time $t_f > 0$. We will then compare:

- Global error vs. simulation time $T$: How the methods converge towards the closed form solution.

- Runtime efficiency: How fast each method can compute the transition probability.

- Stability during evolution: How well each method handles long time simulations.

We numerically propagate an initial wavefunction prepared in the ground state of the uncoupled system, and compute the final transition probability $P_{12}$, given analytically by (2.33). In other words, after the sweep we compute

$$P_{1 \to 2} = |\langle \Psi_2 | \Psi(t_f) \rangle|^2,$$

the probability of finding the system in the excited state $|\Psi_2\rangle$ at time $t_f$, given that it was initially prepared in the ground state $|\Psi_1\rangle$. The Landau-Zener transition probability is derived in the infinite time-limit, i.e $t \to \pm\infty$, so this analysis illustrate how each numerical method converges to the analytical solution as total simulation time increase.
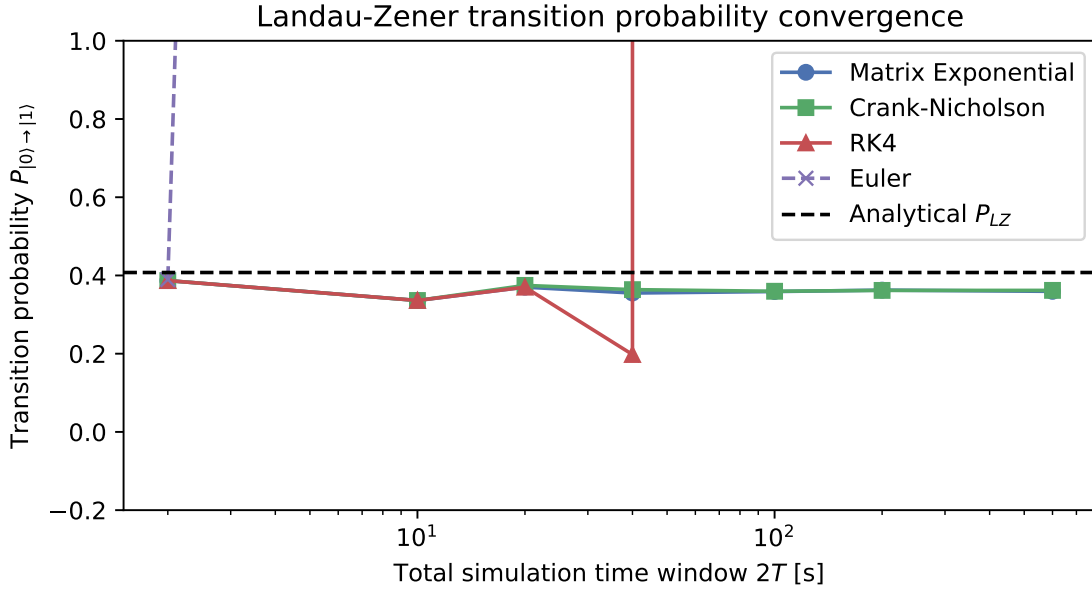


Figure 4.4: Final transition probability using $v = 7.0$, $V = 1.0$, computed with various numerical methods for increasing total simulation time $2T$. We see that Crank-Nicolson and matrix exponentiation converge towards the analytical Landau-Zener probability (dashed line), with RK4 showing good accuracy until instability sets in at longer times due to lack of normalization. The $x$-axis is in logarithmic scale.

As we can see in figure (4.4), some of the methods converge closely towards the analytical solution within certain timeframes, with varying degrees of stability. The Euler method diverges rapidly, as expected, due to its explicit nature and lack of normalization corrections. The more robust RK4 method remain stable and follow closely with the more sophisticated methods, before the accumulated error in the norm blows it up. Both of these methods can be improved upon by introducing norm corrections, at a computational cost (albeit minimal). The Crank-Nicolson method, on the other hand, remains stable and accurate for longer simulation times, as it preserves unitarity by construction. We also see that every method undershoots the analytical probability by a few percentages, and we expect this deviance to dissapear completely for even longer timespans. The reason for this is due to the asymptotic nature of the analytical expression, and how well the initial state accurately models the "true" ground state. At $t_0 = -T/2$, for a finite $T$, the off-diagonal terms are non-zero giving rise to *minor* mixing which will vanish as $T$ is increased. The culmination of both of these errors are seen as the deviance between "true" transition probability $P_{LZ}$ and the numerically computed probabilites.

To assess the computational speed of the numerical methods, a full Landau-Zener simulation was measured using the `time.perf_counter()` function in Python, which provides a high-resolution timer suitable for short time measurements.This measurement also includes system

overhead, yielding realistic performance metrics to evaluate each method. The benchmark was performed for the two-level system with sweeping parameter $v = 7.0$, coupling strength $V = 1.0$, and a time integration interval of $t \in [-5, 5]$ with 100,000 time steps, i.e a time-step of $\Delta t = 10^{-4}$s. The results are presented in the following table (4.1), along with remarks on their performance characteristics.

Table 4.1: Runtime comparison of time propagation methods for the Landau-Zener model ($v = 7.0$, $\Delta = 1.0$, $t \in [-5, 5]$, 100,000 steps). Timing measured using `time.perf_counter()`.

| Method | Time (ms) | Remarks |
|---|---|---|
| Matrix Exponential | 5942.1 | Most accurate, but very slow |
| Euler | 828.6 | Fastest, but unstable |
| RK4 | 2621.0 | Balanced performance |
| Crank–Nicholson | 1953.6 | Stable and efficient |

The table (4.1) shows that the matrix exponential method is the slowest, but also it is exact, while the Euler method is the fastest but unstable and inaccurate for longer simulations. The RK4 method is a good compromise between speed and accuracy, while the Crank-Nicolson method is stable and efficient, and—in our novel unoptimized implementation— outperforms the speed of RK4. This is generally not the case however, as for most system of moderate size, the linear system of equations in CN is more expensive to solve than the matrix products in RK4.

In conclusion, the convergence plot together with the runtime analysis shows that the Crank-Nicolson method is the most suitable for long time simulations, as it preserves unitarity and stability, for cases where direct matrix exponentiation is not feasible. We have confirmed that the explicit Taylor-expansion methods (Euler and RK4) can work over shorter intervals, but they require norm corrections, and small time steps to remain reliable for longer simulations. Direct matrix exponentiation is unbeatable with regards to accuracy, but scales exponentially in computational cost. Crank-Nicolson hits a sweet spot: It is unconditionally stable, preserves unitarity, and is computationally efficient for long time simulations.

Because our goal is to simulate two interacting particles trapped in a double-well potential, in a Hartree-reduced basis, we choose to employ direct matrix exponentiation whenever possible, and default to Crank-Nicolson for extended time-simulations. While one could explore more advanced methods, we firmly believe that the Crank-Nicolson method is sufficient for our purposes, as it provides a good balance between accuracy, efficiency and simplicity.

## 4.2 Optimization of the Morse Double-Well Parameters

Applying the optimization procedure outlined in Section 3.2.2, we identify two sets of optimal parameters for the Morse double well potential that meet the desired energy and entanglement criteria. Configuration $C_I$ is tailored to yield distinct, well-separated single-particle energy spectrums and vanishing two-body entanglement, while configuration $C_{II}$ is designed to produce a significant two-body entanglement and enforce a degeneracy of the first excited single-particle energy levels in each well to enable coherent mixing of the $|10\rangle$ and $|01\rangle$ logical states.

Table 4.2 summarizes the five optimized parameters—depths of the left and right wells $D_L$ and $D_R$, widths $k_L$ and $k_R$, and inter-well separation $d$—for each configuration, all in atomic units (a.u.). In $C_I$ a deeper left well ($D_L = 62.1709$ a.u.) alongside a shallower right well ($D_R = 60.7336$ a.u.) ensures distinct eigenenergies and a von Neumann entanglement entropy of $S_{VN} = 0.0000$ across the first 6 energy eigenstates, indicating a product state regime. Configuration $C_{II}$, on the other hand, slightly increases the right-well depth ($D_R = 64.1174$

Table 4.2: Optimized Morse potential parameters for configurations $C_I$ (separable) and $C_{II}$ (degenerate).

| Parameter | $C_I$ | $C_{II}$ |
|---|---|---|
| $D_L$ (depth of left well) [a.u.] | 62.1709 | 62.9733 |
| $D_R$ (depth of right well) [a.u.] | 60.7336 | 64.1174 |
| $k_L$ (width of left well) [a.u.] | 19.8947 | 13.2271 |
| $k_R$ (width of right well) [a.u.] | 21.8194 | 13.0978 |
| $d$ (inter-well separation) [a.u.] | 15.0000 | 14.9574 |

a.u.) and adjust a more balanced width for both wells ($k_L = 13.2271$ a.u., $k_R = 13.0978$ a.u.) so that the first excited single-particle energies coincide within numerical tolerance, and we have degeneracy in our two-particle system.

This engineered degeneracy creates a sharp 'entanglement peak' in the potential parameter space, allowing our ramp protocol to traverse from $C_I$ to $C_{II}$ to induce mixing of the logical states $|10\rangle$ and $|01\rangle$, and thus, generate a significant two-body entanglement. The two configurations are similar within a few atomic units, so quantum control protocols can perturb our system without having to significantly alter the system architecture, with minimal control overhead. Figure 4.5 illustrates the sharpness of the entanglement peak in the parameter space
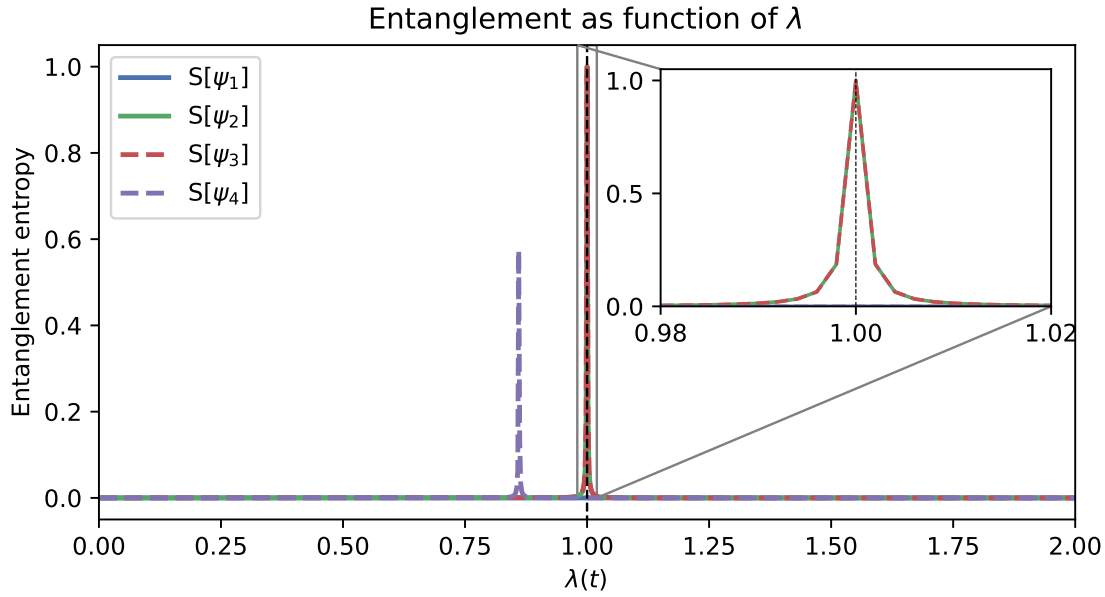


Figure 4.5: The entanglement peak in the parameter space of the Morse double-well potential. The plot shows the von Neumann entanglement entropy $S_{VN}$ in the first four eigenstates of the system, as a function of sweeping parameter $\lambda(t)$. The inset highlights the sharpness of the peak, indicating a narrow range of parameters where the first excited states are nearly degenerate, allowing for significant two-body entanglement generation. The peak is centered around $\lambda = 1$, corresponding to configuration $C_{II}$, where the first excited states are entangled. Parameters for configuration $C_I$ and $C_{II}$ are listed in Table 4.2
.

of our optimization procedure. It shows the von Neumann entanglement entropy $S_{VN}$ in the first four eigenstates of the system, as a function of sweeping parameter $\lambda(t)$ (3.5.4) as we traverse from configuration $C_I$ at $\lambda = 0$, to configuration $C_{II}$ at $\lambda = 1.0$ and beyond. The inset highlights the sharpness of the peak where we have 'good' parameters that allow for significant two-body entanglement generation. This illustrates the difficulty of optimizing the parameters for configuration $C_I I$, as the parameter space is barren and mostly flat (it looks more flat in

the figure due to the sweep being linear, as seen in (3.3)), and why a good initial guess was crucial for the optimization procedure to converge to the desired configuration. The sharpness stems mainly from the weak Coulomb-interaction our system experiences at our designated separation, and one would expect a wider peak if we moved the particles closer as this would allow more parameter configurations to mix as desired due to the increased coupling terms. This could however make it harder to find a suitable non-degenerate configuration without increasing distance drastically.
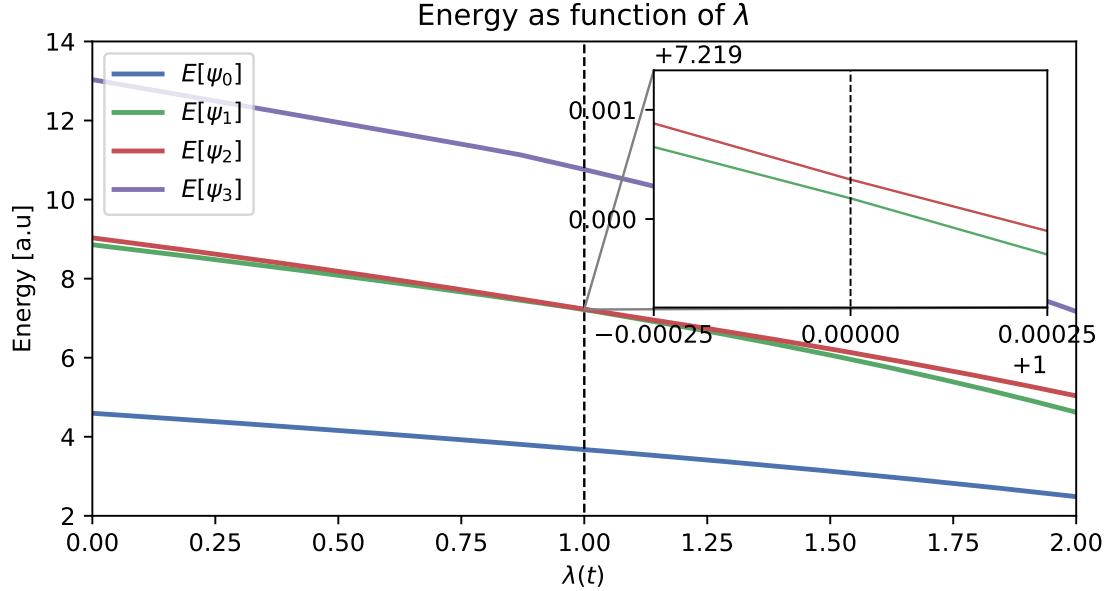


Figure 4.6: Energy curves for the four lowest lying energy eigenstates of the Morse potential as a function of ramping parameter $\lambda(t)$. The curves illustrate the avoided crossing between the first excited states in configuration $C_{II}$, where the first excited states $|10\rangle$ and $|01\rangle$ are nearly degenerate, and repel each other. The inset highlights the avoided crossing, where the non-interacting energies would cross and 'swap' places, but due to the Coulomb interaction the states repel each other, creating a 'gap' in the energy spectrum. Because our numerical procedure only enforces near-degeneracy, we omit overlaying the non-interacting energies to avoid confusion, as they are shifted in the spectrum due to the degeneracy not being exact.

In the inset of figure 4.6 we show the avoided crossing of the first excited energy levels as we move into the (near)-degenerate configuration $C_{II}$. The energy curves are plotted as a function of ramping paramter $\lambda(t)$, which varies from 0 to 1 as we ramp from configuration $C_I$ to $C_{II}$. The first excited states $|10\rangle$ and $|01\rangle$ are nearly degenerate, and repel each other due to the Coulomb interaction, creating a 'gap' in the energy spectrum where the non-interacting energies would cross and 'swap' places. This is akin to the avoided crossing we visualized in the Landau-Zener model in Section 2.4.3. We originally intended to overlay the corresponding non-interacting energies (that would cross in the absence of coupling), but in practice they do not cross exactly at $\lambda = 1.0$ (but rather at $\lambda \approx 0.98$) as our numerical procedure only enforces near-degeneracy up to finite tolerance. To avoid confusion by introducing a non-interacting energy that does not cross exactly at the same point, we omitted the non-interacting curves. We simply note that, in an ideal scenario, the uncoupled energies would indeed cross at $\lambda = 1.0$, and the avoided crossing would be exact when coupling is introduced. In our case however, the near-degeneracy is more than sufficient to induce the desired mixing of the logical states $|10\rangle$ and $|01\rangle$, and thus, generate significant two-body entanglement.

Figure 4.7 show the computational basis state (Hartree states) occupancy of the six lowest
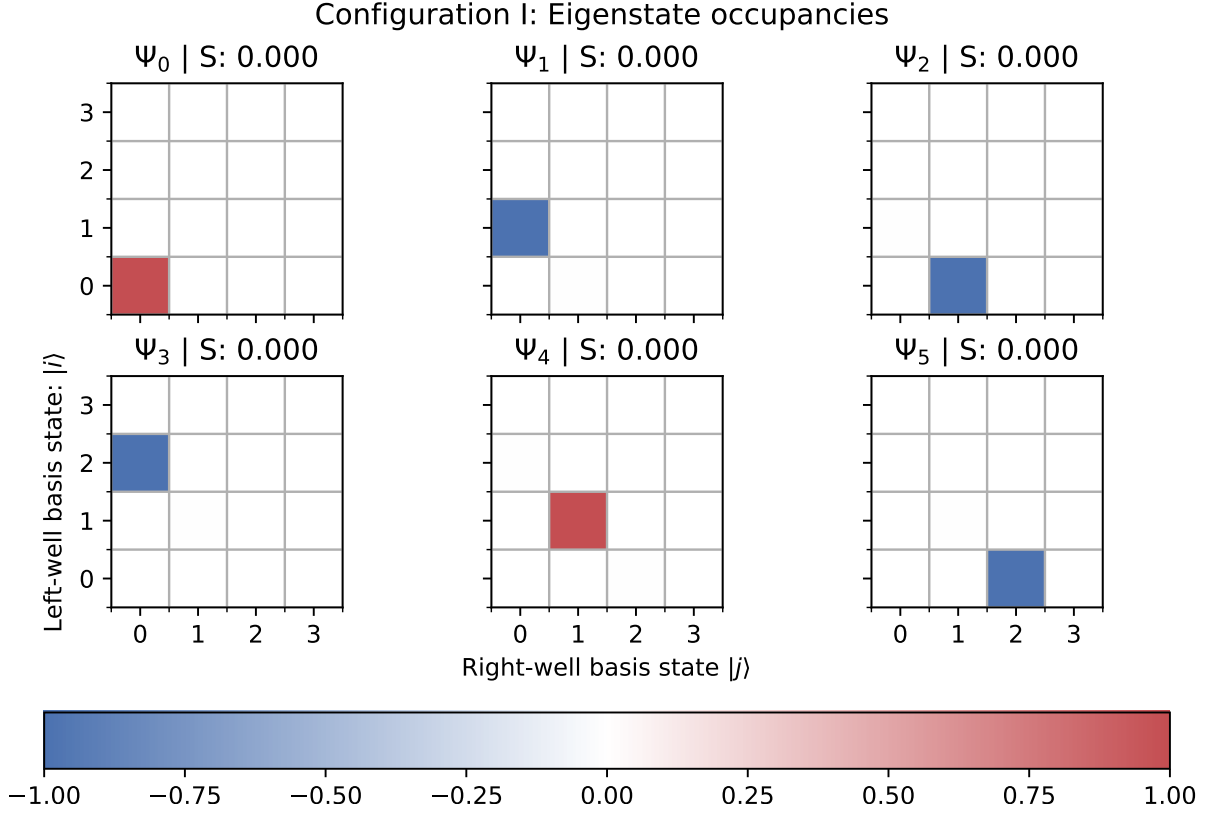
**Figure 4.7:** State populations of the six lowest two-particle energy eigenstates in configuration $C_I$. Each energy eigenstate is occupied by a single computational basis state (Hartree state), and are pure product states. The entropy $S$ for each state is zero, indicating no entanglement.

two-particle energy eigenstates for configuration $C_I$, where we observe that the states are indeed pure product states within a numerical tolerance of $10^{-7}$. Each eigenstate has exactly one dominant block, and is zero elsewhere—meaning the there is vanishing two-body entanglement between the particles, as seen from the listed entropy $S$ for each state—just what we aimed to achieve for the separable configuration.

By contrast, Figure 4.8 illustrates the same six two-particle energy eigenstates under configuration $C_{II}$, where we observe that the first excited states $|10\rangle$ and $|01\rangle$ are now mixed, with both states having significant contributions from both wells. The mixture is almost equal, and we are close to achieve the Bell states (maximally entangled states) for these two energy eigenstates, as indicated by the entropy $S \approx 1$. This means we have near perfect superpositions of the logical states $|10\rangle$ and $|01\rangle$. The remaining states remain essentially pure product states up to numerical tolerance $(10^{-7})$, highlighting that only the desired qubit subspace is affected by the entanglement, while the rest of the two-particle Hilbert space remains unaffected. This will be crucial for quantum control protocols we aim to run. The minor contributions from other basis states, seen as transparent red/blue tint in the heatmap, are negligible, and do not significantly affect the entanglement properties of the first excited states. As long as the coupling terms are small enogh and energy gaps wide in comparison, the mixing of higher order states will not lead to unwanted transitions or decoherence in our two-qubit gate operations.

Together, these two static heatmaps validate our optimization procedure: Configuration $C_I$ produces well-separated, pure energy eigenstates (pure in the sense they are singly occupied by a logical state), while configuration $C_{II}$ enforces a degeneracy of the first excited states, enabling a coherent mixing of the logical states $|10\rangle$ and $|01\rangle$, thus generating significant two-
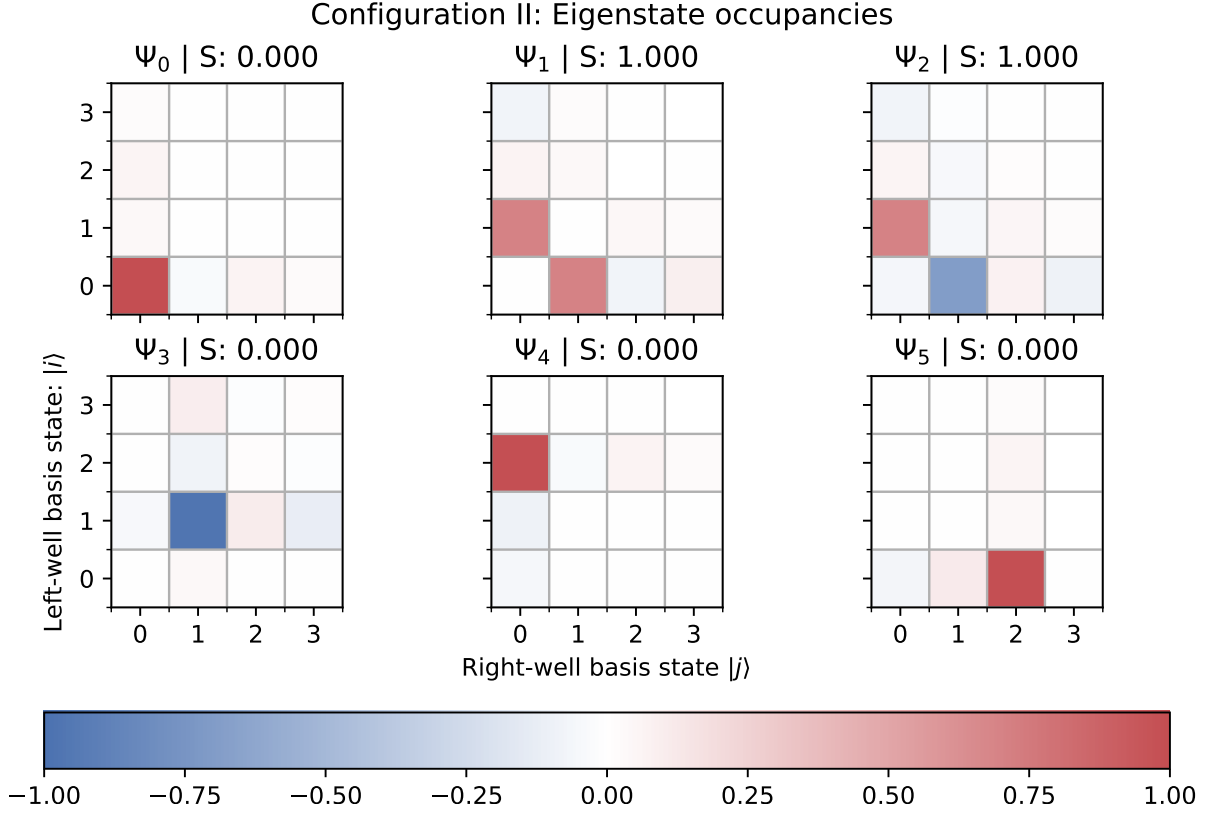
## Configuration II: Eigenstate occupancies



**Figure 4.8:** State populations of the six lowest two-particle energy eigenstates in configuration $C_{II}$. The first excited states $|10\rangle$ and $|01\rangle$ are now mixed, with significant contributions from the first excited state in each well. The entropy $S$ for these states is equal to 1 (within a tolerance of $10^{-}6$), indicating (near) maximal entanglement. We note that maximal entanglement is not equivalent to being in a Bell state, but rather, maximally entangled with *multiple* states beyond $|01\rangle$, $|10\rangle$. In this mixed configuration however, we see traces of other basis states leaking into our previously pure product states, especially prevalent in the higher energy states. This is seen as transparent red/blue tint in the heatmap, indicating minor contributions from other basis states.

body entanglement needed for our two-qubit gate operation protocols.

These two parameter configurations form the foundation for all subsequent static analyses and dynamical simulations in the thesis work when working in the $l = 4$ regime. The inter-well separation $d$ is set to $\approx 15.0$ a.u. for both configurations, which is sufficiently large to ensure negligible exchange interaction between the particles, as confirmed in Section 4.1.1. This also is within working ranges for quantum dots, and translated into effective mass units (for GaAs) the separation corresponds to approximately $d \approx 150$ nm, which is a reasonable distance for quantum dot systems [9], referring to the discussions in Appendix A.1 for the conversion from atomic units to effective mass units. In SI-units, we note that this separation is very small compared to the typical length scales of qubit architectures, $15a_0 \approx 0.79$ nm, one order of magnitude below the typical inter-dot separation in quantum dot systems, which is on the order of 10 nm [9].

## 4.3 Time-evolution of quantum gate protocols

We simulate the time-dependent Schrödinger equation for two distinguishable particles in our double-well Morse potential, in accordance with the procedural framework outlined in Section 3.7. The system is built in the Sinc-DVR basis using a grid length of 200 a.u. with 400 grid points, and mapped into the reduced Hartree basis as described in Section 3.3. We choose

eigenvectors of Hamiltonian in the optimal parameters for configuration $C_I$ as our measurement (computational) basis, as the eigenvectors of this configuration have complete overlap with the logical basis states $|ij\rangle$, i.e the product states of the two particles. Our ramping protocol (Section 3.5.4) smoothly ramps from configuration $C_I$ (non-degenerate qubit levels, zero entanglement) to configuration $C_{II}$ (close-to degeneracy in first excitations, high entanglement), and back. In what follows, we present the results of our time-evolution simulations, focusing on the state populations throughout.

First we shall present a minimal "two-level" model of the system ($l = 2$ basis functions per well) to demonstrate the idealized gate action and entanglement generation, and then we will present the full simulation ($l = 4$ basis functions per well) to investigate the effects of higher-order excitations, assess higher-order leakage and its impact on gate fidelity. The discussions that follow will focus on the implications of these results for quantum control protocols and the feasibility of implementing a two-qubit gate operation in a real-world experimental setup. Time-scales in the simulations are given in atomic units (a.u.), where 1 a.u. corresponds to approximately $2.42 \times 10^{-17}$ seconds (Hartree time), or about 58.7 attoseconds. The total simulation times will be converted as needed to SI units, and the time steps are set to $\Delta t = 0.1$ a.u. for all simulations, ensuring a sufficiently fine resolution for capturing the dynamics of the system.

### 4.3.1  Two-level model: Idealized gate action and entanglement generation

In the reduced four-dimensional Hilbert space spanned by the product states $\{|00\rangle, |01\rangle, |10\rangle, |11\rangle\}$, we simulate the time evolution using the unitary time-evolution operator (Section 3.5.2) for the two-particle system. Because only the first four states are active, there is no possibility for population leakage to higher order states outside the qubit subspace, and we can expect the system to behave as a perfect two-qubit gate. Figure 4.9 shows the time evolution of the state populations for the two-level model, where we have plotted the populations

$$P_{ij} = |\langle ij|\psi(t)\rangle|^2,$$

for each logical state $|ij\rangle$ in the qubit manifold, as a function of time.
Parameters used to simulate the $l = 2$ system are for the two configurations $(D_L, D_R, k_L, k_R, d)$:
$C_I = [39.9492, 40.0848, 9.4420, 8.4860, 10.3085]$ and $C_{II} = [40.0204, 41.9739, 6.9939, 7.0214, 9.9614]$. We ran a separate optimization scheme to identify these paramaters, in the same manner as for the full $l = 4$ system.

Figure 4.9 shows how the populations initially are clearly separated, with clean energy eigenfunctions (e.g $\langle\psi_0(0)|00\rangle = 1$), before the ramping procedure is initiated at $t = 50.0$ a.u. During the ramp we see a slight nudge in the populations, where the eigenstates become populated by higher order states, that are not included in the figure. After the ramp is completed, the first and second excited states $\psi_1(t)$ and $\psi_2(t)$, initially in $|01\rangle$ and $|10\rangle$ respectively, coherently mix. This is indication of a successful SWAP-like operation. The entanglement is generated as the populations of the two energy eigenstates mix, and swap, with a uniform frequency of oscillation $T_{\mathrm{rabi}}$ (2.34). This clean SWAP-like behaviour serves as a proof of concept for the two-qubit gate operation in our Morse double-well potential, demonstrating that the system can be controlled to perform a coherent SWAP of the logical states $|10\rangle$ and $|01\rangle$. At the end of the simulation the energy eigenfunctions are in a superposition,

$$|\psi_1(t_{\mathrm{end}})\rangle \approx 0.0027\,|01\rangle + 0.9973\,|10\rangle,$$
$$|\psi_2(t_{\mathrm{end}})\rangle \approx 0.9973\,|01\rangle + 0.0027\,|10\rangle,$$

with negligible contributions from the states $|00\rangle$ and $|11\rangle$, which remain (almost) constant throughout the simulation. We identify the importance of optimizing the ramping procedure to ensure that the populations of the states $|00\rangle$ and $|11\rangle$ remain consistent with our desired
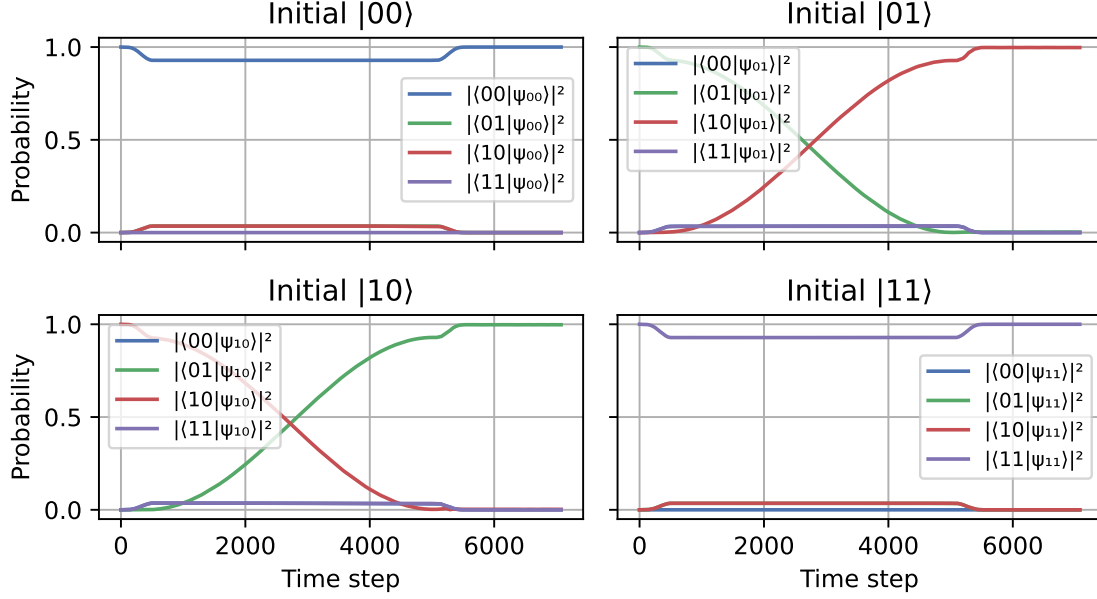
**Figure 4.9:** Evolution of the state populations for the two-level model of the Morse double-well potential using the Crank-Nicolson (CN) integrator, showing the idealized gate action and entanglement generation. The populations of the logical states $|10\rangle$ and $|01\rangle$ oscillate in a coherent manner, indicating a successful SWAP-like operation. The populations of the states $|00\rangle$ and $|11\rangle$ remain constant. The parameters used for the ramping protocol are $T_{\text{start}} = 10.0$ a.u., $T_{\text{end}} = 1500.0$ a.u, $T_{\text{up}} = 500.0$ a.u., $T_{\text{down}} = 500.0$ a.u., and the hold time $T_{\text{hold}} = 4566.0$ a.u. The ramping protocol is applied to the Morse double-well potential parameters for configuration $C_I$ and $C_{II}$, as described in Section 4.2. The simulation is run for a total time of $T_{\text{total}} \approx 7000.0$ a.u., with a time step of $\Delta t = 0.1$ a.u. Converted using the atomic units, this corresponds to a total time $T_{\text{total}} = 0.1639$ picoseconds.

gate operation post ramp, as the populations oscillates in time. Carefully constructed ramping protocols can be the difference between a successful (total) swap between the two states, a perfect mixing where the two states are equally populated, or a failed operation where the states go back to their original population after the gate operation has been performed. We used the Crank-Nicolson integration scheme to simulate the two-level model.

Qualitatively, we seem to have achieved a good SWAP gate in this simple system, and we check the gate fidelity to make a quantitative assessment of the gate operation. The logical propagator $U_{\text{logical}}$ is computed as described in Section 3.6, and we compare it to the ideal SWAP gate (2.35). The classical fidelity of our gate is $F_c = 99.94\%$, while we find the average fidelity to be $F = 46.40\%$. As expected, the classical fidelity which only concerns itself with population transfer is much higher than the average fidelity. We shall see in the larger model how we can improve upon the average fidelity by clever single-qubit rotations, as explained in Section 3.6.

### 4.3.2 Four-level model: Higher-order excitations and gate fidelity

In the four-level model, we include higher-order excitations by using $l = 4$ basis functions per well, allowing us to investigate the effects of higher-order excitations on the gate operation, and reveal realistic limitations of the two-qubit gate operation in our Morse double-well potential. Leakage between the qubit manifold $\{|01\rangle, |10\rangle\}$ and the higher-order spectator manifolds can lead to unwanted population transfer, instability during evolution, and de-phasing effects that can significantly reduce the fidelity of the gate operation. The propagator used in the simulations are the Crank-Nicolson method, and we use the optimal parameters for the two configurations

$C_I$ and $C_{II}$ as identified in Section 4.2. We build a grid of length 200 a.u. with 400 grid points, and map the Sinc-DVR basis into the reduced Hartree basis with 4 functions in each well.
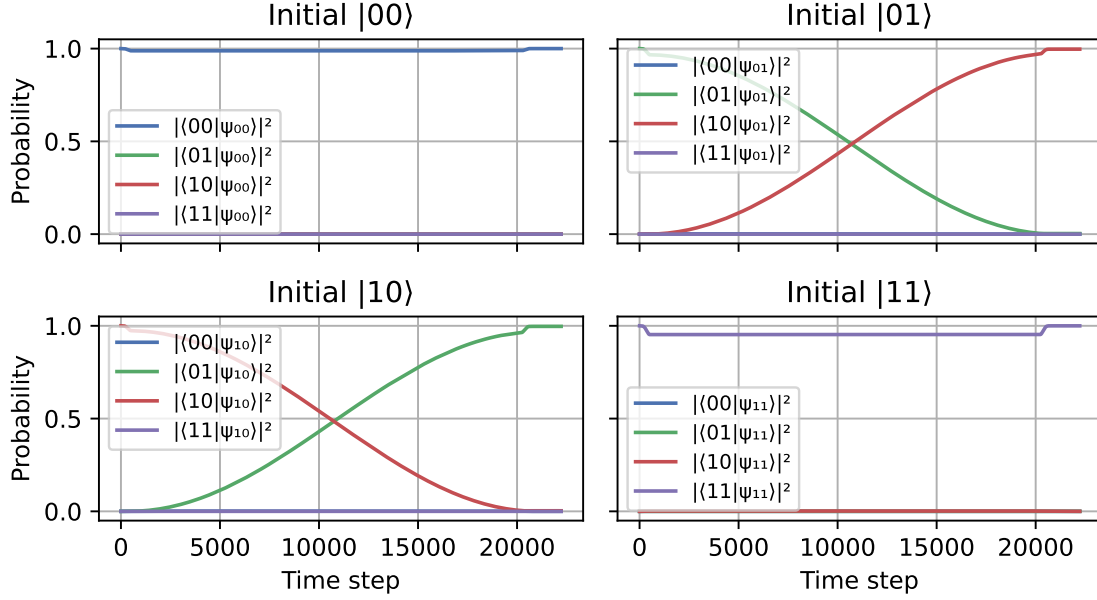
**SWAP-gate operation**



Figure 4.10: Evolution of the state populations for the four-level model of the Morse double-well potential using the CN integrator, showing the effects of higher-order excitations on the gate operation. The populations of the energy eigenstates $|\psi_0(t)\rangle$ and $|\psi_1(t)\rangle$ oscillate in a coherent manner, but due to the low coupling term $J = H[\psi_0, \psi_1]$ the oscillations are elongated. The coherent oscillations indicate successful SWAP-like operation. During evolution, there is possibly some mixture of higher order states not present in the plot, which we exclude for readability as they are non-existent at start and end of evolution. The parameters used in the ramping protocol are $T_{\text{start}} = 10.0$ a.u., $T_{\text{end}} = 1500.0$ a.u, $T_{\text{up}} = 500.0$ a.u., $T_{\text{down}} = 500.0$ a.u., and the hold time $T_{\text{hold}} = 19315.0$ a.u. The ramping protocol is applied to the Morse double-well potential parameters for configuration $C_I$ and $C_{II}$, as described in Section 4.2. The simulation is run for a total time of $T_{\text{total}} \approx 22000.0$ a.u., with a time step of $\Delta t = 0.1$ a.u. Converted using the atomic units, this corresponds to a total time $T_{\text{total}} = 0.53$ picoseconds.

In figure 4.10 we show the time evolution of the state populations for the four-level model, where we observe similar behaviour as in the idealised two-level mode. The populations of the eigenstates $|\psi_0(t)\rangle$ and $|\psi_1(t)\rangle$ oscillate in a coherent manner, indicating a successful SWAP-like operation. The final state population of the two energy eigenstates are

$$|\psi_1(t_{\text{end}})\rangle \approx 0.9970\,|01\rangle + 0.0030\,|10\rangle$$
$$|\psi_2(t_{\text{end}})\rangle \approx 0.0030\,|01\rangle + 0.9970\,|10\rangle,$$

and we see that we have a pure mixture of the logical states $|01\rangle$ and $|10\rangle$, and the SWAP was successful within an error of $10^{-2}$.

Figure 4.10 shows the protocol with hold time to approximately match the Rabi oscillation for a successful swap of the logical states. With a coupling term of $J = 7.9674 \times 10^{-5}$ a.u., we find the Rabi oscillation (2.34) period to be $T_R = 19715$ a.u., and we set the hold time accordingly. We note that the oscillations are elongated compared to the two-level model, indicating that the coupling term is lower than in the idealized case. This is expected, as we have higher-order excitations that can lead to leakage and de-phasing effects.

To assess how this evolution aligns with our desired SWAP gate operation, we can compute the logical propagator $U_{\text{logical}}$,

$$U_{\text{logical}} = \Psi_0^\dagger \Psi(t_f) = \begin{pmatrix} \langle 00|\psi_{00}(t_f)\rangle & \langle 00|\psi_{01}(t_f)\rangle & \langle 00|\psi_{10}(t_f)\rangle & \langle 00|\psi_{11}(t_f)\rangle \\ \langle 01|\psi_{00}(t_f)\rangle & \langle 01|\psi_{01}(t_f)\rangle & \langle 01|\psi_{10}(t_f)\rangle & \langle 01|\psi_{11}(t_f)\rangle \\ \langle 10|\psi_{00}(t_f)\rangle & \langle 10|\psi_{01}(t_f)\rangle & \langle 10|\psi_{10}(t_f)\rangle & \langle 10|\psi_{11}(t_f)\rangle \\ \langle 11|\psi_{00}(t_f)\rangle & \langle 11|\psi_{01}(t_f)\rangle & \langle 11|\psi_{10}(t_f)\rangle & \langle 11|\psi_{11}(t_f)\rangle \end{pmatrix},$$

where $\Psi(t_f)$ is the time-evolved wavefunction at the end of the simulation, and $\Psi_0$ is the initial wavefunction in the logical basis. The ideal SWAP gate operation would yield a propagator of the form (2.35), i.e

$$U_{\text{ideal}} = \begin{pmatrix} 1 & 0 & 0 & 0 \\ 0 & 0 & 1 & 0 \\ 0 & 1 & 0 & 0 \\ 0 & 0 & 0 & 1 \end{pmatrix}.$$

The result of our simulation yields the following logical propagator,

$$U_{\text{logical}} = \begin{pmatrix} 0.7157 - 0.6984i & 0.0000 + 0.0000i & 0.0000 + 0.0000i & 0.0000 + 0.0000i \\ 0.0000 + 0.0000i & 0.0191 - 0.0518i & -0.3709 - 0.9270i & 0.0000 + 0.0000i \\ 0.0000 + 0.0000i & -0.2850 + 0.9569i & -0.0238 - 0.0498i & 0.0000 + 0.0000i \\ 0.0000 + 0.0000i & 0.0000 + 0.0000i & 0.0000 + 0.0000i & 0.9769 + 0.2135i \end{pmatrix}$$

and the populations of the states are given by

$$|U_{\text{logical}}|^2 = \begin{pmatrix} 1.0000 & 0.0000 & 0.0000 & 0.0000 \\ 0.0000 & 0.0030 & 0.9970 & 0.0000 \\ 0.0000 & 0.9970 & 0.0030 & 0.0000 \\ 0.0000 & 0.0000 & 0.0000 & 0.9998 \end{pmatrix}.$$

We can see that the propagator is close to the ideal SWAP gate operation, with the populations of the states $|00\rangle$ and $|11\rangle$ remaining constant, while swapping the populations of the states $|\psi_1\rangle$ (initially $|01\rangle$) and $|\psi_2\rangle$ (initially $|10\rangle$) almost perfectly, to an accuracy of 99.70%. The small deviation can be improved upon by further optimizing the ramping protocol. We can assess the fidelity by computing the average and classical fidelity of the gate operation, equations (2.38) and (2.40), respectively. The average fidelity of our gate operation is computed to be $F = 26.41\%$, using $d = 4$. This indicates that while the gate operation (near) perfectly swaps the populations, it is still a no significant improvement over random operations, which would yield an average fidelity of $F = 1/d = 25\%$ [71]. The deviation from the ideal SWAP gate operation arises from the fact that we do not optimize with regards to the phase evolution of the states, and instead only focus on the population transfer between the states.

A better measurement of the gates performance before single-qubit corrections would be the classical fidelity, as this measures the population transfer. We find the classical fidelity to be $F_c = 99.92\%$, indicating that the gate operation is indeed successful in transferring the populations of the states $|01\rangle$ and $|10\rangle$, even without much optimization of the ramping protocol, and only an approximation of the Rabi oscillation is used. By that we mean, that while we target the Rabi oscillation period exactly (to 4 decimal places), we do not account for what happens *during* the parameter ramp (i.e the linear sweep between configurations), which will alter the perfect Rabi oscillation period. More studies would be needed to properly investigate the effects of the linear sweep and ramping duration on the 'perfect' Rabi oscillation period, and how this affects the gate fidelity.

## $\sqrt{\text{SWAP}}$-gate operation

In addition to the SWAP gate operation, we can also investigate the $\sqrt{\text{SWAP}}$ gate operation, which is a half-SWAP operation that transfers only half of the population from one state to another, inducing maximally entangled Bell-states (2.27) at the end of the operation. Figure
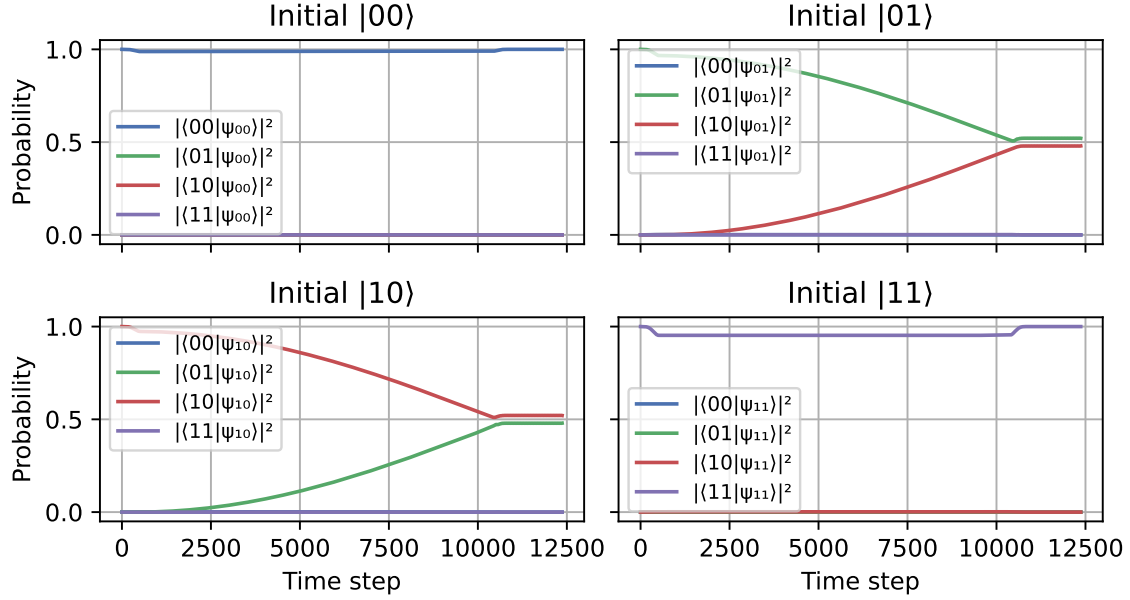


Figure 4.11: Evolution of the state populations in the four-level model of the Morse double-well potential using the CN integrator, showing the $\sqrt{\text{SWAP}}$ gate operation. The evolution is with a hold time $T_{\text{hold}} = T_{\text{SWAP}}/2 = 9857$ a.u. The ramp up and down times are set to $T_{\text{up}} = T_{\text{down}} = 500$ a.u., and we end with $T_{\text{end}} = 1500$ a.u. We see that running the evolution for a half-Swap duration results in a near-perfect mixed state, and we get Bell-like states for the first two energy eigenstates, while the remaining states remain constant. Qualitatively, this looks like we have implemented a successful $\sqrt{\text{SWAP}}$ gate-like operation, where the populations of the states $|01\rangle$ and $|10\rangle$ are mixed.

4.11 shows the time-evolution of the same system as in figure 4.10, but with a hold time of $T_{\text{hold}} = T_{\text{SWAP}}/2 = 9857$ a.u., which is half the Rabi oscillation period. To this end, we aim to achieve a $\sqrt{\text{SWAP}}$ gate operation, which would yield a maximally entangled Bell-state at the end of the operation. Qualitatively, we see that the population of the states $|01\rangle$ and $|10\rangle$ are highly mixed, indicating that we have been successful to some degree. At the end of the simulation, the populations of the two energy eigenstates are

$$|\psi_1(t_{\text{end}})\rangle \approx 0.4797\,|01\rangle + 0.5203\,|10\rangle,$$
$$|\psi_2(t_{\text{end}})\rangle \approx 0.5203\,|01\rangle + 0.4797\,|10\rangle,$$

which means we have achieved a good mixing of the two states, but not a perfect $\sqrt{\text{SWAP}}$ gate, although the states $\psi_0(t)$ and $\psi_3(t)$ remain constant (to an accuracy of $10^{-5}$). We can note that we have successfully implemented a $\sqrt{\text{SWAP}}$ gate-like operation, where the populations of the states $|01\rangle$ and $|10\rangle$ are mixed, but not to the extent that we achieve a perfect Bell-state. It is still a pure mixture (to numerical accuracy) of the two logical states $|01\rangle$ and $|10\rangle$, with no contribution from higher order states, but it is not the maximally entangled Bell-state. To quantitatively assess the success of the $\sqrt{\text{SWAP}}$ gate operation, we can compute the logical propagator $U_{\text{logical}}$ as before, and compare it to the ideal $\sqrt{\text{SWAP}}$ gate operation. Recall, the

ideal $\sqrt{\text{SWAP}}$ 2.36 is given by

$$U_{\sqrt{\text{SWAP}}} = \begin{pmatrix} 1 & 0 & 0 & 0 \\ 0 & \frac{1+i}{2} & \frac{1-i}{2} & 0 \\ 0 & \frac{1-i}{2} & \frac{1+i}{2} & 0 \\ 0 & 0 & 0 & 1 \end{pmatrix}.$$

The result of our simulation yields

$$U_{\text{logical}} = \begin{pmatrix} 0.9635 + 0.2677i & 0.0000 + 0.0000i & 0.0000 + 0.0000i & 0.0000 + 0.0000i \\ 0.0000 + 0.0000i & 0.1459 - 0.7066i & -0.4472 - 0.5286i & 0.0000 + 0.0000i \\ 0.0000 + 0.0000i & 0.0216 + 0.6921i & -0.5814 - 0.4273i & 0.0000 + 0.0000i \\ 0.0000 + 0.0000i & 0.0000 + 0.0000i & 0.0000 + 0.0000i & -0.8709 + 0.4914i \end{pmatrix}.$$
$$(4.1)$$

Of which, if we take the element-wise modulus, we gain the population transfer matrix

$$\sqrt{|U_{\text{logical}}|^2} = \begin{pmatrix} 1.0000 & 0.0000 & 0.0000 & 0.0000 \\ 0.0000 & 0.7215 & 0.6924 & 0.0000 \\ 0.0000 & 0.6924 & 0.7215 & 0.0000 \\ 0.0000 & 0.0000 & 0.0000 & 1.0000 \end{pmatrix}. \tag{4.2}$$

As we are primarily interested in the realisation of correct population transfer, we can assess the fidelity of the population transfer, yielding a classical fidelity of $F_c = 99.99\%$, now calculated using (2.39) due to the non-deterministic nature of the $\sqrt{\text{SWAP}}$-gate. The single-qubit rotations improved the average fidelity from $F = 25.26\%$ to $F = 77.30\%$, which is a significant improvement, but still not anywhere near the ideal $\sqrt{\text{SWAP}}$ gate operation. We see that our gate works, and correctly transfers the populations—but without proper phase control during evolution, we struggle to correct the accumulated phases post-evolution.

### Phase correction for coherent gate fidelity

Applying the phase correction procedure (Section 3.6.2) to our raw time-evolved two-qubit unitary matrices $U_{\text{SWAP}}$ and $U_{\sqrt{\text{SWAP}}}$ dramatically improves their coherent gate fidelities. We summarize below the key numbers for both gate operations, before and after phase correction, to illustrate the impact of this procedure.

### SWAP gate

- **Raw gate fidelity:** $F_c = 99.92\%$ (classical fidelity), $F = 26.41\%$ (average fidelity)

- **Optimized phase angles:** $(\theta_2, \theta_3) = (3.8832, 1.4117)$ (radians)

- **Phase-corrected gate fidelity:** $F_c = 99.92\%$ (classical fidelity), $F = 98.79\%$ (average fidelity)

The optimized phase angles $(\theta_2, \theta_3)$ are applied to the time-evolved unitary matrix $U_{\text{SWAP}}$, resulting in a significant increase in both classical and average fidelities. The optimized gate operation after phase correction is given by

$$G_{\text{SWAP}} = \begin{pmatrix} 1.0000 + 0.0000i & 0.0000 + 0.0000i & 0.0000 + 0.0000i & 0.0000 + 0.0000i \\ 0.0000 + 0.0000i & 0.0313 + 0.0455i & 0.9714 + 0.2309i & 0.0000 + 0.0000i \\ 0.0000 + 0.0000i & 0.9714 + 0.2309i & -0.0484 + 0.0265i & 0.0000 + 0.0000i \\ 0.0000 + 0.0000i & 0.0000 + 0.0000i & 0.0000 + 0.0000i & 1.0000 + 0.0000i \end{pmatrix}.$$
$$(4.3)$$

Qualitatively, this is a much better result than the raw gate operation, as the populations of the states $|01\rangle$ and $|10\rangle$ are now pure to a tolerance of $10^{-3}$, and the populations of the states $|00\rangle$ and $|11\rangle$ are now constant with no relative phase.

**√SWAP gate**

- **Raw gate fidelity:** $F_c = 99.99\%$ (classical fidelity), $F = 25.26\%$ (average fidelity)

- **Optimized phase angles:** $(\theta_2, \theta_3) = (2.8589, 1.0674)$ (radians)

- **Phase-corrected gate fidelity:** $F_c = 99.99\%$ (classical fidelity), $F = 77.30\%$ (average fidelity)

The optimized phase angles $(\theta_2, \theta_3)$ are applied to the time-evolved unitary matrix $U_{\sqrt{\text{SWAP}}}$, resulting in once again a significant increase in both classical and average fidelities. We are not as successful in improving the average fidelity as we were for the SWAP gate, likely due to the more complex phase factors present in the ideal gate operation. The optimized gate matrix is given by

$$G_{\sqrt{\text{SWAP}}} = \begin{pmatrix} 1.0000 + 0.0000i & 0.0000 + 0.0000i & 0.0000 + 0.0000i & 0.0000 + 0.0000i \\ 0.0000 + 0.0000i & 0.6072 - 0.3898i & 0.0652 - 0.6893i & 0.0000 + 0.0000i \\ 0.0000 + 0.0000i & -0.3823 - 0.5773i & 0.7192 + 0.0577i & 0.0000 + 0.0000i \\ 0.0000 + 0.0000i & 0.0000 + 0.0000i & 0.0000 + 0.0000i & 1.0000 + 0.0000i \end{pmatrix}$$

$$(4.4)$$

. Qualitatively, we see that the phase correction has improved the gate operation immensively, as the populations of the states $|01\rangle$ and $|10\rangle$ are now mixed cleanly to a much higher degree, and the population of states $|00\rangle$ and $|11\rangle$ are now constant with no relative phase. There is still room for improvement, and we again would need to optimize further the ramping protocol to ensure that the relative phases of are more easily optimized by our correction procedure.

These results demonstrate the effectiveness of the phase correction procedure in improving the coherent gate fidelities of our two-qubit gate operations. Initially, our average fidelities were no better than random operations ($\approx 25\%$), but after a single phase correction step, we achieved average fidelities of 98.79% for the SWAP gate and 77.30% for the $\sqrt{\text{SWAP}}$ gate, with classical fidelities of 99.92% and 99.99%, respectively. This highlights the importance of phase control in quantum gate operations, and how it can significantly enhance two-qubit operations. In exprimental setups, such single-qubit phase corrections are usually seamlessly integrated into the two-qubit gate protocols—in fact, the implementation of single-qubit rotations is so straightforward that fidelities routinely exceed 99.99% with negligible execution time [72]. As a result, relative phase errors from these rotations are not major contributors to two-qubit gate fidelities. With this in mind, we have here assumed that our single-qubit rotation gate is ideal—meaning that it rotates the states perfectly, which in practice is an excellent approximation given current hardware performance [38].

# Chapter 5

# Concluding remarks and outlook

In this thesis, we have explored the viability of a Morse-double well potential as a platform for quantum control of two-particle entanglement. We have viewed it as a candidate model for a prototype semi-conductor (or electronic device) quantum-dot qubit, aiming to demonstrate the feasibility of implementing one- and two-qubit quantum logic protocols. Our main goals were to (i) develop and validate a numerical framework for for obtaining the time-dependent Schrödinger equation (TDSE) solutions for the Morse double well in a product state approach, (ii) identify the optimal parameters for the potential to obtain optimized basis-set configurations for efficient representation, (iii) simulate coherent quantum-gate operations via time-evolution of the system, and (iv) assess the performance of the quantum control protocols in terms of gate fidelity, entanglement generation and population transfer.

**Summary of key findings**

- **Time-independent basis construction:** Our calculation demonstrated excellent agreement between the discrete-variable-representation (Sinc-DVR) basis and analytical expressions, with overlaps exceeding $99.99\%$ for the lowest six bound states (Figure 4.2), and energy deviations of less than $10^{-2}$ a.u. for the relevant energy levels (Figure 4.3).

- **Exchange interaction:** We showed that the exchange interaction has a negligible contribution to the ground-state energy for inter-well separations larger than $d = 10$ a.u. 4.1, confirming our assumption of strict locality and distinguishability of the particles. This justified the use of product states in our Hartree approach, which yielded a first excited-states energies within sub-meV of the exact configuration-interaction (CI) solution, and the remaining relevant energy levels with a deviance in the meV ranges of the exact solution ($10^{-4}$ a.u.).

- **Parameter optimization:** Running constrained optimization routines, we identified the optimal Morse double-well potential parameters for the two configurations $C_I$ and $C_{II}$. Configuration $C_I$ was optimized to yield distinct single-particle energies with wide energy gaps and zero entanglement, with the energy eigenstates showing complete overlap with the logical states $|ij\rangle$ as intended, indicated in Figure 4.7. Configuration $C_{II}$ was optimized to yield a degenerate first excited single-particle energy, allowing for coherent mixing of the logical states $|10\rangle$ and $|01\rangle$, with a high level of entanglement and a low energy gap between the first and second excited states. We aimed to achieve Bell-like entanglement in this configuration, and we see Bell-like mixing in the populations shown in Figure 4.8, with the populations of the logical states $|10\rangle$ and $|01\rangle$ being nearly equal, indicating a high degree of entanglement.

- **Time-dependent simulation:** With the optimal parameters in hand, we successfully simulated the time evolution of the system as we drove the system from configuration $C_I$

to $C_{II}$, and back again. We demonstrated coherent population transfer between the logical states $|10\rangle$ and $|01\rangle$. The time evolution was performed using the Crank-Nicolson method, indicating a successful implementation of the time-dependent Schrödinger equation in our numerical framework.

- **Gate fidelity:** With the unitary two-qubit gate operation implemented, we calculated the gate fidelity for the transfer between the logical states $|10\rangle$ and $|01\rangle$, achieving classical fidelities exceeding 99.92% for both gate operations after single-qubit phase correction was performed. For SWAP-gate showed an average fidelity of 98.79%, while the $\sqrt{\text{SWAP}}$ gate achieved an average fidelity of 77.30%. This verifies that while we achieved high fidelity population transfer, our lack of phase control during evolution resulted in a significant phase error, which is more prevalent in the $\sqrt{\text{SWAP}}$ gate due to complex phase factor in the gate.

## Implications for Qubit architectures

Our work positions the Morse double-well potential as an attractive model for quantum-dot qubits, demonstrating that it is possible to achieve coherent control of two-particle entanglement driven purely by Coulomb interaction via time-dependent Schrödinger evolution and perturbative control over the confining potential. By driving the gate operations purely by tuning the confining potential (well structure and separation), we achiveve high-fidelity gate operations without the need for additional external fields or complex control systems. This is a significant advantage, and can lead to simpler and more robust qubit architectures, reducing noise and decoherence that could arise from external control fields [13, 14, 55].

The ability to optimize the potential parameters for distinct configurations allows for flexible control over the system, enabling the implementation of quantum logic gates and entanglement generation protocols. The successful demonstration of coherent mixing of logical states in configuration $C_{II}$ indicates that the Morse double-well potential can serve as a viable platform for quantum information processing, with potential applications in quantum computing and quantum communication [38]. The Morse potentials mathematical form, originally derived to model the anharmonic bonds in diatomic molecules [22], naturally describes a smooth, tunable well profile that can be engineered in semiconductor heterostructures. Adjusting gate voltages one can closely mimic the desired potential (like in [21]), allowing for precise control over well depths, barrier heights, and inter-well separations. This tunability not only leverages decades of experience in molecular-potential shaping, but also aligns with existing semiconductor fabrication techniques that routinely create similar confinement profiles in quantum dots [9, 70].

Because the Morse double-well, and the entirety of the gate operation, can be implemented purely by electrostatic control, it offers a direct path from theory to experiment: One can directly translate the optimized parameters into gate voltages in a quantum dot system, without the need for complex microwave or laser control systems. Consequently, the work presented in this thesis provides a concrete foundation for future efforts to build and characterize Morse-based quantum-dot qubits, and to explore their potential for scalable quantum computing architectures.

In short, the deep connection between the Morse potential and real-world fabrication, combined with the promising fidelities and reconfigurability we have demonstrated, make this double-well potential a compelling model for future scalable, high-performance quantum-dot qubit architectures.

## Limitations of our study

- **Dimensionality and spin degrees of freedom:** Our 1D model neglects transverse confinement and spin-orbit coupling, both of which can significantly alter exchange

interaction and coherence properties in real devices [13, 14]. Furthermore, the 1D model does not capture the full complexity of a real 3D quantum dot system, and future work should consider extending the model to include more degrees of freedom.

- **Environmental and noise effects:** We did not incorporate environmental effects such as phonon interactions, charge-noise models, or other decoherence mechanism that are known to limit coherence in real quantum-dot systems [38, 70]. These effects can significantly impact the performance of quantum control protocols.

- **Phase control:** While achieving high fidelity population transfer, we did not implement a sophisticated phase control protocol during the time evolution. This resulted in significant phase errors, particularly in the $\sqrt{\text{SWAP}}$ gate operation, which we were unsuccessful in correcting with single-qubit phase corrections.

**Outlook and recommendations for future work**

Future work should focus on extending the Morse double-well model to include more realistic features such as transverse confinement, spin-orbit coupling, and environmental effects. Exploring noise models and their impact on our system would provide further insights into the robustness of the Morse double-well potential as a quantum-dot qubit architecture, and its possibility for quantum sensing [13, 73]. It should also extend the model to all three dimensions to capture the full complexity of a real quantum dot system. Additionally, it would be beneficial to explore the implementation of more advanced quantum control protocols, such as multi-qubit gates and error correction schemes beyond single-qubit rotations post-simulation, to further enhance the performance of the Morse double-well potential as a quantum-dot qubit architecture. Our work barely scraped the surface, and there are many avenues for further research into multi-qubit entanglement generation and quantum control protocols in Morse-like potentials.

Building on our 1D model, one should consider more refined methods for both representing the quantum state, and methods for time evolution. For example, our limited system truncated to a moderate number of basis states, and a further Hartree reduction to build product states. This could be improved upon by including a larger basis set and using more sophisticated methods for solving the quantum system without the need for such aggressive truncation. This could include using more advanced numerical methods such as the time-dependent density functional theory (TDDFT) that would allow for more complex interactions and higher order correlations between particles [74, 75]. A continued study in our simplified 1D model would want to explore more direct methods to control the phase evolution of the system, such as tracking relative phases of the logical states through the evolution, and using this to achieve higher fidelity gate operations. This could be done by implementing a more sophisticated ramping protocol that takes into account the relative phases of the logical states, and optimizes the ramping speed and duration to achieve the desired gate operation.

Finally, it would be interesting to explore the physical implementation of the Morse double-well potential in real quantum dot systems, and to investigate the feasibility of implementing the quantum control protocols demonstrated in this thesis in a real experimental setup. This would require a detailed study of the physical parameters of the Morse potential, and how they can be tuned in a real quantum dot system [9]. It would also require careful consideration in choice of materials and fabrication techniques to ensure that the Morse double-well potential can be realised in practice. Following the discussions in Appendix A.1, we believe that the Morse potential can be implemented in a semi-conductor quantum dot system, and that our simulation parameters are within realistic ranges for such systems.

**Concluding remarks**

In conclusion, we have demonstrated—with phase corrected SWAP fidelities exceeding 98%—that a Morse double-well potential offers a fully electrostatic platform for high-fidelity, two-particle entanglement protocols. By meeting our four key objectives (numerical framework validation, parameter optimization, coherent gate simulation, and fidelity assessment), this work lays a solid foundation for future research into experimentally accessible quantum-dot qubits based on the Morse double-well. Looking ahead, translating these theoretical insights into practical device architectures and incorporating spin degrees of freedom will be critical next steps toward realizing robust, scalable Morse-based quantum-computing systems.

# Appendix A

# Additional discussions and proofs

## A.1 Effective mass and SI conversion

In an effective-mass/dielectric medium we define the effective Bohr radius as

$$a_0^* = \frac{\epsilon_r}{m^*/m_e} a_0, \tag{A.1}$$

where $a_0 = 5.291772108 \times 10^{-11}$ m is the Bohr radius, $m^*$ is the effective mass of the electron in the medium, $m_e$ is the mass of a free electron, and $\epsilon_r$ is the relative permittivity of the medium. As the length scales in our simulations are in the region $\approx 15$ a.u. we choose to express the lengths in effective Bohr radii, $a_0^*$ (as we are free to do so, as long as we are consistent), to properly assess the physical relevance of our results. Similarly, we can convert both time and energy into effective mass units. The conversion factors are

$$E_h^* = \frac{m^*/m_e}{\epsilon_r^2} E_h,$$

$$t_0^* = \frac{\hbar}{E_h^*},$$

where $E_h \approx 27.21 eV$ is the Hartree energy.

In this appendix, we present the conversion of our result into the effective mass picture of GaAs-based quantum dots, which is the most common material used in quantum dot fabrication [9, 70]. The effective mass of the electron in GaAs is $m^* = 0.067 m_e$ and the relative permittivity is $\epsilon_r = 12.9$. This gives us an effective Bohr radius of

$$a_0^* = \frac{12.9}{0.067} a_0 \approx 1.0185 \times 10^{-8} = 10.19 \text{nm}, \tag{A.2}$$

and correspondingly the effective Hartree energy, and unit of time is

$$E_h^* = \frac{0.067}{12.9^2} E_h \approx 11 meV,$$

$$t_0^* = \frac{\hbar}{E_h^*} \approx 5.9 \times 10^{-14} \approx 60 \text{fs}.$$

We can now convert our results from a.u. by the conversion factors

$$\text{A length of 15a.u.} \to 15 a_0^* = 153 \text{nm},$$
$$\text{Gate duration 22000a.u.} \to 22000 t_0^* = 1.32 \text{ns},$$
$$\text{Ground state energy 7.5a.u.} \to 7.5 E_h^* = 82.5 \text{meV}.$$

This shows that our results are in the right ballpark for GaAs-based quantum dots, where typical quantum dot structures have lengths in the range of tens to hundreds of nanometers, gate durations in the sub-nanosecond to nanosecond range, and energy level spacings from a few meV to tens of meV [9, 70]. For our theoretical model, this means that we are well within reasonable physical paramters for certain quantum dot systems, and experimentally realizable gate operations. We note that we are on the larger side of the length scale, which is not a problem as we are interested in the qualitative behavior of the system, and not the exact numerical values.

## A.2 Midpoint Hamiltonian in CN

In what follows, we present a simple proof of the unitarity of the Crank-Nicolson (CN) update rule for the midpoint Hamiltonian, which is given by

$$H_{CN} = \frac{H(t) + H(t + \Delta t)}{2}.$$

Put into the update rule for the Crank-Nicolson propagator, we have

$$U_{CN} = \left[ \mathbb{I} - i\frac{\Delta t}{2} H_{CN} \right]^{-1} \left[ \mathbb{I} + i\frac{\Delta t}{2} H_{CN} \right].$$

To show that this propagator is unitary, we need to show that $U_{CN}^\dagger U_{CN} = \mathbb{I}$. Since the Hamiltonian is Hermitian, so is any sum of Hamiltonians, and thus $H_{CN}$ is Hermitian. Meaning

$$H_{CN}^\dagger = H_{CN}.$$

Defining new operators

$$A = \mathbb{I} - i\frac{\Delta t}{2} H_{CN},$$

$$B = \mathbb{I} + i\frac{\Delta t}{2} H_{CN},$$

we can rewrite the propagator as

$$U_{CN} = A^{-1} B.$$

Note that, since $H_{CN}$ commutes with itself, $[A, B] = 0$ since they are built from identity and $H_{CN}$.

Computing the adjoint (hermitian conjugate) of the new operators $A$ and $B$, we have

$$A^\dagger = \mathbb{I} + i\frac{\Delta t}{2} H_{CN} = B,$$

$$B^\dagger = \mathbb{I} - i\frac{\Delta t}{2} H_{CN} = A.$$

Which means that the adjoint of the propagator is

$$U_{CN}^\dagger = (A^{-1} B)^\dagger = B^\dagger (A^\dagger)^{-1} = A B^{-1}.$$

And we can check the unitarity condition

$$U_{CN}^\dagger U_{CN} = (A B^{-1})(A^{-1} B) = A(B^{-1} A^{-1})B = A(A^{-1} B^{-1})B = A\mathbb{I}B = AB = \mathbb{I},$$

where we used the fact that $A$ and $B$ commute, and that $AA^{-1} = \mathbb{I}$ and $BB^{-1} = \mathbb{I}$. Thus, we have shown that the Crank-Nicolson propagator with the midpoint Hamiltonian is unitary, i.e. $U_{CN}^\dagger U_{CN} = \mathbb{I}$.

# Bibliography

[1] Peter W. Shor. 'Polynomial-Time Algorithms for Prime Factorization and Discrete Logarithms on a Quantum Computer'. In: *SIAM Rev.* 41.2 (1999), pp. 303–332.

[2] Peter W. Shor. 'Fault-Tolerant Quantum Computation'. In: *Proc. 37th IEEE Conf. Found. Comput. Sci.* 1996, pp. 56–65.

[3] Nicolas Gisin et al. 'Quantum Cryptography'. In: *Rev. Mod. Phys.* 74.1 (2002), p. 145.

[4] Lov K. Grover. 'A Fast Quantum Mechanical Algorithm for Database Search'. In: *Proc. 28th ACM Symp. Theory Comput.* 1996, pp. 212–219.

[5] Andrew J. Daley et al. 'Practical Quantum Advantage in Quantum Simulation'. In: *Nature* 607.7920 (2022), pp. 667–676.

[6] Jonathan Wei Zhong Lau et al. 'NISQ Computing: Where Are We and Where Do We Go?' In: *AAPPS Bull.* 32.1 (2022), p. 27.

[7] Guido Burkard, Daniel Loss and David P. DiVincenzo. 'Coupled Quantum Dots as Quantum Gates'. In: *Phys. Rev. B* 59.3 (1999), p. 2070.

[8] Daniel Loss and David P. DiVincenzo. 'Quantum Computation with Quantum Dots'. In: *Phys. Rev. A* 57.1 (1998), p. 120.

[9] F. Pelayo García de Arquer et al. 'Semiconductor Quantum Dots: Technological Progress and Future Challenges'. In: *Science* 373.6555 (2021).

[10] Xin Zhang et al. 'Qubits Based on Semiconductor Quantum Dots'. In: *Chin. Phys. B* 27.2 (2018), p. 020305.

[11] Augustine D. Terna et al. 'The Future of Semiconductor Nanoparticles: Synthesis, Properties and Applications'. In: *Mater. Sci. Eng. B* 272 (2021), p. 115363.

[12] Peter Stano and Daniel Loss. 'Review of Performance Metrics of Spin Qubits in Gated Semiconducting Nanostructures'. In: *Nat. Rev. Phys.* 4.10 (2022), pp. 672–688.

[13] Andreas V. Kuhlmann et al. 'Charge Noise and Spin Noise in a Semiconductor Quantum Device'. In: *Nat. Phys.* 9.9 (2013), pp. 570–575.

[14] Jun Yoneda et al. 'A Quantum-Dot Spin Qubit with Coherence Limited by Charge Noise and Fidelity Higher than 99.9%'. In: *Nat. Nanotechnol.* 13.2 (2018), pp. 102–106.

[15] M. Veldhorst et al. 'An Addressable Quantum Dot Qubit with Fault-Tolerant Control-Fidelity'. In: *Nat. Nanotechnol.* 9.12 (2014), pp. 981–985.

[16] Bent Weber et al. 'Engineering Independent Electrostatic Control of Atomic-Scale ( 4 nm) Silicon Double Quantum Dots'. In: *Nano Lett.* 12.8 (2012), pp. 4001–4006.

[17] J. Gorman, D. G. Hasko and D. A. Williams. 'Charge-Qubit Operation of an Isolated Double Quantum Dot'. In: *Phys. Rev. Lett.* 95.9 (2005), p. 090502.

[18] Dohun Kim et al. 'Microwave-Driven Coherent Operation of a Semiconductor Quantum Dot Charge Qubit'. In: *Nat. Nanotechnol.* 10.3 (2015), pp. 243–247.

[19]  Xiao Xue et al. 'Quantum Logic with Spin Qubits Crossing the Surface Code Threshold'. In: *Nature* 601.7893 (2022), pp. 343–347.

[20]  Irina Heinz and Guido Burkard. 'Crosstalk Analysis for Single-Qubit and Two-Qubit Gates in Spin Qubit Arrays'. In: *Phys. Rev. B* 104.4 (2021), p. 045420.

[21]  Niyaz R. Beysengulov et al. 'Coulomb Interaction-Driven Entanglement of Electrons on Helium'. In: *PRX Quantum* 5.3 (2024), p. 030324.

[22]  Philip M. Morse. 'Diatomic Molecules According to the Wave Mechanics. II. Vibrational Levels'. In: *Phys. Rev.* 34.1 (1929), pp. 57–64. DOI: `10.1103/PhysRev.34.57`.

[23]  Lucjan Piela. *Ideas of Quantum Chemistry*. Elsevier, 2006.

[24]  Josh Apanavicius et al. *Morse Potential on a Quantum Computer for Molecules and Supersymmetric Quantum Mechanics*. 2021.

[25]  J. H. Smet et al. 'Gate-Voltage Control of Spin Interactions Between Electrons and Nuclei in a Semiconductor'. In: *Nature* 415.6869 (2002), pp. 281–286.

[26]  Attila Szabo and Neil S. Ostlund. *Modern Quantum Chemistry: Introduction to Advanced Electronic Structure Theory*. Courier Corporation, 1996.

[27]  P. A. M. Dirac. 'A new notation for quantum mechanics'. In: *Math. Proc. Cambridge Philos. Soc.* 35.3 (1939), pp. 416–418. DOI: `10.1017/S0305004100021162`.

[28]  Arjun Berera and Luigi Del Debbio. *Quantum Mechanics*. Cambridge University Press, 2021.

[29]  David J. Griffiths and Darrell F. Schroeter. *Introduction to Quantum Mechanics*. Cambridge University Press, 2018.

[30]  Trygve Helgaker, Poul Jorgensen and Jeppe Olsen. *Molecular Electronic-Structure Theory*. John Wiley & Sons, 2013.

[31]  Stefano Baroni et al. 'Phonons and Related Crystal Properties from Density-Functional Perturbation Theory'. In: *Rev. Mod. Phys.* 73.2 (2001), p. 515.

[32]  Charles Kittel and Paul McEuen. *Introduction to Solid State Physics*. John Wiley & Sons, 2018.

[33]  Gilbert Strang. *Linear Algebra and Its Applications*. 2000.

[34]  Jun John Sakurai, San Fu Tuan and Roger G. Newton. *Modern Quantum Mechanics*. American Institute of Physics, 1986.

[35]  J. C. Light, I. P. Hamilton and J. V. Lill. 'Generalized Discrete Variable Approximation in Quantum Mechanics'. In: *J. Chem. Phys.* 82.3 (1985), pp. 1400–1409.

[36]  Daniel T. Colbert and William H. Miller. 'A Novel Discrete Variable Representation for Quantum Mechanical Reactive Scattering via the S-Matrix Kohn Method'. In: *J. Chem. Phys.* 96.3 (1992), pp. 1982–1991.

[37]  John C. Light and Tucker Carrington Jr. 'Discrete-Variable Representations and Their Utilization'. In: *Adv. Chem. Phys.* 114 (2000), pp. 263–310.

[38]  Michael A. Nielsen and Isaac L. Chuang. *Quantum Computation and Quantum Information*. Cambridge University Press, 2010.

[39]  David Hochstuhl, Christopher M. Hinz and Michael Bonitz. 'Time-dependent multiconfiguration methods for the numerical simulation of photoionization processes of many-electron atoms'. In: *Eur. Phys. J. Spec. Top.* 223.2 (2014), pp. 177–336.

[40]  M. Born and R. Oppenheimer. 'Zur Quantentheorie der Molekeln'. In: *Ann. Phys.* 389.20 (1927), pp. 457–484. DOI: `10.1002/andp.19273892002`.

[41]    Fei Yuan et al. 'Addition and Removal Energies of Circular Quantum Dots'. In: *J. Chem. Phys.* 147.16 (2017). DOI: `10.1063/1.4995615`.

[42]    Peter W. Atkins and Ronald S. Friedman. *Molecular Quantum Mechanics.* Oxford University Press, 2011.

[43]    Michel H. Devoret and Robert J. Schoelkopf. 'Superconducting Circuits for Quantum Information: An Outlook'. In: *Science* 339.6124 (2013), pp. 1169–1174.

[44]    Yu Zhai, Hui Li and Robert J. Le Roy. 'Constructing High-Accuracy Intermolecular Potential Energy Surface with Multi-Dimension Morse/Long-Range Model'. In: *Mol. Phys.* 116.7–8 (2018), pp. 843–853.

[45]    R. Khordad and B. Mirhosseini. 'Linear and Nonlinear Optical Properties in Spherical Quantum Dots: Rosen–Morse Potential'. In: *Opt. Spectrosc.* 117 (2014), pp. 434–440.

[46]    D. B. Hayrapetyan et al. 'Exciton States and Interband Absorption of Cylindrical Quantum Dot with Morse Confining Potential'. In: *Superlattices Microstruct.* 78 (2015), pp. 40–49.

[47]    T. A. Sargsian et al. 'Effects of External Electric and Magnetic Fields on the Linear and Nonlinear Optical Properties of InAs Cylindrical Quantum Dot with Modified Pöschl–Teller and Morse Confinement Potentials'. In: *Phys. E* 126 (2021), p. 114440.

[48]    Lev Landau. 'Zur Theorie der Energieübertragung. II'. In: *Phys. Z. Sowjetunion* 2 (1932), p. 46.

[49]    Clarence Zener. 'Non-adiabatic Crossing of Energy Levels'. In: *Proc. R. Soc. Lond. A* 137.833 (1932), pp. 696–702.

[50]    Ahsan Nazir et al. 'Anticrossings in Förster Coupled Quantum Dots'. In: *Phys. Rev. B* 71.4 (2005), p. 045334.

[51]    A. Einstein, B. Podolsky and N. Rosen. 'Can Quantum-Mechanical Description of Physical Reality Be Considered Complete?' In: *Phys. Rev.* 47.10 (1935), pp. 777–780. DOI: `10.1103/PhysRev.47.777`.

[52]    E. Schrödinger. 'Die gegenwärtige Situation in der Quantenmechanik'. In: *Naturwissenschaften* 23.48 (1935), pp. 807–812. DOI: `10.1007/BF01491891`.

[53]    Dik Bouwmeester et al. 'Experimental Quantum Teleportation'. In: *Nature* 390.6660 (1997), pp. 575–579.

[54]    J von Neumann. 'Wahrscheinlichkeitstheoretischer Aufbau der Quantenmechanik'. In: *Nachr. Ges. Wiss. Göttingen, Math.-Phys. Kl.* 1927 (1927), pp. 245–272.

[55]    Jason R. Petta et al. 'Coherent Manipulation of Coupled Electron Spins in Semiconductor Quantum Dots'. In: *Science* 309.5744 (2005), pp. 2180–2184.

[56]    Garng M. Huang, Tzyh J. Tarn and John W. Clark. 'On the Controllability of Quantum-Mechanical Systems'. In: *J. Math. Phys.* 24.11 (1983), pp. 2608–2618.

[57]    Domenico d'Alessandro. *Introduction to Quantum Control and Dynamics.* Chapman & Hall/CRC, 2021.

[58]    John M. Nichol et al. 'High-Fidelity Entangling Gate for Double-Quantum-Dot Spin Qubits'. In: *npj Quantum Inf.* 3.1 (2017), p. 3.

[59]    Juan Yin et al. 'Entanglement-Based Secure Quantum Cryptography Over 1,120 Kilometres'. In: *Nature* 582.7813 (2020), pp. 501–505.

[60]    Lewis R. B. Picard et al. 'Entanglement and iSWAP Gate Between Molecular Qubits'. In: *Nature* 637.8047 (2025), pp. 821–826.

[61]   R. McDermott and M. G. Vavilov. 'Accurate Qubit Control with Single Flux Quantum Pulses'. In: *Phys. Rev. Appl.* 2.1 (2014), p. 014007.

[62]   Line Hjortshøj Pedersen, Niels Martin Møller and Klaus Mølmer. 'Fidelity of Quantum Operations'. In: *Phys. Lett. A* 367.1–2 (2007), pp. 47–51.

[63]   Anil Bhattacharyya. 'On a Measure of Divergence Between Two Statistical Populations Defined by Their Probability Distribution'. In: *Bull. Calcutta Math. Soc.* 35 (1943), pp. 99–110.

[64]   T. M. Ragonneau and Z. Zhang. *COBYQA Version 1.1.2*. 2024.

[65]   Jaseung Ku et al. 'Suppression of Unwanted ZZ Interactions in a Hybrid Two-Qubit System'. In: *Phys. Rev. Lett.* 125.20 (2020), p. 200504.

[66]   Pauli Virtanen et al. 'SciPy 1.0: Fundamental Algorithms for Scientific Computing in Python'. In: *Nat. Methods* 17 (2020), pp. 261–272. DOI: `10.1038/s41592-019-0686-2`.

[67]   Awad H. Al-Mohy and Nicholas J. Higham. 'A New Scaling and Squaring Algorithm for the Matrix Exponential'. In: *SIAM J. Matrix Anal. Appl.* 31.3 (2010), pp. 970–989. DOI: `10.1137/09074721X`.

[68]   Cleve Moler and Charles Van Loan. 'Nineteen Dubious Ways to Compute the Exponential of a Matrix, Twenty-Five Years Later'. In: *SIAM Rev.* 45.1 (2003), pp. 3–49.

[69]   Nicholas J. Higham. *Functions of Matrices: Theory and Computation.* SIAM, 2008.

[70]   Lucjan Jacak, Pawel Hawrylak and Arkadiusz Wojs. *Quantum Dots.* Springer Science & Business Media, 2013.

[71]   Karol Życzkowski and Hans-Jürgen Sommers. 'Average Fidelity Between Random Quantum States'. In: *Phys. Rev. A* 71.3 (2005), p. 032313.

[72]   Christopher J. Ballance et al. 'High-Fidelity Quantum Logic Gates Using Trapped-Ion Hyperfine Qubits'. In: *Phys. Rev. Lett.* 117.6 (2016), p. 060504.

[73]   Yi Zhang and Tza-Huei Wang. 'Quantum Dot Enabled Molecular Sensing and Diagnostics'. In: *Theranostics* 2.7 (2012), p. 631.

[74]   Richard Car and Mark Parrinello. 'Unified Approach for Molecular Dynamics and Density-Functional Theory'. In: *Phys. Rev. Lett.* 55.22 (1985), p. 2471.

[75]   Jürgen Hafner. 'Ab-Initio Simulations of Materials Using VASP: Density-Functional Theory and Beyond'. In: *J. Comput. Chem.* 29.13 (2008), pp. 2044–2078.